Modelling Radiation Damage in Spinel Oxides

BY

DNYANSINGH BACORISEN

A DOCTORAL THESIS

SUBMITTED IN PARTIAL FULFILMENT OF THE REQUIREMENTS

FOR THE AWARD OF

DOCTOR OF PHILOSOPHY OF LOUGHBOROUGH UNIVERSITY

November 2006

Abstract

In this thesis, defect formation by a radiation event in the normal $MgAl_2O_4$ was investigated using molecular dynamics (MD) simulations. The mechanisms and activation barriers for point defects to diffuse were determined using temperature accelerated dynamics (TAD). The role of cation inversion on defect formation and defect diffusion in spinel-structured oxides was analysed by performing the simulations in three spinels: the normal $MgAl_2O_4$, the half-inverse $MgGa_2O_4$ and the fully inverse $MgIn_2O_4$. The methodology employed in this thesis can be utilised for simulations in other ionic materials.

The onset of defect formation in $MgAl_2O_4$ was investigated by determining the threshold displacement energies, E_d, using MD simulations. E_d was dependent on the species of the primary knock-on atom and on its direction. The lowest energy required to create permanent displacements was 27.5 eV for an oxygen ion directed along [1 0 0]. In general, oxygen ions could be displaced at a lower energy than cations. The defects consisted mainly of split interstitials and cation antisites. Cation split interstitials were centred around a tetrahedral site with the two interstitials close to structural octahedral vacancies. The formation energy of an antisite pair was < 1 eV whereas this value was an order of magnitude higher for split interstitials.

Higher energy cascades in the 0.4-10 keV range, were performed in all three spinels using simulation cells containing up to 3 million charged particles. The large simulations were run using the parallel LBOMD code which has been implemented with the parallel DPMTA library for fast Coulomb evaluations. Subcascade branching at the higher energies and efficient interstitial-vacancy recombination in the normal $MgAl_2O_4$ resulted in similar defect structures as observed at the low energies. Ring defects and split vacancy defects on the Al sublattice were also a feature of the cascades. Defect formation in the half-inverse and fully inverse spinels was characterised by the formation of split interstitials, crowdions, crowdion chains and cation disorder

defects. The results show that cation interstitials in all three spinels preferentially occupied octahedral sites in the structure. The damage became more complex at the higher energies in the spinels with inversion; core regions containing a large amount of atomic rearrangement could be seen.

The long time evolution of point defects determined by TAD showed that diffusion in a normal spinel was easier as compared to a spinel with inversion. The anisotropy brought about by the inversion induced localised traps for the defects. The fastest diffusing species was the oxygen split interstitial in the normal $MgAl_2O_4$. Over the time scales accessible by TAD, no long range diffusion occurred in the half-inverse and inverse spinels.

In the final part of this thesis, the effect of low-energy displacive radiation in a MgO/Al_2O_3 system was modelled in order to investigate the formation and growth of a spinel structure at the interface. The interfacial rearrangement between the two materials showed that spinel-like tetrahedra formed under thermalisation followed by relaxation. However, no clear indication of spinel growth induced by the low 0.6 keV cascades was obtained.

Acknowledgements

I would like to thank my supervisor, Professor Roger Smith, for his guidance and support during the preparation of this thesis. I thank him for giving me the opportunity to present part of this work at two major international conferences in the USA.

I wish to thank Dr. Steven Kenny for his support at various points during my research. Invaluable discussions with Dr. Kenny are also acknowledged.

The technical support provided by Dr. Keith Watling is kindly acknowledged.

I wish to extend my gratitude to Dr. Preethee Nunkoo Gonpot for proposing my name as candidate for this position and for guiding me during the application process.

I wish to thank the whole team at Los Alamos and at Imperial College for their contribution in making this work possible. In addition, I wish to thank Blas Uberuaga, Kurt Sickafus, Srinivasan Srivilliputhur and family, and Art Voter (and his bike!), for making my one-week visit at Los Alamos National Laboratory an enriching experience. Fruitful collaboration with Robin Grimes, Jon Ball, Sam Murphy and Mark Levy from the Atomistic Simulation Group of Imperial College is kindly acknowledged.

I wish to thank my colleague and friend, Chris Gilbert, for providing me his *ab-initio* results.

My thanks also go to all my friends whom I met at Loughborough for making this experience memorable. Thanks to Ajeev, Hurry, San, Devianee, Dee and Binoy.

I would like to thank Loughborough University and Los Alamos for supporting my research.

I wish to thank my family, Mum, Dad, Ritesh and Hansha for their unconditional support. My deepest thoughts are for my fiancee, Tina, for her encouragement and tremendous support throughout my research. My thanks go to my uncles for their encouragement.

Contents

List of Figures

List of Tables

Chapter 1

Introduction

Many physical and chemical processes happening in nature can be modelled by some mathematical formulation based on a combination of existing laws and theorems. The accessibility to fast computers has made it possible for these models to be translated by an appropriate programming language into a computer software which can then be run efficiently as a computer simulation. Computer simulations act as a link between theory and experiment by providing a relatively easy way to solve and to understand complex problems. Modelling also helps to investigate the behaviour of a system under different conditions in order to make realistic predictions.

Computer simulation studies are widely used in materials science. Different techniques are available to analyse the properties of materials across a range of length and time scales, thus leading to the concept of multi-scale modelling. At the electronic level, quantum mechanical methods are employed to describe the interactions between electrons and nuclei. These models enable the energy of any arrangement of atoms in a system to be calculated relative to the atomic positions. This involves complex electronic structure calculations which are computationally intensive, thus limiting the system sizes investigated to be of the order of a few hundreds of atoms only. Simulations performed at the atomistic scale can involve thousands to millions of atoms using molecular dynamics (MD) or Monte Carlo (MC) methods [1]. MD uses

Newtonian mechanics to describe the time-evolution of mutually interacting atoms while MC is a stochastic method that can move a system from one configuration to another. At higher levels, a continuum representation of the material is modelled by neglecting the underlying atomic structure. The behaviour of materials under applied stresses or temperature gradients can be captured kinematically through displacement or velocity fields while the forces are described by a stress tensor field [2].

In this work, atomistic scale MD simulations are used to investigate the evolution of spinel-structured materials under particle irradiation. The interaction of highly energetic particles with matter is a fundamental scientific problem. The energy transferred from an energetic projectile to a target material can result in structural modifications of the material referred to as radiation damage. These changes occur at the atomistic scale and are directly related the material's stability and durability which are identifiable at the macroscopic level.

In many applications such as in nuclear waste storage, materials which exhibit minimal changes in their properties and for which long-term stability can be anticipated, are highly desirable. Due to a paucity of these materials, numerous experiments have been conducted on materials with different structures to determine their radiation tolerance. The underlying mechanisms which contribute to radiation tolerance can then be determined in order to design new materials with enhanced-radiation resistivity. Much effort has also been dedicated to investigate this phenomenon using different simulation techniques so that complex experimental observations can be understood.

The main purpose of this thesis is to investigate the structural modifications occurring in spinels when defects form in the structure due to a radiation event and to investigate the defect diffusion mechanisms in the material. Spinels belong to the class of ternary oxides with the general formula AB_2X_4, where A and B are cations and X is an anion. Magnesium aluminate spinel, $MgAl_2O_4$ is the main component of the spinel group and exhibits exceptional resistance to irradiation. The crystal structure of spinel is described in chapter 2. The various experimental studies of

irradiation in magnesium aluminate spinel are also reviewed.

The formation of defects by irradiation is characterised by time scales of the order of femtoseconds which cannot be monitored in real experiments. However, MD simulations are ideal to investigate dynamical events occurring on such short time and length scales. The ionic character of spinels requires special treatment of the Coulomb interactions for fast computation. The parallel algorithms employed in the MD code, including the algorithms for evaluating Coulomb forces, are introduced in chapter 3. These are essential for running large scale simulations. The results of defect formation in the energy regime of 0.4-10 keV are shown in chapter 4 for $MgAl_2O_4$ while the damage created in two other spinels, $MgGa_2O_4$ and $MgIn_2O_4$, is given in chapter 5.

The time scale problem of MD restricts the simulations to several picoseconds only. However, the diffusion of defects induced by radiation occurs over much longer time scales. We use temperature accelerated dynamics (TAD) [3] in order to determine the mechanisms and the corresponding energy barriers for point defects to diffuse in the three spinels. The TAD methodology and the results for point defect diffusion are given in chapter 6.

In chapter 7, the effect of low energy cascades in a MgO/Al_2O_3 system is investigated using MD simulations. The atomic rearrangement occurring at the interfacial region is analysed.

The main findings in this work are summarised in the final chapter together with some suggestions for future work.

Chapter 2

Spinel oxides

Minerals with the general formula AB_2X_4 (where A and B are cations and X is an anion), and which have the same crystal structure as magnesium aluminate spinel, $MgAl_2O_4$, form the spinel group. Spinels are ionic compounds which are widespread in nature and occur in various geological forms in the Earth's crust and upper mantle [4]. Many spinels show remarkable electronic and magnetic properties and are thus suitable for various technological applications such as superconductors and magnetic devices [5]. The ability of some ferrite spinels to exhibit different valence states makes them good electrical conductors while those spinels with a high melting point can be utilised as refractories [6]. Magnesium aluminate spinel is exceptionally popular because of its resistance to radiation and is therefore a potential candidate for a number of applications in radiation environments. In this chapter, an atomic description of the structure of these oxides and some general background is provided. Radiation damage experiments performed in $MgAl_2O_4$ are also reviewed.

2.1 The structure of spinel

Magnesium aluminate spinel is probably the most studied component of the spinel systems. Its structure consists of a face-centered cubic arrangement of anions that

contains two distinct sites, tetrahedral sites and octahedral sites, which are partially filled by cations. One unit cell consists of 8 $MgAl_2O_4$ formula units forming a structure that contains 64 tetrahedrally coordinated interstices (surrounded by 4 O^{2-}) and 32 octahedrally coordinated interstices (surrounded by 6 O^{2-}). In the normal spinel, one eighth of these 64 tetrahedral sites are occupied by the divalent Mg^{2+} ions and half of the 32 octahedral interstices are taken up by Al^{3+} ions. The remaining sites are left empty and are referred to as structural vacancies. The basic repeat units are shown in fig. 2.1 and span the lattice diagonally as illustrated by the corresponding pattern.

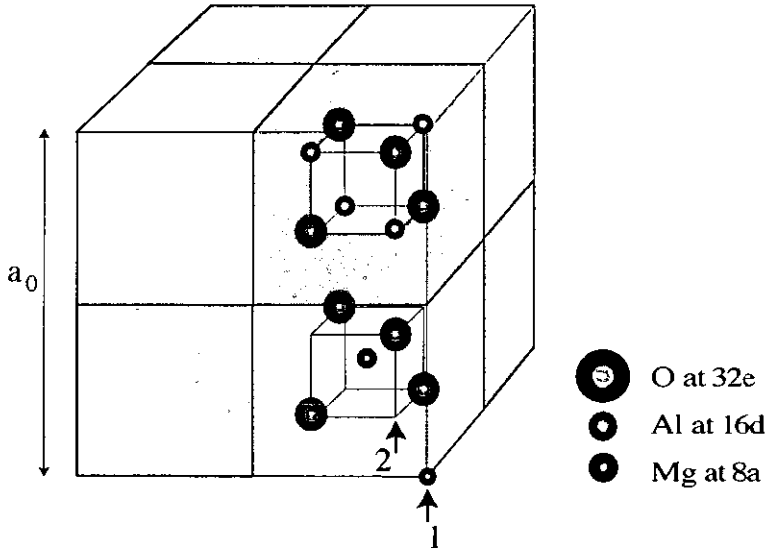

Figure 2.1: Unit cell of the normal $MgAl_2O_4$ spinel with lattice parameter a_0. The pattern indicated by the shading denotes cell repetition. The arrows indicate the two origins which can be used to describe atomic positions in the crystal.

Most of the spinel compounds have the $Fd3m$ space group symmetry (No. 227 in the International Tables) [7]. In that respect, the atomic positions are usually described using the Wyckoff notation [8] and by specifying the unit cell origin. Under this scheme, lattice sites with identical symmetry are referenced using a unique lowercase letter (eg. a, b, c,...). These letters are then prefixed by a number (eg.

1, 2, 3,...) indicating the number of equivalent sites or equipoints that exist in the unit cell. Spinel has 6 such equipoints at the fractional coordinates shown in table 2.1. In the description of these positions, the origin is conventionally set either on an occupied Mg-site, labelled 1 in fig. 2.1, or on an octahedral structural vacancy site, labelled 2 in fig. 2.1.

Table 2.1: Fractional coordinates of lattice sites in the $MgAl_2O_4$ spinel primitive cell. The positions of the anions depend on the parameter u (see section 2.1.1 for details). $u = 3/8$ when the origin is at a Mg-site, and, $u = 1/4$ when the origin is set at an octahedral vacancy. The abbreviations 'octa' and 'tetra' stand for octahedral and tetrahedral respectively, and the term 'vacancy' defines a structural vacancy or an unoccupied lattice site. The crystal structure is generated by repeating this cell according to a fcc lattice.

		Fractional coordinates of lattice sites	
Lattice site	Equipoint	Origin at Mg-site	Origin at octa. vacancy
Mg-site	8a	0,0,0; 1/4,1/4,1/4	1/8,1/8,1/8; 7/8,7/8,7/8
Tetra. vacancy	8b	1/2,1/2,1/2; 3/4,3/4,3/4	3/8,3/8,3/8; 5/8,5/8,5/8
Al-site	16d	5/8,5/8,5/8; 5/8,7/8,7/8; 7/8,5/8,7/8; 7/8,7/8,5/8	1/2,1/2,1/2; 1/2,1/4,1/4; 1/4,1/2,1/4; 1/4,1/4,1/2
Octa. vacancy	16c	1/8,1/8,1/8; 1/8,3/8,3/8; 3/8,1/8,3/8; 3/8,3/8,1/8	0,0,0; 0,1/4,1/4; 1/4,0,1/4 ; 1/4,1/4,0
O-site	32e	u,u,u; $u,\bar{u},\bar{u}$; $\bar{u},u,\bar{u}$; $\bar{u},\bar{u},u$; (1/4 - u),(1/4 - u),(1/4 - u); (1/4 + u),(1/4 + u),(1/4 - u); (1/4 + u),(1/4 - u),(1/4 + u); (1/4 - u),(1/4 + u),(1/4 + u)	u,u,u; $\bar{u},\bar{u},\bar{u}$; u,(1/4 - u),(1/4 - u); (1/4 - u),u,(1/4 - u); (1/4 - u),(1/4 - u),u; $\bar{u}$,(3/4 + u),(3/4 + u); (3/4 + u),$\bar{u}$,(3/4 + u); (3/4 + u),(3/4 + u),$\bar{u}$
Tetra. vacancy	48f	1/4,0,0; 0,1/4,0; 0,0,1/4; -1/4,0,0; 0,-1/4,0; 0,0,-1/4; 1/2,1/4,1/4; 1/4,1/2,1/4; 1/4,1/4,1/2; 0,1/4,1/4; 1/4,0,1/4; 1/4,1/4,0	3/8,1/8,1/8; 1/8,3/8,1/8; 1/8,1/8,3/8; -3/8,7/8,7/8; 7/8,-3/8,7/8; 7/8,7/8,-3/8; -1/8,1/8,1/8; 1/8,-1/8,1/8; 1/8,1/8,-1/8; 1/8,7/8,7/8; 7/8,1/8,7/8; 7/8,7/8,1/8

Using a Mg site as origin, the positions of the atoms can be described as Mg occupying equipoint 8a, Al at 16d and O at 32e while the structural vacancies are located at 16c (octahedral sites) and 8b and 48f (tetrahedral sites) [9]. The structure

is composed of alternate layers of Mg ions only and layers containing Al and O ions as shown in fig. 2.2. The nearest neighbour environment around each atom is schematically represented in fig. 2.3 showing the arrangement of the Al^{3+} ion with an octahedral coordination, the Mg^{2+} ion residing at a tetrahedral site and the O^{2-} ion with its four nearest neighbour cations.

Although the atomic positions are well defined at the above mentioned sites, there are three degrees of freedom associated with those positions in spinels. These are the anion parameter, u, the inversion parameter, i, and the lattice parameter, a_0.

2.1.1 The anion parameter, u

The AB_2O_4 system can accommodate a wide range of cations with varying ionic radii within its structure. These can range from 0.57 - 0.66 Å for the divalent A-site cation (e.g. Mg, Mn, Fe, Ni, Zn) and 0.53 - 0.65 Å for the trivalent B-site cation (e.g. Al, Cr, Fe) [4]. The size of the cations in the spinel structure affects the perfect ordering of the anions, since larger cations would require interstices with larger volumes as illustrated by the diagram in fig. 2.4.

The anion parameter, u, is the fraction of the unit cell edge defining the position of the oxygen ion at fractional coordinates (u, u, u). It provides a measure of the movement of the anions from their ideal sites. For an ideal closed packed oxygen arrangement with the unit cell origin on an A-site cation, $u = 0.375$ (or 0.250 when the origin is an octahedral structural vacancy), and the tetrahedral sites are smaller than the octahedral sites. In real systems, this u value is larger and the oxygen ions move away from their perfect sites in order to balance the volume of each of the tetrahedral and octahedral interstices relative to the cationic radii. This results in an outward oxygen dilatation along the <111> direction from the occupied tetrahedral cation as illustrated by the arrows in fig. 2.4 (b). This distortion of the anion sublattice has

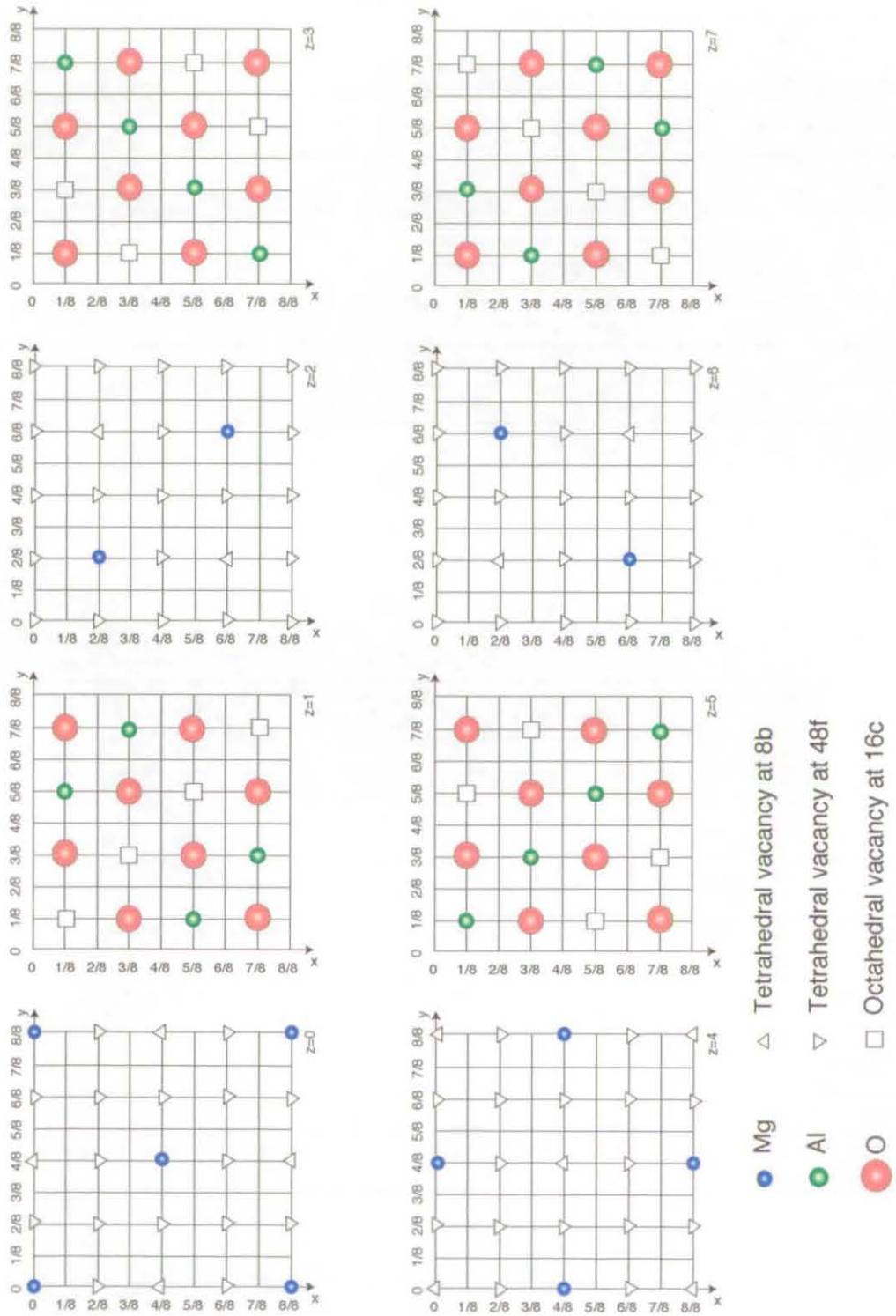

Figure 2.2: Interstice occupancies as a function of height in spinel (Adapted from Sickafus *et al.* [9]). The layers are stacked at intervals of $a_0/8$. The positions of the anions are defined by the u parameter, here $u = 3/8$.

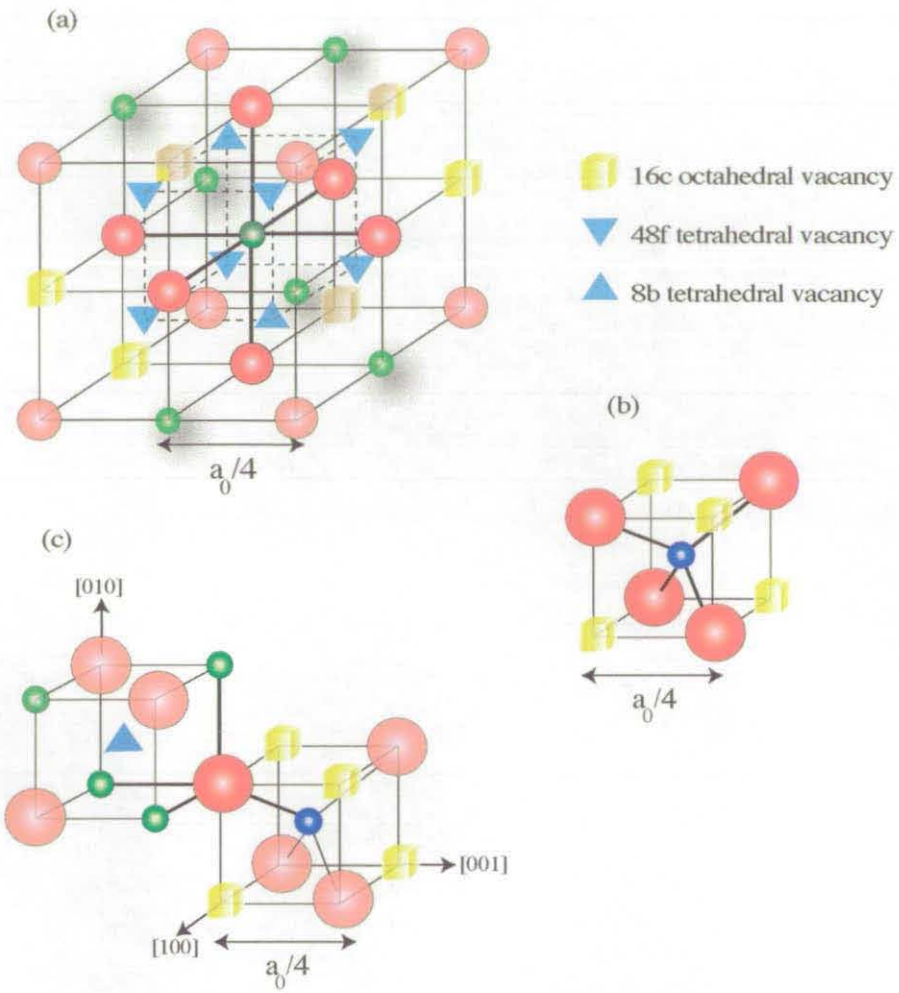

Figure 2.3: Nearest neighbour configurations in the spinel structure for an (a) Al^{3+} ion, (b) Mg^{2+} ion, and (c) O^{2-} ion. Al ions are represented as green spheres, Mg ions are coloured blue and O ions are shown in red.

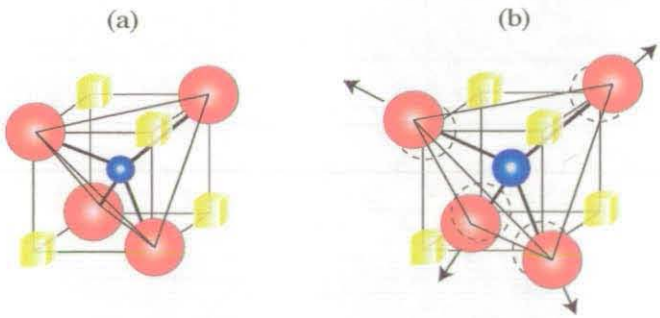

Figure 2.4: (a) Tetrahedral environment with a perfect oxygen arrangement. (b) The oxygen ions are dilated along $< 111 >$ due to a bigger cation.

direct consequences on the cation-anion bond lengths and the interstices' geometries and volumes.

2.1.2 The inversion parameter, i

In normal spinels, as described above, the divalent cations (Mg^{2+}) reside at tetrahedral sites whereas the trivalent cations (Al^{3+}) occupy octahedral sites. However, under different conditions of temperature and pressure, the divalent cations can interchange sites with the trivalent cations, resulting in disordering on the cation sublattice. This cation-site interchange is characterised by the so-called inversion parameter, i, defined as the fraction of tetrahedral sites occupied by trivalent cations and ranges from 0 to 1. Spinel compounds with $i = 0$ are said to be normal, whereas those with $i = 1$ are referred to as inverse spinels. In the latter case, all the divalent cations occupy octahedral sites whereas half of the trivalent cations remain at their octahedral sites and the other half occupy tetrahedral sites. Different cation arrangements can also yield to intermediate i values between 0 and unity while a random cation arrangement occurs when $i = \frac{2}{3}$.

An example of this cation mixing mechanism in the normal spinel is represented by equation 2.1, with a Mg ion interchanging site with an Al ion, forming a pair of cation disorder defects called antisites. In this equation and throughout this thesis, the defects are denoted using the Kröger-Vink scheme [10].

$$Mg^{\times}_{Mg} + Al^{\times}_{Al} \rightarrow Mg'_{Al} + Al^{\cdot}_{Mg} \tag{2.1}$$

In reality, the inversion parameter of natural samples of $MgAl_2O_4$ is only close to zero at low temperatures whereas for synthetic samples the inversion parameter lies between $0.2 - 0.6$ [11]. Cation disorder increases with increasing temperature and can also be triggered by irradiation [12]. However, some spinels have the inverse structure under normal conditions, while others have intermediate/partial inversion depending

on their chemical compositions. For example, $MgIn_2O_4$ is inverse ($i = 1$), whereas $MgGa_2O_4$ is partially inverse [13, 14]. A broader list of partially inverse and inverse spinels is given in [15].

2.1.3 The lattice parameter, a_0

The lattice parameter, a_0, is a function of the average of the A-site and B-site cationic radii and typically ranges from 8 - 9 Å. However, the oxygen sublattice has a repeat unit which is half that of the spinel unit cell as represented by one of the octants of fig. 2.1.

The lattice parameter, a_0 decreases with increasing i. This was observed experimentally under thermal treatment in $MgAl_2O_4$, showing a small reduction in the value a_0 of the order of 0.0027 Å with cation disordering triggered by a rise of 500 K in the temperature [16]. Such a trend was also seen in several computer modelling techniques whereby the formation of cation antisites resulted in a small reduction of the lattice parameter [17].

Related to the increase in cation disorder, the anion parameter is also subject to variations, but decreases instead. This is because the tetrahedral sites occupied by the smaller Al^{3+} ions, become smaller in volume whereas the octahedral sites expand due to the presence of the larger Mg^{2+} ions [18]. Fluctuations in the anion parameter can therefore be regarded as an indication of cation disorder.

2.1.4 Cation-anion bond and cation disorder

The normal spinel structure is composed of MgO_4 tetrahedra and AlO_6 octahedra. Neglecting the effect of the oxygen parameter u, the relative sizes and shapes of these polyhedra depend on their cation-anion bond lengths. However, with cation disorder, these bonds can expand or shrink depending mainly on the magnitude of the central cation's valency and how this is shared with the oxygen ions around the

cation as postulated by Pauling. According to him, the strength of an electrostatic bond is defined as a cation's valence charge divided by its coordination number [19]. Therefore, the strength of the Mg^{2+}–O^{2-} bond for a Mg^{2+} occupying a tetrahedral site (coordination 4) is different from that of a Mg^{2+} occupying an octahedral site (coordination 6). Pauling also states that "*In a stable structure, the charge of the anion tends to compensate the strength of the electrostatic bonds reaching to it from the cations...*".

Thus, in the normal spinel, the tetrahedrally coordinated Mg^{2+} shares its +2 charge with its 4 nearest neighbour oxygen ions whereas the octahedrally coordinated Al^{3+} shares its +3 charge with its 6 nearest neighbour oxygen ions. Hence, each oxygen gets a charge of $+\frac{2}{4}$ in a Mg^{2+}–O^{2-} bond and $+\frac{3}{6}$ in an Al^{3+}–O^{2-} bond. Since each oxygen is bonded to 1 Mg^{2+} and 3 Al^{3+} in the normal structure, the total charge contribution from these cations is $\frac{2}{4} + 3\times\frac{3}{6} = +2$ which is balanced exactly by the -2 charge of the oxygen. Therefore, according to Pauling, this configuration is stable.

However, in the presence of a cation antisite defect, the charges shared between the antisite and its nearest neighbour anions in the corresponding polyhedra no longer balance. If the overall charge contribution of the nearest neighbour cations on any oxygen forming this polyhedra is negative (or positive), then this oxygen is said to be under-bonded (or over-bonded). Consequently, the under-bonded oxygen ions will have a smaller bond length with their nearest cation neighbours, whereas over-bonded oxygen ions will have a longer bond length with their cation neighbours than usual. This effect is particularly important in spinels with $i > 0$ and yield to a complex electrostatic field.

2.2 Radiation damage in spinel

On historical backgrounds, spinels have not always been subject to scientific attention, but due to their appearance, they have been used as gemstones for a long period of

time. The name spinel originates from the latin word "spina", meaning "little thorn", most probably because of its sharp corners in crystalline form. Spinels can exhibit a variety of colours, especially red and blue. The famous Imperial State Crown of England, has a big spinel (length of about 5.08 cm and weighing 140-ct) known as the Black Prince's ruby on its front as shown in fig. 2.5. However, over the past decades, many spinels have been studied for scientific purposes - one such example is $MgAl_2O_4$.

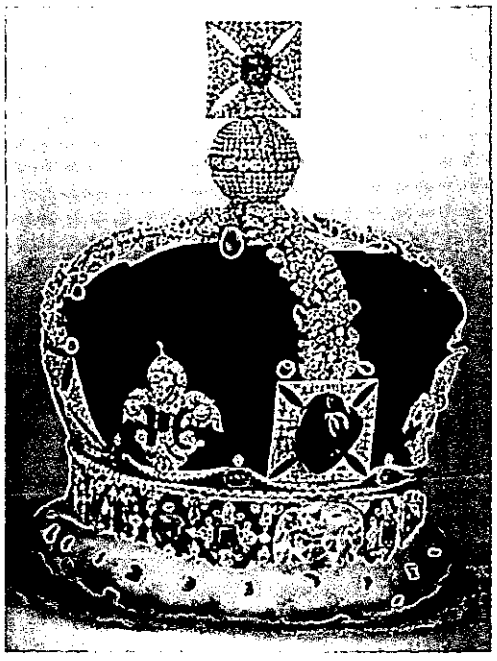

Figure 2.5: The Imperial State Crown of England is decorated by a red spinel at the front. (Photo taken from www.palagems.com/spinel_ball.htm)

$MgAl_2O_4$ spinel has been proposed as a potential candidate in many nuclear applications because it maintains a relatively stable structure under irradiation. In such environments, materials are subjected to constant irradiation and their resistance to that bombardment is a key to their performance. Because of this, the effects of radiation on the microstructure of spinel has been extensively studied by various experimental techniques to assess its radiation tolerance.

time. The name spinel originates from the latin word "spina", meaning "little thorn", most probably because of its sharp corners in crystalline form. Spinels can exhibit a variety of colours, especially red and blue. The famous Imperial State Crown of England, has a big spinel (length of about 5.08 cm and weighing 140-ct) known as the Black Prince's ruby on its front as shown in fig. 2.5. However, over the past decades, many spinels have been studied for scientific purposes - one such example is $MgAl_2O_4$.

Figure 2.5: The Imperial State Crown of England is decorated by a red spinel at the front. (Photo taken from www.palagems.com/spinel_ball.htm)

$MgAl_2O_4$ spinel has been proposed as a potential candidate in many nuclear applications because it maintains a relatively stable structure under irradiation. In such environments, materials are subjected to constant irradiation and their resistance to that bombardment is a key to their performance. Because of this, the effects of radiation on the microstructure of spinel has been extensively studied by various experimental techniques to assess its radiation tolerance.

Spinel has demonstrated good resistance under neutron irradiation. Clinard and co-workers found that the material was resistant to swelling as compared to MgO and Al_2O_3 under fluences of $\approx 2 \times 10^{26}$ n/m^2 ($E > 0.1$ MeV) and that the irradiated structure contained interstitial loops which could not develop into dislocation networks [20, 21]. The spinel structure was found to be invariant to dimension changes and swelling under neutron exposure with fluences ranging from 2.2 to 24.9 $\times$ 10^{26} n/m^2, and within the temperature range of 650-1000 K [22]. Sickafus *et al.* found that the spinel microstructure remained relatively stable under neutron irradiation to fluences $> 5 \times 10^{26}$ n/m^2, resulting in a large amount of cation disordering rather than point defect accumulation [23]. These investigations showed that the radiation tolerance of spinel was primarily attributed to a high vacancy-interstitial recombination rate and to the ability of Mg and Al ions to swap lattice sites (cation disordering) thereby maintaining a crystalline structure.

However, several ion-irradiation experiments showed that the material transformed to an intermediate crystalline phase distinct from spinel prior to amorphisation. Yu *et al.* first observed signs of amorphisation during irradiation by 400 keV Xe^{2+} at 100 K to a dose of 1×10^{20} Xe/m^2 [24]. In their experiment, they found three distinct layers in the irradiated $MgAl_2O_4$ sample: an uppermost amorphous region, followed by a radiation-damaged crystalline phase and an undamaged region. This intermediate crystalline phase was also observed in [25, 26, 27] and had a repeat unit half that of the spinel unit cell. Identifying correctly this new crystalline phase was crucial in order to understand firstly, how the spinel structure underwent this transformation and, secondly, from there, what factors contributed to the full amorphisation of the material. The repeat unit of the metastable phase corresponded to the anion sublattice spacing of spinel indicating that the anion sublattice retained its periodicity whereas it was believed that the cations were randomised on both the tetrahedral and octahedral sublattices. However, detailed investigations of the diffraction patterns of this region revealed that it corresponded to a disordered rocksalt (NaCl) structure

whereby cations were found on the octahedral sites and the tetrahedral sites were empty [26]. Based on these experimental observations, it is believed that amorphisation would occur via the accumulation of cation disorder defects (antisites) and dislocation loops, and eventually leading to the destruction of the anion sublattice.

Recent theoretical *ab-initio* work by Gupta [28] showed that a normal $MgAl_2O_4$ spinel can transform to an inverse spinel via cation disordering much more readily than when the Mg^{2+} cations are directly placed at the octahedral vacancy sites (16c sites) in a rock-salt structural arrangement. The latter case could yield to another rock-salt structure whereby 75 % of the metal atom sites are randomly occupied. However, the various ways in which these sites are populated by the cations are not well characterised.

The above observations show that cation disordering plays an important role in the structural properties of spinel under irradiation. This is a preferred mechanism for defect accommodation since it maintains a stable crystal structure as seen under neutron irradiation. The presence of more than two ions in the spinel lattice with different atomic masses and valencies could also be a significant factor contributing to the material's radiation tolerance as compared to simple oxides like MgO and Al_2O_3. Moreover, the structural vacancies could provide an efficient route for interstitial diffusion, essential for interstitial-vacancy recombination. However these processes/mechanisms are difficult to investigate in the usual experiments because of their microscopic length and time scales. Many theoretical investigations using a variety of modelling techniques are necessary to address the above mentioned issues and to provide better insight of the effects of radiation on the microstructure of spinel.

Chapter 3

Molecular dynamics methodology

Molecular dynamics (MD) is an established method that models the evolution in time of a system of N-interacting particles. The main task of MD is the time-integration of Newton's laws of motion by assuming that the interaction between the particles is governed by a pre-defined potential energy function. MD has been successfully employed in many areas of science to address fundamental issues such as protein motion in solutions, friction and wear of materials, and the effects of radiation in materials [29, 30, 31].

This chapter provides an overview of the basic components of a molecular dynamics programme. The discussion is related to the physical problem of interest, which is the dynamical process of damage production in the spinel microstructure. We first introduce the force field describing the atomic interactions in the structure, then the procedures involved in advancing the system in time. The main aspects of the parallel algorithms implemented in the MD code are also presented. This chapter forms a prelude to chapters 4, 5 and 7 whereby collision cascade simulations are investigated.

3.1 Introduction

The modelling of atomic interactions can be investigated either quantum mechanically, by treating explicitly electronic and nuclear variables for each atom using first principles or *ab-inito*, or alternatively, by considering the atoms as classical particles within the force field of a potential energy function. Classical molecular dynamics forms part of the latter category, whereby at any point in time, the atomic configuration is specified by the positions and momenta of the individual particles. As time progresses, this configuration is adjusted such that the system's dynamics are captured over a certain period of time. Semi-empirical methods, such as the tight binding model, incorporate electronic structure calculations into molecular dynamics simulations through an empirical Hamiltonian [32]. Thus, semi-empirical methods are intermediate techniques between *ab-initio* and classical methods. The work presented in this thesis is based on classical molecular dynamics.

MD assumes that the net force $\mathbf{F}_i$, on each atom i, at time t, is given by Newton's second law of motion:

$$\mathbf{F}_i = m_i.\mathbf{a}_i, \tag{3.1}$$

where m_i is the mass and $\mathbf{a}_i$ is the acceleration of the particle. The acceleration can be expressed in terms of the atomic position $\mathbf{r}_i$ as follows,

$$\mathbf{a}_i = \frac{d^2\mathbf{r}_i}{dt^2}, \tag{3.2}$$

such that, under the current force, the subsequent position $\mathbf{r}_i$ of each atom as the time is incremented to $t + \delta t$ can be determined by applying a suitable integrating scheme (discussed in section 3.3.1). In order to capture the system's dynamics, this procedure of force evaluation and numerical integration is repeated at every time step. Each of these time steps is of the order of 1 femtosecond thereby limiting the total simulation time to several tens of picoseconds even on the fastest computers available.

The complexity of the atomic interactions in the system relies on the force field employed. The forces are generally assumed to be conservative and thus can be expressed as the negative gradient of a potential energy function, V. This function describes the energy given the system's configuration and is dependent on the positional vectors of the atoms $\{\mathbf{r}_i;\ i = 1, 2, ..., N\}$. Thus, for any atom i, eqn. 3.1 can be rewritten as follows:

$$m_i.\mathbf{a}_i = -\nabla_{\mathbf{r}_i} V(\mathbf{r}_1, \mathbf{r}_2, ..., \mathbf{r}_N). \tag{3.3}$$

If initial atomic positions are known $\{\mathbf{r}_i;\ i = 1, 2, ..., N\}$, and their interactions fully described by the potential energy function V, the MD scheme finds the trajectory of each atom by solving eqns. 3.2 and 3.3.

However, as in any other experiment or computer modelling technique, it is essential to prepare the system before running the MD simulation. This involves, the potential energy function selection, setting up the initial configuration of the crystal structure, and applying the necessary constraints during the simulation. Eventually, by using a suitable visualisation tool/software, the results can be scrutinised to identify microscopic details of the dynamical process.

3.2 The potential energy function

The major component of the atomistic model is the potential energy function which approximates the quantum mechanical interactions of electrons and nuclei in the system. The complexity of these interactions are incorporated in the potential energy function, which is commonly expressed as follows:

$$V = \sum_i \sum_j{}' V_{ij}(\mathbf{r}_i, \mathbf{r}_j) + \sum_i \sum_j \sum_k{}' V_{ijk}(\mathbf{r}_i, \mathbf{r}_j, \mathbf{r}_k) + ... \tag{3.4}$$

Each term in eqn. 3.4 represents mathematical expressions which describe specific features in the potential energy hypersurface. The first term is the contribution of the interactions between pairs of atoms i and j, and V_{ij} describes the energy profile between them as a function of their distance apart. The second term involves interactions between triplets i, j and k, and characterises bond bending effects. Three-body interactions become important in systems with covalent bonding, in metals and semiconductors [33]. Higher order terms are too small compared to the two-body and three-body terms and are usually omitted in MD simulations [34]. The prime on the summation signs indicates that each distinct pair (or triplet) is not counted twice.

There is a wide selection of potential energy functions available for a broad range of materials. Because of the ionic character of the spinel compounds considered in this thesis, the model of interest has to properly describe this ionic crystalline cohesion. Here, atoms are treated as point-like charges forming an ordered arrangement of alternate positive ions and negative ions held together by two competing interactions:

- the Coulomb attraction between these cations and anions, and,

- a short range, repulsive field that prevents the ions from collapsing into each other.

The potential energy function V can be expressed as follows:

$$V = V_{Coul} + V_{SR}, \tag{3.5}$$

where V_{Coul} denotes the standard Coulomb potential and V_{SR} represents the short range repulsive part which can be modelled empirically. Only pair potentials are used in the simulations presented in this thesis. The functional form of these potentials are introduced in the following subsections.

3.2.1 Coulomb interactions

It is well known in electrostatics that "*like charges repel, unlike charges attract*". This phenomenon was studied by the French scientist Charles-Augustin de Coulomb (1785), who discovered an inverse relationship on the force between two charges and the square of their distance. Later in time, came the potential energy concept of this charge-charge interaction, which can be expressed mathematically as follows:

$$V_{Coul}(r_{ij}) = \frac{z_i z_j e^2}{4\pi\epsilon_0 r_{ij}}, \tag{3.6}$$

where z_i and z_j are the valencies of the interacting ions i and j, r_{ij} the distance between them, e is the electronic charge ($e = 1.602 \times 10^{-19}$ C), and ϵ_0 represents the permittivity of free space ($\epsilon_0 = 8.854 \times 10^{-12}$ C^2 N^{-1} m^2). In a system of N ions, the total potential energy contribution due to the electrostatic interactions is given by:

$$V_{Coul}(r_{ij}) = \sum_{i}^{N} \sum_{j>i}^{N} \frac{z_i z_j e^2}{4\pi\epsilon_0 r_{ij}}. \tag{3.7}$$

The Coulomb potential falls off slowly with r_{ij}, such that the interaction between two particles can be felt at distances of up to 70 nm [35]. For this reason, the summation involves all ion pairs in the crystal in contrast with the short-range potentials discussed below.

3.2.2 Buckingham potential

The attraction between two atoms or ions of opposite charges within an interaction range gradually becomes repulsive as they come closer and closer. This is due to the nuclear repulsion between the atomic cores of the interacting pair and to the so called Pauli effect. The latter effect results from the electronic cloud overlap between the two ions which prevents them from collapsing into one another. The Born-Mayer potential models this repulsive interaction prevailing at short pair separation and is

given by the function:

$$V(r_{ij}) = A_{ij}e^{-\frac{r_{ij}}{\rho_{ij}}}, \tag{3.8}$$

where the parameters A_{ij} and ρ_{ij} are dependent on the two interacting ions. The Buckingham potential results from the addition of an attractive van der Waals tail to the Born-Mayer potential as shown:

$$V(r_{ij}) = A_{ij}e^{-\frac{r_{ij}}{\rho_{ij}}} - C_{ij}r_{ij}^{-6}, \tag{3.9}$$

where the parameter C_{ij} also varies according to the interacting species. The Buckingham potential is widely used in the modelling of ionic systems to describe short-range interactions [36]. The simplicity of this potential has contributed to its popularity. Additionally, the interaction range of this term is small and thus, the computation can be done efficiently.

3.2.3 Ziegler-Biersack-Littmark potential

The kinetics involved when modelling high-energy collision events should account for the significant internuclear repulsion induced at very short pair separations. At normal atomic distances, the electronic shells effectively screen the nuclei and to some extent, take part in the chemical bonding. However, during an energetic collision the impact is huge and the electronic clouds are dispersed and provide no more shielding. This repulsive potential between the nuclei then becomes essentially Coulombic and has the following form:

$$V(r_{ij}) = \frac{1}{4\pi\epsilon_0}\frac{Z_iZ_j}{r_{ij}}\phi\left(\frac{r_{ij}}{a_{ij}}\right), \tag{3.10}$$

where Z_i and Z_j are the atomic numbers of the interacting particles, ϕ is the screening function which incorporates the electronic shielding of the nuclei, and a_{ij} denotes the screening length for the interaction. The idea here is that $\phi \rightarrow 1$ as $r_{ij} \rightarrow 0$ such that the screening becomes less significant as the two nuclei come closer. Several

models for the screening function have been proposed. Among those in the literature, the functions proposed by Bohr, Thomas-Fermi, Molière, Lenz-Jensen and Ziegler-Biersack-Littmark (ZBL) are often encountered [37].

The ZBL potential [38] is widely used for atomic collision studies because it has been found to be more closely in agreement with experiment [39]. Here, the screening function $\phi(x)$ is given by:

$$\phi(x) = 0.1818e^{-3.1998x} + 0.5099e^{-0.9423x} + 0.2802e^{-0.4029x} + 0.02817e^{-0.2016x}. \quad (3.11)$$

The coefficients in eqn. 3.11 result from a fitting procedure to quantum mechanical calculated data. The screening distance depends on the atomic numbers of the colliding pair and relates to the equation:

$$a_{ij} = \frac{0.88534a_0}{Z_i^{0.23} + Z_j^{0.23}}, \quad (3.12)$$

where $a_0 = 0.529$ Å (Bohr radius for a H atom).

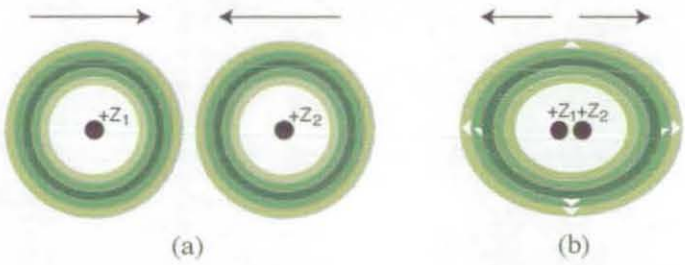

Figure 3.1: Schematic representation of the short-range repulsive interactions between two atoms colliding with high energies. (a) The nuclei are shielded by their electrons. (b) The electron cloud is dispersed during a collision event exposing the atomic cores to a strong Coulombic repulsion.

3.2.4 Spinel potential used in the MD code

The ionic spinel crystal is modelled as an ordered array of point masses with formal charges. The interactions are calculated by a pairwise potential consisting of the stan-

dard Buckingham potential for short range interactions, and the Coulomb potential for the long range electrostatic field. Because of the energetic collisions encountered in this work, the potential energy function is joined to the ZBL potential for short particle-particle separation by a splining function, $g(r_{ij})$. A smooth cutoff of the Buckingham potential is also implemented via the function $h(r_{ij})$. This combined potential energy function, $V(r_{ij})$, is given by eqn. 3.13.

$$V(r_{ij}) = \begin{cases} \text{ZBL} & r_{ij} < r_a; \\ g(r_{ij}) & r_a \leq r_{ij} < r_b; \\ A_{ij}e^{-\frac{r_{ij}}{\rho_{ij}}} - \frac{C_{ij}}{r_{ij}^6} + V_{Coul}(r_{ij}) & r_b \leq r_{ij} < r_c; \\ h(r_{ij}) \times \left(A_{ij}e^{-\frac{r_{ij}}{\rho_{ij}}} - \frac{C_{ij}}{r_{ij}^6} \right) + V_{Coul}(r_{ij}) & r_c \leq r_{ij} < r_0; \\ V_{Coul}(r_{ij}) & r_{ij} \geq r_0, \end{cases} \tag{3.13}$$

The potential parameters A_{ij}, ρ_{ij} and C_{ij} implemented in the MD code are reported in table 3.1 and describe the pair interactions in the three spinels $MgAl_2O_4$, $MgGa_2O_4$ and $MgIn_2O_4$. These parameters were obtained from the Atomistic Simulation Group of Imperial College [40, 41]. Because of the relatively short cationic radii, the cation-cation interactions show no polarisability and are treated as being purely Coulombic, such that A_{ij} and C_{ij} are equal to zero. For the interactions in the latter case, the spline connects to the ZBL potential at a pair separation of ≈ 0.40 Å and to the V_{Coul} potential at ≈ 1.05 Å. The potential used in this work for $MgAl_2O_4$ predicts the correct defect structures as *ab-initio* calculations. This potential has also been employed to investigate the variation in the lattice parameter of magnesium aluminate spinel as a function of cation disorder [17].

The lattice parameters resulting from our model are in good agreement with experimental data in all three spinels as shown in table 3.2. The lattice energy and volume per molecule of magnesium aluminate spinel show good agreement with those

Table 3.1: Buckingham potential function parameters for magnesium aluminate, magnesium gallate and magnesium indate spinels.

	A_{ij} (eV)	ρ_{ij} (Å)	C_{ij} (Å^{6}eV)	r_a(Å)	r_b(Å)	r_c(Å)	r_0(Å)
Mg–O	1279.69	0.2997	0.0	0.15	0.80	4.8	5.0
O–O	9547.96	0.2192	32.0	0.20	1.50	7.2	7.4
O–Al	1374.79	0.3013	0.0	0.15	0.65	4.8	5.0
O–Ga	1625.72	0.3019	0.0	0.15	0.65	4.8	5.0
O–In	1595.65	0.3296	7.4	0.45	1.10	4.8	5.0

predicted by the Bush *et al.* potential which includes shell polarisability [45]. The bulk modulus in $MgAl_2O_4$ is overvalued by about 39 % as compared to experimental data. This is because the structural properties of the materials were used during the fitting procedure and not their elastic properties.

Table 3.2: Calculated bulk properties of the three spinels. a_0 denotes the lattice parameter, i, the inversion parameter, E_L and V are the lattice energy and volume per spinel molecule. K denotes the bulk modulus.

Spinel	a_0 (Å)	i	E_L (eV/mol.)	V (Å/mol.)	K (GPa)
$MgAl_2O_4$	8.12 (8.14[a], 8.08[b])	0.0 (0.07[b])	–201.79 (–200.51[a])	66.97 (67.52[a])	272 (196[c])
$MgGa_2O_4$	8.31 (8.28[b])	0.5 (0.67[b])	–196.57	71.73	374
$MgIn_2O_4$	8.85 (8.81[b])	1.0 (1.0[b])	–181.81	86.64	238

[a] Ref. [42]: Chen *et al.* using the Bush *et al.* potential.
[b] Ref. [43]: Hill *et al.* (experiment).
[c] Ref. [44]: Kruger *et al.* (experiment).

The splining function $g(r_{ij})$ is a 5th order polynomial of the form:

$$g(r_{ij}) = e^{(f_1+f_2 r_{ij}+f_3 r_{ij}^2+f_4 r_{ij}^3+f_5 r_{ij}^4+f_6 r_{ij}^5)}, \tag{3.14}$$

where the constants f_k (k = 1,.., 6) are listed in table 3.3. These are derived by assuming that at the point of intersection of the spline to the ZBL potential (at r_a), and at the other point where the spline intersects the outer potential (at r_b), the

functions, their first and second derivatives are all continuous. The numerical values of r_a and r_b were chosen in order to reproduce a smooth transition in the potential energy. This can be illustrated in figs. 3.2, 3.3 and 3.4. The repulsive parts of the trivalent cation B-O pair potentials are shown in fig. 3.5. It can be clearly seen from this curve that the indate has a much steeper repulsion than the gallate which is also steeper than the normal spinel.

The cut-off function $h(r_{ij})$ in eqn. 3.15, ensures that the Buckingham potential gradually becomes zero at r_0 over the range $d = 0.2$ Å.

$$h(r_{ij}) = \begin{cases} 1 & r_{ij} < r_c; \\ \frac{1}{2}\left(1 + \cos \pi \frac{r_{ij} - r_c}{d}\right) & r_c \leq r_{ij} < r_0; \\ 0 & r_{ij} \geq r_0. \end{cases} \tag{3.15}$$

Table 3.3: The parameters for the spline.

	f_1	f_2	f_3	f_4	f_5	f_6
Mg–Mg	14.4507	-47.7977	122.4210	-175.9999	125.1304	-34.1480
Mg–Al	10.6531	-17.0984	27.9501	-36.8467	28.3526	-8.5504
Mg–O	11.0765	-31.3878	118.9207	-302.6137	367.5647	-167.4741
Al–Al	10.3578	-112.8183	9.4511	-1.2318	-1.0544	0.1604
Al–O	11.5733	-41.0565	200.9594	-614.9430	875.5115	-464.8603
O–O	9.9306	-17.4669	25.3341	-19.0023	6.6210	-0.8289
Ga–Ga	13.4778	-30.1638	80.1403	-135.7550	109.9295	-32.7604
Ga–O	12.3580	-39.8836	185.4654	-545.5733	736.6578	-365.7662
Ga–Mg	12.2051	-25.6830	62.8748	-103.3191	83.2123	-24.8280
In–In	15.0978	-39.1426	116.5600	-204.9417	166.9734	-49.6767
In–O	12.5481	-25.6434	54.0561	-62.4669	37.3255	-8.9238
In–Mg	13.0074	-30.0841	80.6271	-137.0188	111.0039	-33.0724

3.3 System integration

The evolution of an N-body system under a certain force field requires approximate numerical methods to integrate Newton's equation in time. This is achieved by using

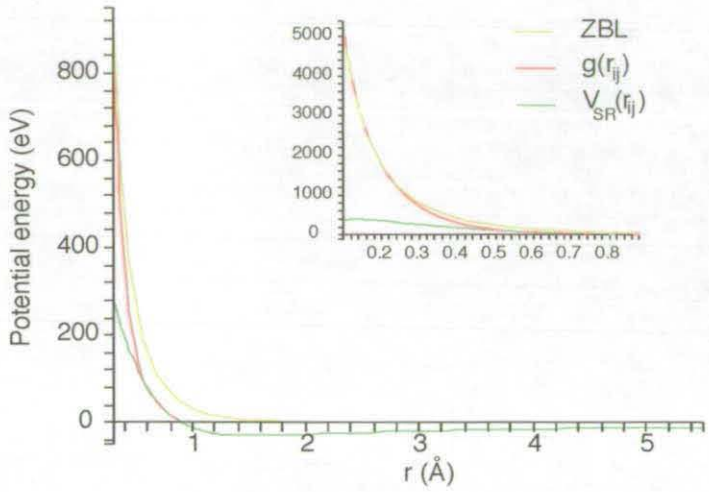

Figure 3.2: The Mg-O interaction potential consisting of the smoothly joined ZBL potential to the outer potential, denoted as V_{SR} (without the cut-off function). The points of intersection are at $r_a = 0.15$ Å and $r_b = 0.80$ Å.

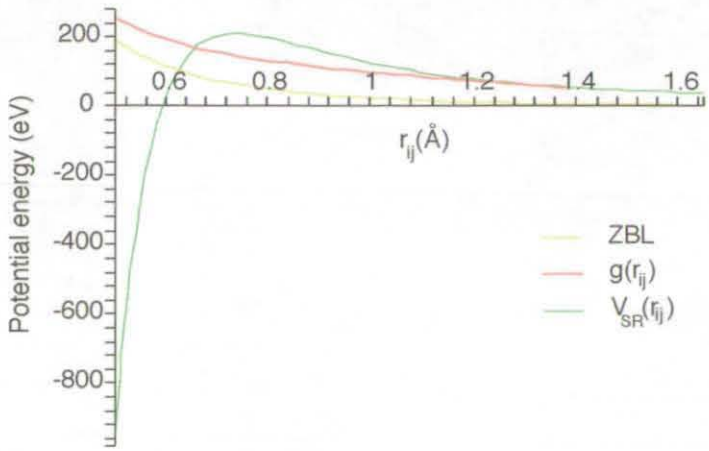

Figure 3.3: The potential energy variation for the oxygen-oxygen interaction. The outer potential intersects the spline at $r_b = 1.50$ Å which itself links smoothly to the ZBL potential at $r_a = 0.2$ Å (not captured in the graph). This results in a repulsive wall at very close spacing.

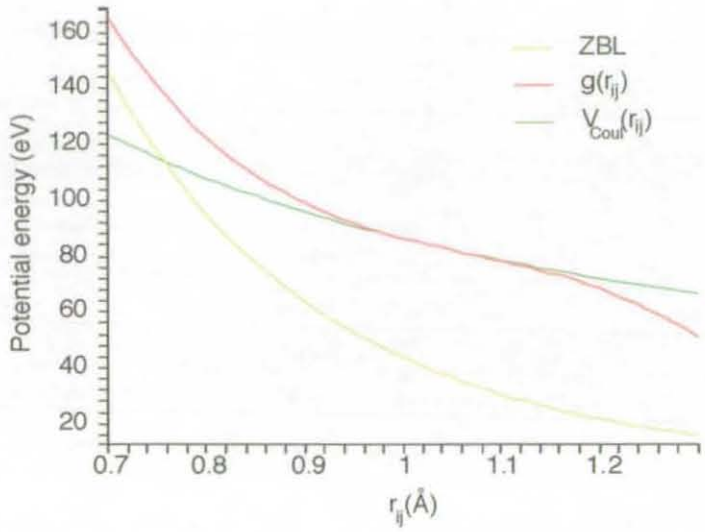

Figure 3.4: Coulomb potential splined to the ZBL potential for the Mg-Al interaction in $MgAl_2O_4$ spinel. $r_a = 0.3$ Å (not shown in the graph) and $r_b = 1.05$ Å.

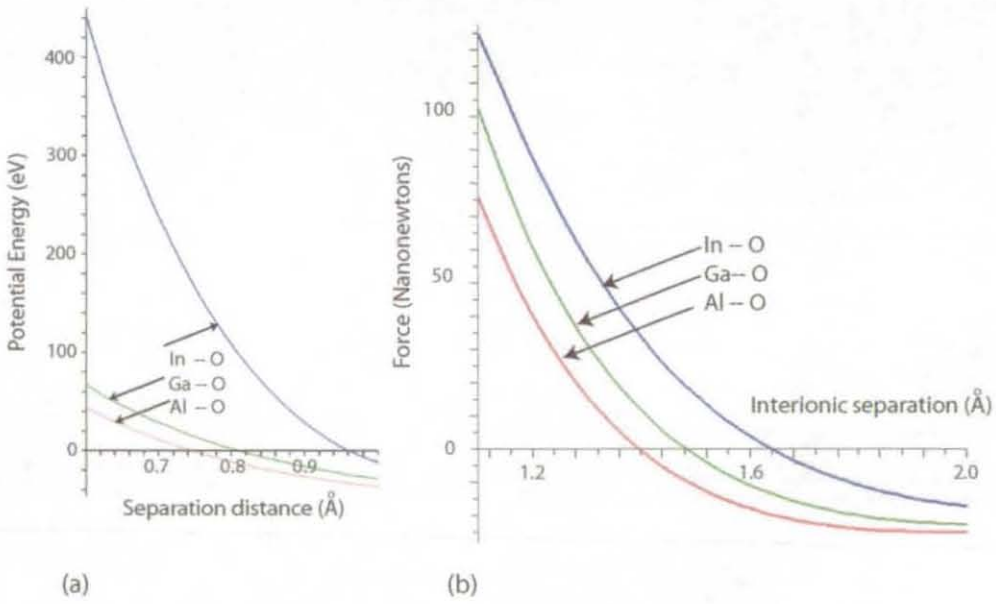

Figure 3.5: (a) The repulsive part of the pair interaction potential, including the Buckingham terms, the Coulombic terms and the ZBL spline for the B-O interaction in the range 0.6 - 1.0 Å. (b) The pair interaction forces of the potentials near the equilibrium separation.

finite difference algorithms which use the current forces acting on the particles to estimate their atomic position and velocity vectors as the time is incremented by δt. The most common integration algorithms used in MD are the leapfrog scheme and those proposed by Beeman and Verlet [46]. In the first subsection we present the velocity-Verlet method, which is implemented in our MD code. In order to advance the system in time, a variable time step controller is employed. This provides a range of values for δt as discussed in the second subsection. In the last subsection, the list of parameters which can be monitored during the simulation is presented.

3.3.1 Velocity-Verlet integration algorithm

For his simulations on liquid argon, Loup Verlet [47] introduced an integration scheme known as the Verlet algorithm, derived from Taylor series expansions. Here, the atomic positions, $\mathbf{r}_i$, and velocities, $\mathbf{v}_i$, are updated as follows:

$$\mathbf{r}_i(t+\delta t) = 2\mathbf{r}_i(t) - \mathbf{r}_i(t-\delta t) + \delta t^2 \mathbf{a}_i(t), \tag{3.16}$$

$$\mathbf{v}_i(t) = \frac{\mathbf{r}_i(t+\delta t) - \mathbf{r}_i(t-\delta t)}{2\delta t}. \tag{3.17}$$

The acceleration, $\mathbf{a}_i$, in eqn. 3.16, is obtained from the force field at time t and is evaluated first. The Verlet algorithm requires stored information at t and $t-\delta t$ in order to advance the coordinates at time $t+\delta t$. This means extra storage needs to be available for the position vectors. Another feature of this method is that the velocity updates lag behind by one interval as compared to the atomic positions. In terms of accuracy, the error is of the order of δt^4 in calculating the new coordinates, and is of the order of δt^2 for the velocities.

A variant of the Verlet algorithm was proposed by Swope *et al.* [48] and is termed the velocity-Verlet algorithm. This method updates the positions and velocities in

the following way:

$$\mathbf{r}_i(t+\delta t) = \mathbf{r}_i(t) + \delta t \mathbf{v}_i(t) + \frac{1}{2}\delta t^2 \mathbf{a}_i(t), \tag{3.18}$$

$$\mathbf{v}_i(t+\delta t) = \mathbf{v}_i(t) + \frac{1}{2}\delta t \left(\mathbf{a}_i(t) + \mathbf{a}_i(t+\delta t)\right). \tag{3.19}$$

The velocity-Verlet scheme proceeds in the following way: the new positions at time $t+\delta t$ are evaluated using eqn. 3.18; at the new positions, the forces and accelerations are updated; finally the velocity is calculated using eqn. 3.19. In this way, the calculations are performed using the minimal amount of data storage or computer memory. The velocity-Verlet algorithm is implemented in our simulation code because of its speed, its simplicity and its accuracy. It is also symplectic and thus conserves the Hamiltonian invariants better than any other algorithm.

3.3.2 Variable time step

Modelling the dynamical process of damage production due to atomic collisions and bombarding particles, usually involves high energies and velocities transferred from one particle to another. The energetic atoms can travel relatively long distances within a short time and, failure to control the time step, δt, can result in atoms moving into other atoms and eventually causing the total energy of the system to drift. In our model, a time step controller is employed which is of the form

$$\delta t = \frac{\alpha}{\sqrt{(\alpha + \beta * \gamma)}} \text{ fs.} \tag{3.20}$$

The time step depends on the parameter γ which is given by

$$\gamma = E_{KE}^{max} + |E_{PE}^{max}|, \tag{3.21}$$

where E_{KE}^{max} and E_{PE}^{max} is the maximum kinetic energy and potential energy over all the atoms in the system respectively. The time step resulting from eqn. 3.20 is smallest

at the beginning of atomic collisions involving keV energies but gradually increases as the energy is dissipated in the system. Typical values for α and β are 1.5 and 0.1 respectively. This limits the time step to 1.5 fs.

3.3.3 Monitored parameters

In an MD programme, it is essential to monitor the parameters that describe the system as a whole or as an ensemble as time progresses. The total energy, the pressure and the temperature, form the set of parameters which can be computed as a function of atomic coordinates and velocities. Based on the pair potential described by eqn. 3.13, the total potential energy due to all the pair interactions is given by:

$$V(t) = \sum_{i}^{N} \sum_{j>i}^{N} V_{ij}(\mathbf{r}_i, \mathbf{r}_j). \tag{3.22}$$

The system's total kinetic energy is the sum of contributions from individual particle momenta:

$$K(t) = \frac{1}{2} \sum_{i}^{N} m_i v_i^2, \tag{3.23}$$

where v_i denote the magnitude of the velocity vectors and m_i the masses of the particles, such that the total energy, $E = K + V$. Most of the dynamical simulations performed in this work were initiated within the so-called microcanonical or constant-NVE ensemble, where the number of atoms N, the volume of the simulation cell V, and the total energy of the system E, are all constant throughout the simulation.

The total kinetic energy in the system is related to the instantaneous temperature, T by:

$$\frac{1}{2} \sum_{i}^{N} m_i v_i^2 = \frac{3}{2} N k_B T, \tag{3.24}$$

where $k_B = 1.38065 \times 10^{-23}$ m^2 kg s^{-2} K^{-1} is the Boltzmann's constant. If required, the system's temperature can be altered by scaling the velocities using a temperature

control algorithm. In a microcanonical ensemble, the system's total energy should remain constant throughout a simulation. Energy conservation usually indicates that the simulation is running correctly while energy drifts can be the result of several factors, one of which is the use of an integration time step which is too large.

3.4 System equilibration

3.4.1 Minimisation by damping

The atomic coordinates describing the crystal structure and their corresponding velocities are required as input at the beginning of a dynamics simulation. However, the lattice structure is usually setup without any energy constraints by an external programme, and may not be in its minimal energy configuration. A quenching method has to be used to refine the structure so as to minimise its potential energy. This is done by adjusting the atomic positions and simultaneously removing the kinetic energy, until the net force on the atoms is zero. For the simulations presented in this thesis, damped MD was used for that purpose. The positions and velocities of the damped atoms are rescaled at each time step as follows:

$$\mathbf{r}_i = \mathbf{r}_i - \alpha \mathbf{v}_i, \tag{3.25}$$

$$\mathbf{v}_i = \beta \mathbf{v}_i. \tag{3.26}$$

The variables α and β are determined by the Lindhard-Scharff and Schiøtt inelastic energy loss model [49]. The physical interpretation of this process is that the kinetic energy of the moving atoms is continuously converted into electronic excitation as the atoms are gradually brought to equilibrium over a certain period of time. However, we often just use the model to find the local potential energy minimum by damping a system until the kinetic energy becomes vanishingly small.

3.4.2 Temperature control

Under the minimisation scheme discussed in the previous subsection, the system is brought to rest where all N atoms are frozen at their respective sites. At this stage, the mimimised structure is at a temperature of 0 K, and can directly be utilised for the production runs. However, in some of our simulations, the system was pre-heated to a certain temperature, T_0. A system with non-zero temperature is characterised by a distribution of atomic motion that reflects the temperature of the system. Here, the initial atomic velocities are drawn from a Maxwell-Boltzmann distribution, and are rescaled after each time step to regulate the system's temperature. This process models the effect of having the system coupled to an external heat bath that is at the desired temperature, T_0. The bath acts as a source of thermal energy, supplying or removing heat from the system as appropriate. Two temperature control algorithms were employed in this work and are discussed next.

Berendsen thermostat

The method of temperature control proposed by Berendsen *et al.* [50] relies on the scaling of the velocity vectors at every time step with a factor λ

$$\lambda = \left[1 + \frac{\delta t}{\tau_T}\left(\frac{T_0}{T} - 1\right)\right]^{\frac{1}{2}}, \tag{3.27}$$

in which T and T_0 are the actual and desired temperatures, δt is the time step of the integration algorithm and τ_T is a coupling parameter between the heat bath and the system. The system is brought towards the desired temperature at a rate determined by τ_T. Typically, a value of 1 ps was chosen for our simulations.

Nosé-Hoover thermostat

The Nosé-Hoover method [51] uses a modified equation of motion:

$$m_i \frac{d^2\mathbf{r}_i}{dt^2} = \mathbf{F} - \zeta \frac{d\mathbf{r}_i}{dt}, \tag{3.28}$$

which incorporates the thermal reservoir as being an integral part of the system. The rate of change of the coefficient ζ is given by

$$\frac{d\zeta}{dt} = \frac{1}{Q}\left(\sum_i^N v_i^2 - 3Nk_BT_0\right), \tag{3.29}$$

where Q describes the strength of the coupling between the system and the heat bath. The algorithm works as follows. If the instantaneous kinetic energy, represented by the term $\sum_i^N v_i^2$ in eqn. 3.29, is larger than the value $3Nk_BT_0$, then $\zeta > 0$. Accordingly, the resultant force on the right hand side of eqn. 3.28 decreases, and the velocity of the particles decreases. This continues until the kinetic energy becomes smaller than $3Nk_BT_0$. In the latter case, the reverse process occurs and the velocity of the particles increases. This mechanism allows the instantaneous temperature to oscillate around the desired temperature [52]. Although this method is canonical, it can introduce large temperature fluctuations.

3.5 Algorithms for force updates

The most computationally expensive task of a MD programme is the force evaluation. In the context of ionic materials, as mentioned previously, the interactions are divided into a short-range potential with a finite cut-off radius, and the long range Coulomb potential. Complex algorithms are required in order to treat long-range Coulomb forces efficiently whereas the short-range interactions can be truncated and, the potential can be evaluated using simple algorithms to enhance the speed of the

calculations.

3.5.1 Neighbour lists for short range interactions

The advantage of using a spherical cut-off radius, r_0, around each atom is because, for pair separations exceeding r_0, the magnitude of the short-range interactions become negligible, and can therefore be skipped in the calculations. However for each atom i, the code has to identify the list of atoms lying within the interaction range of atom i by examining the distances between atom i and all the remaining N-1 atoms. This involves calculating $\frac{1}{2}$N(N-1) distinct pair separations every single time step during the simulation. We employ the algorithm proposed by Verlet [47] to maintain a list of neighbours within the interaction range of each atom. In this method, the $\frac{1}{2}$N(N-1) distances are computed every nth time step and a list of neighbours within a distance r_l of every atom, is setup. The value of r_l is greater than r_0, such that there is a 'skin' of thickness $r_l - r_0$ around each atom as shown in fig. 3.6. For the next $n-1$ steps, the short-range forces are computed within this list of neighbours. The magnitude of r_l, should be such that in between the neighbour list updates, no particle should be allowed to traverse the 'skin' around the cut-off, and come within the interaction range of the potential. For the simulations presented in this work, the skin has a value of 0.3 Å. The frequency of the neighbour list updates depends on the maximum displacement recorded at each time step.

The cell index method [34] is used to increase the speed of the neighbour list updates described above. Here, the simulation cell with sides of length L_x, L_y and L_z is partitioned into smaller cubic subcells of length r_l. The creation of these subcells allows the neighbour search for each atom, to be performed in the subcell containing the atom, and, in the 26 neighbouring subcells around it. The computational time for the cell index method scales as $O(N)$ for N atoms.

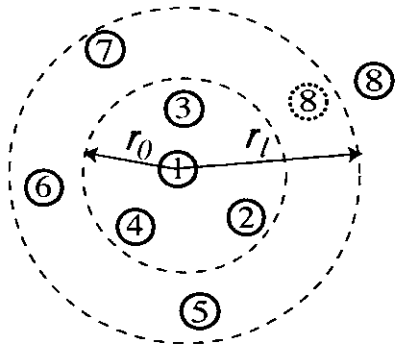

Figure 3.6: Illustration of the neighbours of atom 1. r_0 is the cut-off radius, with a skin of thickness $r_l - r_0$. Atoms 2, 3, 4, 5, 6 and 7 are on the list of atom 1, but not 8. During the next update, atom 8 (dotted) will appear on the list of atom 1.

3.5.2 Methods for Coulomb forces

The problem with charge-charge interactions arises from the term r_{ij}^{-1} in the potential energy function (eqn. 3.6). Because of its long range, the implementation of a cut-off radius for this type of potential is not possible. The direct method for computing the Coulomb interactions for a system of N ions is time consuming and requires $O(N^2)$ operations. A variety of algorithms have been developed to handle long range forces. The Ewald summation technique [34] is commonly used to evaluate the Coulomb forces in systems with periodic boundaries. This method scales as $O(N^{3/2})$ and is thus prohibitive for simulating very large systems. An alternative to the Ewald summation method is the Fast Multipole Method (FMM) which scales as $O(N)$. Two variants of the multipole method have been implemented in our parallel code for studying collision cascades, namely the Distributed Parallel Multipole Tree Algorithm (DPMTA) [53] and the Fast Multipole Method for Parallel computers (FMMP) [54]. A brief description of the Ewald method and the FMM are provided in the following subsections. The Ewald summation technique is in-built in the temperature accelerated dynamics software used in this work for investigating point defect diffusion (Chapter 6).

Ewald summation

The Ewald summation technique evaluates the Coulomb interactions for a charge-neutral system of ions and its periodic replicas. Let us assume that our system is a cubic cell of length L and containing N ions. The electrostatic energy becomes the sum of contributions between pairs of charges in the central cell plus all contributions from the periodic images around it, and is given by

$$V = \frac{1}{2}\sum_{\mathbf{n}}{}' \left(\sum_{i}^{N}\sum_{j}^{N} \frac{z_i z_j e^2}{4\pi\epsilon_0 |\mathbf{r}_{ij} + \mathbf{n}|} \right). \tag{3.30}$$

The outer sum in eqn. 3.30, is taken over all periodic images, $\mathbf{n} = (n_x L, n_y L, n_z L)$ with n_x, n_y, n_z being integers, and the prime indicates omission of $i = j$ for $\mathbf{n} = 0$. Eqn. 3.30 is a poorly converging series and is difficult to evaluate. The basic principle of the Ewald method is to rewrite the summation into two series, each of which converges more rapidly. This is done by setting up a Gaussian charge distribution of opposite charge around each ion which neutralises the ion. The electrostatic potential due to particle i results only from the fraction of its charge that is not screened. This results in a rapidly converging series in real space which can be easily computed by direct summation.

The system's charge neutrality is restored by placing another Gaussian charge distribution on each ion, which has the same sign as the ion. These additional distributions are summed in reciprocal space, the result of which converges more rapidly than the original point-charge sum.

Two more terms are required in the final result. The first involves subtracting a so called self-interaction term of each Gaussian function with itself within the real space calculations. The second term is dependent on the medium surrounding the system and its periodic images. More details of this method can be found elsewhere [1, 34, 46].

The Fast Multipole Method

The Fast Multipole Method forms part of the tree-code family and provides a different approach to modelling electrostatic interactions in a N-body system. The FMM algorithm divides the simulation cell into sub-regions containing small groups of charges, and uses multipole expansions to evaluate the interactions between groups that are sufficiently far from each other. The interactions between nearby charges are computed directly. The different steps involved during the calculations are summarised below.

1. *Cell subdivision*

   The simulation box with dimensions (L_x, L_y, L_z) is divided into smaller cells according to a user-defined parameter n (see fig. 3.7). For $n = 0$, there is no such subdivision. For $n = 1$, the simulation box is divided once along the x-, y- and z- axes resulting in 8 subcells with dimensions $(L_x/2, L_y/2, L_z/2)$. At level l, the subcell dimensions are $(L_x/2^l, L_y/2^l, L_z/2^l)$.

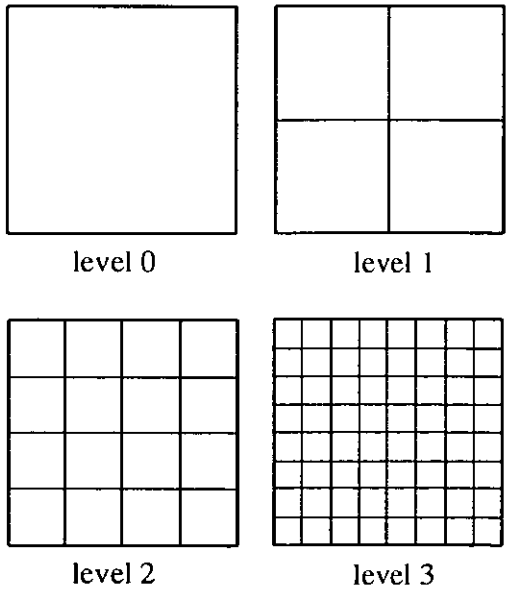

Figure 3.7: Cell subdivision in the fast multipole method in two-dimensions. Here, the number of recursive subdivisions is 3. Level 0 denotes the simulation box.

2. *Multipole expansion*

   At the finest level n of subdivision, the multipole expansions about the center of each subcell is computed. For each cell A, this expansion represents the potential field due to all other particles found in sufficiently distant subcells in the interaction list of A, as shown in fig. 3.8. In this representation, the potential field at a point $\mathbf{P} = (r, \theta, \phi)$ due to a group of k charges located at $\mathbf{r}_i = (\rho_i, \alpha_i, \beta_i)$ with charges $\{q_i, i = 1, ..., k\}$, sufficiently far away from $\mathbf{P}$ $(\rho_i < r, \forall i)$ can be expressed as the multipole expansion

$$\phi(\mathbf{P}) = \sum_{n=0}^{\infty} \sum_{m=-n}^{n} \frac{M_n^m}{r^{n+1}} Y_n^m(\theta, \phi), \tag{3.31}$$

$$M_n^m = \sum_{i=1}^{k} q_i \rho_i^n Y_n^{-m}(\alpha_i, \beta_i), \tag{3.32}$$

   where Y_n^{-m} are the associated Legendre polynomials [55].

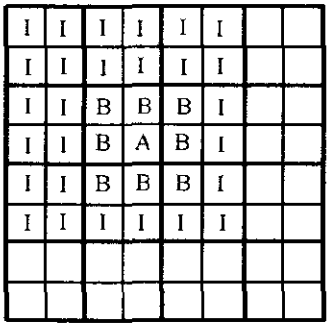

Figure 3.8: A 2-D representation of the interaction list of cell A at level $n = 3$. The squares separated by thin lines represent level n subdivisions, their parents at level $n-1$ are separated by thick lines. Subcell A interacts with *sufficiently distant* subcells labelled I. These are not near neighbours of A but are contained within the nearest neighbours of the parent cell of A.

3. *Upward pass*

   The multipole expansions of the smallest cells at level n, are then grouped about a common origin at the next $n-1$ level. This is done by translating the

multipole expansions of the smallest cells upwards to the centre of the parent cell. In this way, the multipole moments at each level of subdivision are obtained and represent the effect of larger and larger groups of particles.

4. *Downward pass*

   The next stage is to fuse together several multipole expansions at a each level into a single local expansion. This represents the potential field due to all particles in the system that are not contained in the current box or its nearest neighbours. This expansion is then shifted to the centre of the box's children, until the local expansions for the cells at the finest level of subdivision are obtained.

5. *Force calculation*

   The potential energy and force on each particle can be evaluated using the local expansion in the smallest cells. Finally, the contributions of the particles in each cell and in the neighbouring cells are computed directly and added together.

The complete algorithm and the set of theorems and equations involved at each step of the FMM are given in the original work of Greengard and Rokhlin which has been reprinted in [56]. The accuracy and speed of the calculations depend on the number of terms present in the multipole expansion (MPE) and on the number of recursive subdivisions (RSD) of the simulation cell.

3.6 Parallel routines

Historically, early MD simulations were performed on the first generation of computers and were limited to a few hundreds of atoms only. With the advent of supercomputers and parallel computing technology, it is now possible to perform large-scale simulations involving millions of atoms within a reasonable amount of time. Parallel computing uses a certain decomposition strategy to distribute the data among the

total number of processors available, with the lowest possible communication cost. The three main parallelisation strategies are atom decomposition, force decomposition and spatial decomposition [57]. The simulations in this work were performed using the parallel LBOMD code, developed at Loughborough University. The code employs the spatial decomposition technique for decomposing the simulation box onto different compute nodes, and uses Message Passing Interface (MPI) [58] for processor communications. The ionic potential was implemented into the code, together with the two parallel multipole methods (DPMTA and FMMP) for evaluating long range electrostatic contributions. The spatial decomposition strategy and the integration of the multipole methods into the LBOMD code are discussed in the next subsections.

3.6.1 Spatial decomposition

The essence of the spatial decomposition technique is to divide the simulation domain into smaller boxes, and to assign each spatial region to a distinct processor. Atoms moving outside the processor-domain are allowed onto the neighbouring processor. Each processor has the complete set of data for each atom in the box and only requires the neighbouring atoms' information in adjacent boxes in order to evaluate the short-range forces at each time step.

In order to communicate the relevant list of neighbours from processor to processor, a list of atoms which lie within the distance Max(r_0) (maximum cut-off radius) from the boundaries of each processor is setup. This list contains the atoms required by neighbouring processors along the relevant directions in order to compute the short-range forces and is represented by the green segments in fig. 3.9. Once the proper number of neighbours is allocated for exchange, the communication is performed firstly in the east/west direction for all processors. A simultaneous send and receive operation is executed: each processor sends data westwardly to the adjacent processor, while receiving incoming data on the other side. In fig 3.9 (a), processor 13 sends data to 12, while receiving data from 14. This process is then repeated in the

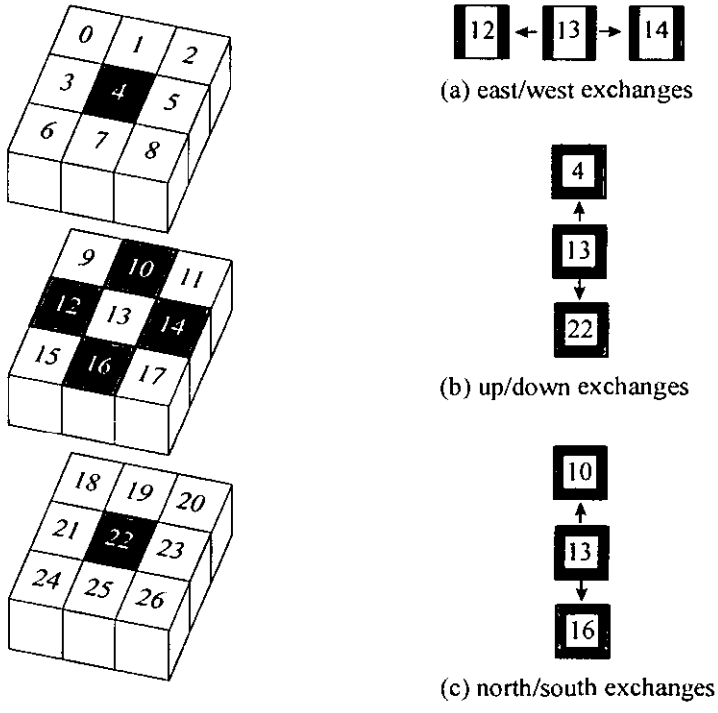

Figure 3.9: Diagram on the left represents the simulation box subdivided into 27 smaller boxes for spatial decomposition on 27 processors. Processor 13 only communicates with processors 12, 14, 4, 22, 10 and 16 shown in red. Data exchange for processor 13 in the (a) east/west direction with 12 and 14; (b) up/down direction with 4 and 22; (c) north/south direction with 10 and 16. The green segments represent exchanged data.

opposite direction to complete the data exchange along that direction. The operation is repeated in the up/down direction (fig. 3.9 (b)), but the exchange list on each processor includes those atoms received at the previous step, and are communicated to neighbouring processors as required during this pass. Finally, the same procedure is done in the north/south direction to complete the processor to processor communication. The advantage of this method is that any processor only communicates with 6 other processors, while getting information from all 26 surrounding boxes.

3.6.2 DPMTA and FMMP

Both the DPMTA [53] and FMMP [54] methods are hybrids of the Fast Multipole Method discussed in section 3.5.2, and are used for the fast evaluation of Coulomb interactions. Parallel versions of both multipole methods have been implemented into the main LBOMD code. There are three major differences between the two multipole methods. Firstly, the DPMTA software is a library of C codes, whereas the FMMP is coded in Fortran77. Secondly, the process of direct force calculations in the fast multipole algorithm (step 5 in section 3.5.2) is performed by an in-built function in the DPMTA library whereas, in the FMMP method, this computation is performed efficiently by an external subroutine that uses the subcells created by the cell index method in the MD code. Lastly, and most importantly, the DPMTA and FMMP methods have their own differences in the way they have been developed by their respective authors. The main features involved during the implementation of the DPMTA and FMMP into the MD code are discussed below.

The DPMTA library is written with the flexibility to fit into the framework of an existing parallel code. Under the spatial decomposition strategy, each processor provides the list of particle data to the DPMTA engine. DPMTA processes all the incoming data, redistributes it where necessary during the computation, and returns the associated force and potential energy values due to the Coulomb interactions, back to the processors. In order to link the DPMTA code (C programme that uses

MPI for message passing) to the Fortran90 LBOMD code, a Fortran interface is used. This interface remaps the data structures of the atoms in the MD code to the corresponding data structures in the DPMTA code and vice-versa.

The main task in the implementation of the FMMP was to convert the Fortran77 commands into Fortran90 and to add a separate subroutine for direct sums. The most efficient way to do the direct computation is to use the subcells created by cell index method in the MD code. Each cell at the finest level of subdivision of the FMMP locates its nearest neighbour cells within the cell index structure in order to perform the direct Coulomb sums. A 2-D schematic representation of this procedure is shown in fig. 3.10.

The FMMP is a more recent version of the multipole method than DPMTA and was an attractive method to implement because of its supposed high efficiency in simulating up to 512 million charged particles [54]. After integrating both multipole methods into our code, their respective speeds for doing the same amount of computation was investigated. Tests were carried out for system sizes ranging from 12331 atoms to 988391 atoms, on a 200 processor cluster at Loughborough University's High Performance Computing and Visualisation Centre. The results in tables 3.4 and 3.5 show the time taken for two force evaluations on a certain number of processors and the corresponding speedup values. The speedup factor is defined as

$$S_P = \frac{\text{Execution time using one processor}}{\text{Execution time using } P \text{ processors}}. \tag{3.33}$$

For the bigger systems, the memory per processor was insufficient to allow runs on a small number of processors. In those cases the speedup factor were estimated using the speedup factors obtained from the smaller systems. The figures in tables 3.4 and 3.5 show that DPMTA is faster than FMMP. One possible reason for this difference in speed is that the implementation of the fast multipole algorithm is done differently in both the FMMP and the DPMTA where in the latter method the direct

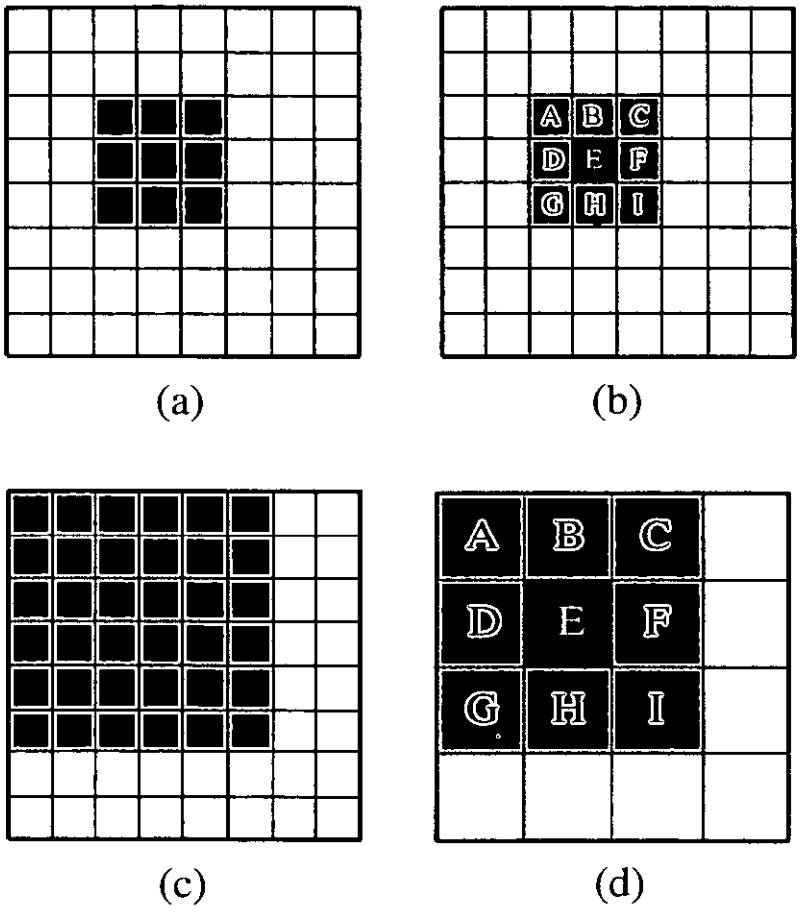

Figure 3.10: Coulomb interactions are computed directly for atoms in cells at the finest level of FMMP, and in their nearest neighbour cells. Figures (a) and (c) represent subdivisions for the cell index method determined by the MD code. Figures (b) and (d) denote FMMP subdivision levels of 3 and 2 respectively. Depending on the size of the FMMP boxes at the finest level, the correct number of cell boxes (shaded region) has to be included in the calculations.

computation is performed just after the *upward pass* procedure while this is done at the end in the FMMP. The inclusion of the direct sums at an early stage could be a more efficient way to do the calculations. However, the speedup factors of FMMP are much better than those of DPMTA. Although both multipole methods were designed to run with and without periodic boundary conditions (pbc), our simulations were unstable when using pbc. The collision cascade simulations were therefore performed using DPMTA and without pbc.

As stated previously, the accuracy and speed of the fast multipole method is dependent on the number of terms present in the multipole expansion (MPE) and on the number of recursive subdivisions (RSD) employed to decompose the simulation cell. It was found that the maximum error of the DPMTA method compared to direct calculations for a system containing 10000 uniformly distributed charges was 0.01 when the MPE level was set to 4. As the MPE level was increased by steps of 2, the maximum error was reduced by one order of magnitude [59]. The variation in the speed and accuracy of the DPMTA calculations for systems containing 2000 to 130000 charged particles has also been studied by Ramasawmy [60]. Typical values of the MPE range between 4 to 8 with the higher values being more accurate than the lower but the calculations take longer. As the system size gets bigger, higher values of RSD are required to speed up the calculations. The MPE and RSD parameters used in this thesis are given in table 3.6.

3.7 Visualisation method

During the evolution of any system by MD, output files of the system's configuration can be generated at regular time intervals. These files usually contain the following information about the atoms: the atomic species, their spatial coordinates and individual energies. This data can be processed by a visualiser in order to create picture frames, which can then be transformed into a movie in order to look at the dynamics

Table 3.4: Execution time in seconds involving two force updates using DPMTA. N is the number of atoms in the system. The speedup factor within brackets is an estimate.

N		Processors					
		1	2	4	8	16	32
12331	Time	7.79	3.97	3.27	2.24	2.36	2.70
	Speedup	1.0	1.96	2.38	3.47	3.30	2.89
97669	Time	50.99	33.13	19.29	12.77	9.29	7.63
	Speedup	1.0	1.54	2.64	3.99	5.49	6.68
154883	Time		55.01	34.76	22.02	18.56	12.01
	Speedup		(1.97)	3.12	4.92	5.84	9.02
988391	Time					88.10	60.87

Table 3.5: Execution time in seconds involving two force updates using FMMP.

N		Processors					
		1	2	4	8	16	32
12331	Time	383.36	193.11	97.93	49.94	28.36	16.39
	Speedup	1.0	1.99	3.91	7.68	13.52	23.39
97669	Time	1471.68	730.34	369.97	190.09	103.07	55.33
	Speedup	1.0	2.02	3.98	7.74	14.28	26.60
154883	Time		751.16	381.16	195.70	108.91	58.25
	Speedup		(1.98)	3.90	7.60	13.66	25.53
988391	Time					923.78	478.39

Table 3.6: DPMTA parameters used in this work. N is the number of particles in the cubic simulation cell of dimension L. MPE is the multipole expansion parameter while RSD is the number of recursive subdivisions.

N	L (Å)	MPE	RSD
7166	41.6	6	4
12331	49.7	6	5
97669	98.5	6	5
154883	114.7	6	5
450461	163.5	6	6
988391	212.2	6	6
3081611	309.7	6	7

of the system being investigated. For the simulations presented in this work, a VTK (Visualization ToolKit) [61] based software called LBOVIS, is used for that purpose. The basic principle of LBOVIS is to store the initial configuration of the system at time $t = 0$ and to compare that with configurations at subsequent time steps in order to produce the required image. LBOVIS can also be used for real time visualisation with the LBOMD code. The different functionalities of LBOVIS can be identified in fig 3.11. For the simulations presented in this work, the atoms were mostly filtered according to the 'point defects' option, in order to investigate the evolution of interstitials, vacancies and antisite defects.

3.8 Conclusions

In this chapter, the main parts of the molecular dynamics method have been discussed. These include the potential energy function, the integration algorithm, the miminisation and temperature-control procedures and the multipole methods. MD was employed to investigate the dynamical process of defect production at the atomistic scale in MgB_2O_4 crystals where B = Al, Ga or In. The results are presented in chapters 4 and 5. The method was also applied in a MgO/Al_2O_3 system to look at the impact of low energy cascades at the interfacial region (chapter 7).

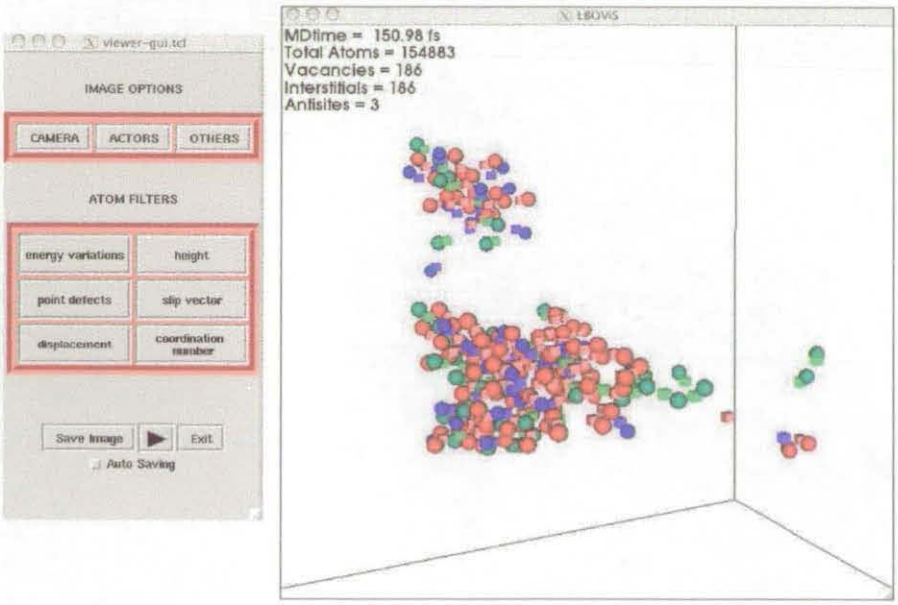

Figure 3.11: The LBOVIS visualisation tool. Different options for imaging are available - atoms can be viewed according to their energy, displacement, height, etc. The images can be zoomed-in and out, and rotated as desired in order to focus on any specific region of interest.

Chapter 4

MD simulations of radiation damage in normal $MgAl_2O_4$ spinel

4.1 Introduction

The crystalline structure of any material is disrupted and destabilised under irradiation by highly energetic particles which penetrate the target material by losing their energy through elastic collisions with other atoms and through electronic excitation at higher energies. The production of lattice defects is mainly due to the elastic collisions whereas excitation of electrons can result in the ionisation of some of the atoms. The spatial distribution and evolution of the defects within the structure directly affect the stability of the material. It is known that point defect accumulation resulting from exposure to radiation can cause adverse effects such as swelling or radiation-induced amorphisation within certain crystal structures [62]. However, harmless interstitial-vacancy recombination mechanisms are very likely in materials with good radiation tolerance. The final damaged state of any material subject to particle bombardment is the result of point defect production (femtoseconds), the nearly instantaneous stage of structure relaxation following the energetic events (picoseconds), and on the long time thermal annealing process (seconds or longer).

In this chapter, MD simulations are performed in normal $MgAl_2O_4$ spinel to determine its microstructural evolution under the impact of an energetic particle. Here, we investigate the first stages of defect production and annihilation occurring on the time scales of several picoseconds. The initial energetic bombardment is modelled by providing excess kinetic energy to one atom in the material, known as the primary knock-on atom or PKA, along a certain crystallographic direction. The ballistic collisions between the PKA and other lattice atoms create atomic displacements over the time scale of picoseconds and produce defects which then diffuse more slowly. The sequence of atomic collisions leads to the formation of a collision cascade in the structure, which is assumed to be purely elastic with no effect on the electronic structure of the atoms. The nature and morphology of surviving defects remaining in the system after the energy has dissipated characterise the radiation damage (on the ps time scale). The evolution of these defect structures over longer time scales will be investigated in chapter 6.

The very early stage of point defect formation in magnesium aluminate spinel is investigated by finding the threshold displacement energies. The results are presented in the first part of the chapter. The various types of defect structures encountered at this stage are thoroughly analysed. For the most common types, the defect formation energies are computed using damped MD. In the last section, collision cascades in the energy regime of 0.4-10 keV are investigated.

4.2 Threshold displacement energies

An important physical parameter for assessing radiation damage in a material is the threshold displacement energy, E_d [63]. E_d is generally defined as the minimum amount of transferred kinetic energy to an atom in the crystal that produces a stable Frenkel pair, which is, an interstitial and a vacancy of the same atom type. For the spinel simulations we assume that the threshold energy is reached either when at least

a Frenkel pair appears in the lattice, or, when at least two atoms of different species exchange sites forming a pair of antisites, or, when at least two atoms of the same species exchange sites and no other defects remain in the lattice. The latter event is referred to as a replacement mechanism. A similar approach was used to find the threshold displacement energies in zircon, $ZrSiO_4$ [64]. With this concept in mind, we define the meaning of an interstitial defect and a vacancy defect.

A displaced atom is referred to as an interstitial if it is further from a normal lattice site by $(\sqrt{3}/16)a_0$ Å, where a_0 denotes the lattice parameter of the spinel. This distance is half the separation between a tetrahedral cation and a nearest structural octahedral vacancy as shown in fig. 4.1. The atom is still counted as an interstitial if it occupies a structural vacancy which is not a normal lattice site. Vacancies are similarly defined as original lattice sites with no atom within a radius of $(\sqrt{3}/16)a_0$ Å. An antisite defect in the normal spinel refers to a Mg ion sitting on an Al site or vice-versa. An mentioned in chapter 2, the Kröger-Vink notation is employed to describe the various defect structures encountered.

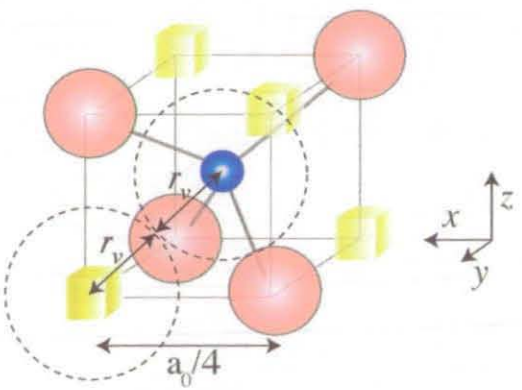

Figure 4.1: The distance criterion in defining an interstitial defect or a vacancy defect is given by the spherical region of radius $r_v = (\sqrt{3}/16)a_0$ Å around a lattice site.

4.2.1 Methodology

The simulations were carried out by choosing an atom (the PKA) close to the centre of the lattice to which excess kinetic energy was imparted along a certain crystallographic direction. For each direction, the threshold energy was determined by gradually increasing the kinetic energy in steps of 5 eV until permanently displaced atoms appear in the structure. E_d was taken to be the average of the two values: the highest kinetic energy that did not create any permanent displacements and the smallest one that did. The error in the resulting value of E_d is therefore $\pm$ 2.5 eV but is not so accurately predicted in different thermal conditions. The $MgAl_2O_4$ lattice was setup using the coordinate system described in table 2.1. The atoms were first relaxed using damped MD, then heated to a certain temperature using the Berendsen method before the simulations were carried out. During the production runs, the system evolved with no heat bath. To determine E_d, the heating temperature was chosen so that after the excess kinetic energy imparted by the PKA was dissipated, the final temperature of the lattice was either 125 K or 300 K. The trajectories used to determine E_d were terminated after 2.5 ps. The system was made up of 5 spinel unit cells containing a total of 7166 atoms within a cubic box of dimensions 41.6 Å. The simulations were performed without periodic boundaries whereby each cascade core was embedded at the centre of the simulation box, far from the fixed boundaries. E_d was determined for each atom species (Mg, Al and O) because of their distinct atomic masses, coordination and bonding in spinel. The DPMTA method was employed to evaluate Coulomb forces.

4.2.2 Results

A range of directions was chosen for the initial knock-on event. For each PKA specie, head on trajectories were chosen for which high E_d values were obtained. However, in order to find out the lower threshold energy values, a few channelling trajectories

Table 4.1: Table of calculated threshold displacement energies in eV in magnesium aluminate spinel at temperatures of 125 K and 300 K. The bold characters indicate the maximum and minimum E_d values. The 300 K simulations were performed three times; the E_d values shown represent the mean ± the standard deviation (std. dev.).

PKA	125 K			300 K (mean ± std. dev.)		
direction	Mg PKA	Al PKA	O PKA	Mg PKA	Al PKA	O PKA
[2 3 2]	182.5	82.5	47.5	**184.2** ± 5.8	79.2 ± 10.4	49.2 ± 2.9
[1 1 1]	167.5	77.5	47.5	172.5 ± 10.0	74.2 ± 2.9	49.2 ± 2.9
[2 1 1]	122.5	77.5	62.5	132.5 ± 25.0	82.5 ± 5.0	64.2 ± 11.5
[1 0 0]	92.5	72.5	**27.5**	94.2 ± 2.9	82.5 ± 36.1	**27.5** ± 0.0
[1 4 1]	232.5	82.5	52.5	142.5 ± 15.0	79.5 ± 10.4	54.2 ± 2.9
[3 1 8]	192.5	87.5	67.5	94.2 ± 10.4	87.5 ± 5.0	72.5 ± 8.7
[8 3 6]	72.5	82.5	57.5	80.8 ± 14.4	82.5 ± 5.0	60.8 ± 10.4
[0 5 3]	**37.5**	**157.5**	77.5	**34.2** ± 2.9	**147.5** ± 31.2	70.8 ± 5.8
[7 1 2]	117.5	**57.5**	72.5	122.5 ± 10.0	**55.8** ± 7.6	67.5 ± 31.2
[7 9 3]	67.5	87.5	57.5	62.5 ± 10.0	90.8 ± 7.6	60.8 ± 5.8
[1 1 0]	42.5	117.5	**112.5**	42.5 ± 5.0	112.5 ± 10.0	**105.8** ± 22.5
[1 5 1]	232.5	82.5	52.5	145.8 ± 5.8	79.2 ± 10.4	54.2 ± 2.9
[1 3 1]	**277.5**	82.5	47.5	159.2 ± 23.6	82.5 ± 5.0	54.2 ± 2.9
Mean	141.4	88.3	60.2 (59[a])	112.9	87.4	60.8
Std. dev.	78.6	24.6	20.3	48.8	21.8	17.9

[a] Ref. [65]: experimental value of the threshold displacement energy of oxygen at the temperature of 77 K.

were included. For each PKA direction shown in table 4.1, E_d was determined from a single set for the simulations performed at the temperature of 125 K. However, the 300 K simulations were performed three times for the same direction but with varying equilibration times before the energetic event because of fluctuations in the displacements of the initial atom positions due to the thermal motion. It was found that E_d could vary depending on the precise initial conditions. The resulting value of the threshold energy at 300 K was therefore taken to be the average of those three values.

For a typical cascade, the maximum damage occurred around 60–90 fs after the initial knock-on event with a maximum of $\approx$ 20 displaced atoms. For low threshold energies, only a few atoms are involved in the cascade. After the ballistic phase of the cascade, the lattice gradually recovers its cohesion with the annihilation of most of the defects, and if the energy imparted to the PKA is large enough, a few permanently displaced atoms are obtained, some of which may remain in the crystal structure as defects. Such a situation is illustrated in fig. 4.2 showing snapshots of a 115 eV Al PKA cascade at 300 K. The PKA direction was set along [0 5 3] resulting in a near head-on collision with another Al atom. The defects remaining at the end of the 2.5 ps cascade consist of a split $Mg_i^{\cdot\cdot}$–V''_{Mg}–$Al_i^{\cdot\cdot\cdot}$ interstitial where one Al and one Mg interstitials share the same Mg vacancy, and an V'''_{Al}–$Al_i^{\cdot\cdot\cdot}$–V'''_{Al} split vacancy configuration where one Al interstitial is trapped between two Al vacancies. The defect evolution and temperature variation during the cascade is shown in fig. 4.3.

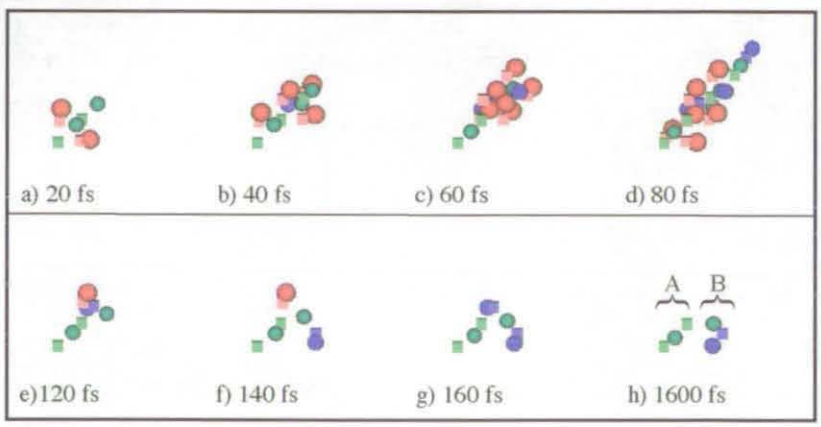

Figure 4.2: Cascade snapshots for an Al PKA along [0 5 3] at the energy of 115 eV (300 K). Only defects are shown. Spheres represent interstitials and cubes denote vacancies. The red colour refers to O^{2-} defects, blue is for Mg^{2+} defects while Al^{3+} defects are coloured green. The same colour scheme is employed throughout this thesis unless stated otherwise. (a)-(d) The PKA starts a small cascade. (e)-(h) The recrystallisation process results in an Al split vacancy defect labelled A, and a $Mg_i^{\cdot\cdot}$–V''_{Mg}–$Al_i^{\cdot\cdot\cdot}$ cation split interstitial denoted B. The defects are separated by 3.0 Å.

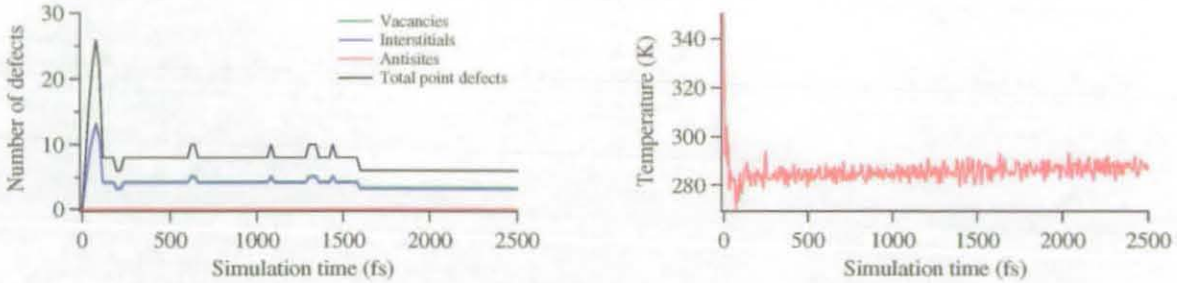

Figure 4.3: The defect evolution (left), and the temperature variation (right) as time progresses during the 115 eV cascade generated by an Al PKA along [0 5 3] at 300 K. The peak damage occurs at the time of 80 fs, while stable defects form at 1600 fs. The temperature remains close to 300 K.

The results in table 4.1 confirm that E_d is dependent on the PKA type, on the orientation of the PKA and on the temperature of the system. Along certain trajectories, where the PKA initially undergoes a direct (head-on) collision with a nearby atom, more energy is required to force the target atom away from its lattice position. In other cases, the PKA is able to move easily along other 'open' paths between its first neighbours, requiring a lower E_d. In general, the O PKA was found to have the lowest threshold energy, followed by Al and then Mg. In addition, there are some large differences in E_d dependent on the exact initial positions and velocities of the lattice ions for a fixed temperature. For example at 300 K, the value of E_d along the near head-on [1 0 0] trajectory for an Al PKA varied by 72 eV from the lowest value of 50 eV to the highest at 122.5 eV. Averaged over all trajectories and PKA ions, the standard deviation in the value of E_d at 300 K was 12 eV but this value is larger for the case of head-on collisions.

The defect distribution for the 13 simulations performed at 125 K is given in table 4.2 and for the 39 runs performed at 300 K, the defect distribution is given in table 4.3. Because interstitial defects occur as split interstitials rather than isolated interstitials, we count a split interstitial separated from an isolated vacancy as two Frenkel pairs. In order to gain a more physical insight into the numbers presented in tables 4.1, 4.2 and 4.3, we examine trajectories with the high and low values of E_d in

more detail for each of the Mg, Al and O PKAs.

Table 4.2: Mean and standard deviation of the number of defects generated per trajectory at threshold energies in magnesium aluminate for each PKA at 125 K (total of 13 simulations). 'Replacements' indicate swapping of ions of the same species. The column 'Split interstitials' is divided into Mg, O and Mg–Al which denote $Mg_i^{\cdot\cdot}$–V''_{Mg}–$Mg_i^{\cdot\cdot}$, O_i''–$V_O^{\cdot\cdot}$–O_i'' and $Mg_i^{\cdot\cdot}$–V''_{Mg}–$Al_i^{\cdot\cdot\cdot}$ defects respectively. N_{TFP} is the mean number of Frenkel pairs and 'Perfect lattice' indicates the percentage of trajectories at the end of which no defect was observed.

PKA	Replacement			Split interstitials			Antisites		N_{TFP}	Perfect
type	Mg_{Mg}	O_O	Al_{Al}	Mg	O	Mg–Al	$Al^{\cdot}_{Mg}$	Mg'_{Al}		lattice (%)
Mg	0.8 ± 0.9	0.0	0.2 ± 0.6	0.5 ± 0.5	0.0	0.1 ± 0.3	0.4 ± 0.5	0.3 ± 0.5	1.1 ± 1.0	31
Al	0.2 ± 0.6	0.0	1.1 ± 0.9	0.0	0.2 ± 0.4	0.2 ± 0.4	0.3 ± 0.5	0.3 ± 0.5	0.6 ± 1.0	38
O	0.0	1.0 ± 1.4	0.0	0.0	0.7 ± 0.5	0.0	0.0	0.0	1.4 ± 1.0	31

Table 4.3: Mean and standard deviation of the number of defects per PKA trajectory at threshold energies calculated at 300 K for a total of 39 simulations for each PKA.

PKA	Replacement			Split interstitials			Antisites		N_{TFP}	Perfect
type	Mg_{Mg}	O_O	Al_{Al}	Mg	O	Mg–Al	$Al^{\cdot}_{Mg}$	Mg'_{Al}		lattice (%)
Mg	0.7 ± 0.9	0.9 ± 1.6	0.0 ± 0.2	0.1 ± 0.3	0.1 ± 0.3	0.2 ± 0.4	0.3 ± 0.5	0.4 ± 0.5	0.7 ± 1.2	49
Al	0.1 ± 0.4	0.0 ± 0.2	1.0 ± 0.7	0.0 ± 0.2	0.1 ± 0.3	0.1 ± 0.3	0.5 ± 0.5	0.5 ± 0.5	0.6 ± 0.9	26
O	0.0	1.0 ± 1.3	0.0	0.0	0.6 ± 0.5	0.0	0.0	0.0	1.2 ± 1.0	38

Mg PKA

In the normal spinel structure, the Mg ions are surrounded by four nearest neighbour oxygen ions. Depending on its local environment, a Mg PKA can undergo direct collisions along four of the ⟨111⟩ directions with an oxygen ion. For instance, a Mg PKA residing at the fractional coordinates (1/2,1/2,0) in fig. 2.2 will be head-on to an oxygen ion along the directions $[\bar{1}\ 1\ 1]$, $[1\ \bar{1}\ 1]$, $[\bar{1}\ \bar{1}\ \bar{1}]$ and $[1\ 1\ \bar{1}]$, while a Mg PKA sitting at (2/3,2/3,1/4) will first collide with an oxygen along $[1\ 1\ 1]$, $[\bar{1}\ \bar{1}\ 1]$, $[1\ \bar{1}\ \bar{1}]$

and [$\bar{1}$ 1 $\bar{1}$]. The PKA chosen for the threshold energy simulations discussed next is located at the fractional coordinate (2/3,2/3,1/4).

Along the specific [1 1 1] path, a relatively high E_d value of 167.5 eV was recorded at the temperature of 125 K. For this energy, the PKA first collided with an O ion creating a maximum of 11 displaced atoms after 60 fs. All the defects recombined after 210 fs leaving a perfect lattice where only 2 Al atoms had exchanged sites (replacement mechanism). For the same direction, each of the three 300 K simulations were different: the first one resulted in 3 O ions swapping sites with no damage (E_d = 172.5 eV); the second simulation terminated with a pair of $Al_{Mg}^{\cdot}$ and Mg'_{Al} antisites (E_d = 182.5 eV); the third simulation was similar to the first (E_d = 162.5 eV). The average value of E_d at 300 K for a Mg PKA along [1 1 1] was therefore 172.5 eV.

Table 4.1 shows that the highest E_d recorded for the temperature of 125 K was along the [1 3 1] direction with a value of 277.5 eV. During this collision cascade, the Mg projectile underwent a head-on collision with an Al ion, creating a maximum of 18 displaced ions after 90 fs with the final state having no defects, but with only 2 Mg ions exchanging sites. The cascade development for this simulation is shown in fig. 4.4. The defects created at t = 240 fs consisting of a Mg split interstitial and a Mg vacancy, anneal completely just after 480 fs. As in most of the cascades, the 300 K simulations for the same direction resulted in different final configurations, with varying threshold energies of 177.5 eV, 132.5 eV and 167.5 eV. These values are much lower than the threshold energy of 277.5 eV obtained at 125 K.

The smallest value of E_d for the Mg PKA was averaged as 34.2 eV at 300 K along the [0 5 3] direction. Unlike the higher energy thresholds where a lot of atoms are displaced, along the [0 5 3] direction, the PKA could reach its nearest neighbour Mg atom without causing much movement of the first nearest oxygen neighbours. During this process, only 2 Mg atoms were displaced. The Mg PKA swapped site with the Mg atom leaving the crystal structure unchanged. An identical mechanism

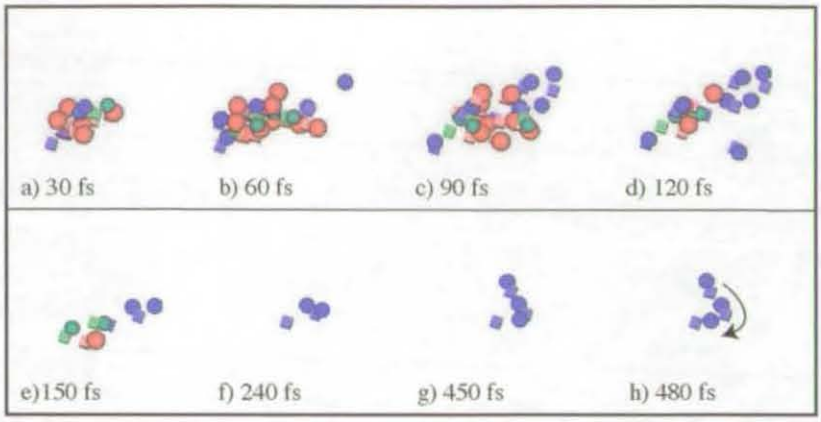

Figure 4.4: Cascade snapshots at the energy of 280 eV and temperature of 125 K for a Mg PKA along [1 3 1]. Peak damage occurs at 90 fs with 18 displaced atoms. No defect remains in the structure after 480 fs.

was observed at 125 K.

The numbers in table 4.2 for the Mg PKA show that 31 % of the trajectories (4 out of the 13 simulations) at 125 K resulted in a perfect lattice due to replacement mechanisms on the Mg and Al sublattices. The perfect lattice was recovered for threshold energy values of 37.5 eV along [0 5 3] (lowest E_d), 167.5 eV along [1 1 1], 277.5 eV along [1 3 1] (highest E_d) and 67.5 eV along [7 9 3]. The PKA did not create any damage or replacements on the oxygen sublattice at 125 K, but resulted in antisite defects and cation Frenkel pairs.

The 300 K simulations show a similar trend in the number of defects produced except that: a) fewer Frenkel pairs are produced at 300 K as compared to the 125 K simulations, b) a large number of replacement mechanisms occurred on the oxygen sublattice at 300 K while none occurred at 125 K, c) a few anion split interstitials were obtained at 300 K but none were seen at 125 K.

Al PKA

The aluminium ions have 6 oxygen nearest neighbours along the six ⟨100⟩ directions as illustrated in fig 2.3 (a). However along six ⟨110⟩ paths, the PKA would undergo head-on collisions with other Al ions.

The highest E_d was recorded along the [0 5 3] direction where the Al PKA path was almost head-on towards another Al ion. The 125 K cascade for an energy of 160 eV along that direction produced replacement sequences of one Al and two Mg ions over their respective sublattices. The system stabilised after 330 fs with the formation of one Al and one Mg antisites. The 300 K simulations for the same direction but with different equilibration times resulted in threshold energies of 112.5 eV (cascade development is shown in fig. 4.2), 172.5 eV and 157.5 eV. The second highest E_d was obtained along the [1 1 0] direction. Both the [0 5 3] and [1 1 0] directions represent initial Al to Al collision sequences for the PKA, hence the high E_d values.

The [1 0 0] directed Al PKA was head-on to an O ion and resulted in threshold energies of 72.5 eV and 82.5 eV at 125 K and 300 K respectively. During the lower temperature cascade, the Al PKA could transfer sufficient energy to move the target O ion. The latter was then displaced to an interstitial site, forming a split interstitial defect with another oxygen atom, leaving behind an isolated O vacancy. The Al PKA regained its lattice site during this process which is illustrated in fig. 4.5. A similar event was observed for the smallest energy threshold along the [7 1 2] direction which is slightly offset from the [1 0 0] path.

The threshold energy calculations initiated by Al PKAs at both 125 K and 300 K resulted mainly in antisites, followed by mixed cation split interstitials of the form $Mg_i^{\cdot\cdot}$–V''_{Mg}–$Al_i^{\cdot\cdot\cdot}$ and anion split interstitials O''_i–$V_O^{\cdot\cdot}$–O''_i. Most of the replacement reactions occurred on the Al sublattice as shown in tables 4.2 and 4.3. At 125 K, 38 % of the cascades (5 out of 13 simulations) resulted in perfect crystals, with only 2 Al ions swapping sites. These were obtained along the [1 1 1] direction at the threshold energy of 77.5 eV, and along [2 3 2], [1 3 1], [1 4 1] and [1 5 1] which had the same

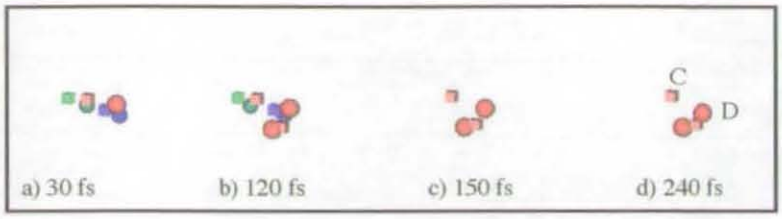

Figure 4.5: Defect evolution for an Al PKA, head-on towards an O ion along [1 0 0]. The PKA energy was 75 eV. Final defects are shown in (d), consisting of an oxygen vacancy (C) separate from an oxygen split interstitial (D).

threshold energy of 82.5 eV.

O PKA

The oxygen PKA caused no damage or replacement sequences on either of the Mg or Al sublattices, but instead produced replacements and Frenkel pairs on the anion sublattice. The anion Frenkel pairs were typical of what is shown in fig 4.5 (d) consisting of an isolated vacancy and a split interstitial defect. No damage occurred in 4 out of 13 simulations at 125 K where O ions just swapped sites. These occurred when the PKA was directed along [2 3 2], [3 1 8], [1 1 0] and [1 3 1] at the corresponding threshold energies of 47.5 eV, 67.5 eV, 112.5 eV and 47.5 eV.

The lowest E_d was 27.5 eV at 125 K along the [1 0 0] direction, whereas the highest recorded value was 112.5 eV along the [1 1 0] direction. In the former simulation, the PKA easily moved along that direction as compared to the latter one whereby the PKA was head-on to another anion which required more kinetic energy to create permanent displacements. The lowest energy cascade resulted in an isolated oxygen vacancy and a corresponding split interstitial defect whereas the highest energy cascade produced no damage but only replacements (see fig. 4.6). Along the other directions investigated, similar mechanisms were observed.

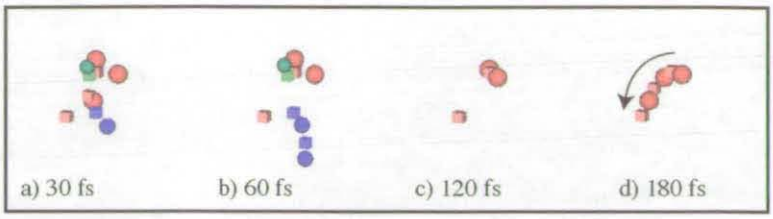

Figure 4.6: Defect production and annihilation for the highest E_d of 112.5 eV for an O PKA along [1 1 0]. No damage remains after 180 fs.

4.2.3 Discussion

The threshold displacement energy is an important parameter in ion range and energy deposition calculations performed by the Monte-Carlo (MC) code SRIM (The Stopping and Range of Ions with Matter) [66]. These calculations are much faster to perform than MD and allow implantation profiles and defect distributions to be obtained easily and quickly. For calculations performed in magnesium aluminate spinel, a threshold displacement value of 40 eV has been commonly used irrespective of the atom species [67, 68]. However, our results show that there is a large variation in E_d with respect to the PKA species and on its direction. Even the least average value shown in table 4.1 is around 60 eV for the oxygen atom. Thus the MD calculations can be used to parametrise the MC codes more accurately.

Only one known measurement of the threshold displacement energy has been conducted experimentally in magnesium aluminate spinel by Summers *et al.* [65]. Here, E_d was measured only for the oxygen ion at temperatures of 77 K and 300 K and was found to be 59 eV at the lower temperature and 130 eV at the higher temperature. The higher E_d at the higher temperature was attributed to the instability of interstitial-vacancy pairs immediately after their creation as compared to the lower temperature. The experimental value of 59 eV for the oxygen ion at 77 K is in good agreement with the averaged value of 60 eV obtained from our simulations at 125 K.

The average threshold energy over all directions, shown in table 4.1, is lower at the higher temperature for the Mg PKA, but remains almost unchanged for the Al and O sublattices.

Williford *et al.* [69] determined the threshold energies in several ceramics including $MgAl_2O_4$ using the GULP simulation code [70]. Their calculations were based on the Bush *et al.* potential [45]. For the oxygen sublattice, the calculated E_d values along three different orientations were 22.1 eV, 40.3 eV and 76.3 eV; only one value of 51 eV was reported for the Al sublattice; whereas two E_d values of 61.4 eV and 58.7 eV were obtained for the Mg sublattice. The numbers in table 4.1 show that the E_d range is 34.2 – 277.5 eV for Mg, 55.8 – 157.5 eV for Al, and 27.5 – 112.5 eV for O. The larger spectrum of E_d is observed in this thesis due to a wider range of initial directions chosen for the PKA in contrast to other studies.

Although the spinel structure differs from that of zircon, for both materials, the threshold displacement energies were much lower for the oxygen sublattice as compared to the cation sublattices [64]. A similar trend was observed in MgO whereby a lower threshold energy was obtained for the anion sublattice [73].

4.3 Point defect energies

For PKA energies near E_d, the main defect structures remaining in the spinel structure comprised of a split interstitial with a corresponding isolated vacancy or/and cation antisites. The split interstitial structures consist of either two oxygen ions sharing an oxygen lattice site, two Mg ions sharing a Mg site or split Mg–Al interstitials sharing a vacant Mg site. In order to investigate how the defects differ from each other energetically, their defect formation energies were evaluated. The defect formation energy is the amount of energy required to introduce the defect into the perfect crystal. The defect formation energies for the antisites and each of the split interstitial types have been determined using the damped MD method. First, the

total potential energy ($E_{perfect}$) of a perfect magnesium aluminate crystal containing 7166 atoms was obtained by standard minimisation using damped MD. Then the defects were introduced into the structure and the system was minimised to obtain its total potential energy (E_{defect}). The difference in $E_{perfect} - E_{defect}$ denotes the defect formation energy provided that both the perfect cell and the defective cell contain an identical number of atoms.

For cation antisites, a pair of Mg'_{Al} and $Al^{\cdot}_{Mg}$ antisites was created by swapping a Mg atom with an Al atom in the perfect structure. The energy associated with the formation of an antisite pair as a function of the separation between the Mg'_{Al} and $Al^{\cdot}_{Mg}$ defects was determined. The results are shown in fig. 4.7 and are compared with *ab-initio* results [71]. The empirical potential calculations overestimate the formation energies by about 0.3 eV as compared to *ab-initio* results, but both techniques show a similar trend as a function of antisite separation. The lowest formation energy was found to be 0.8 eV (0.49 eV *ab-initio*) when the antisite pair was closest at $\approx$ 3.3 Å. For the next pair separation at $\approx$ 5.2 Å, a steep rise of about 0.2 eV was observed in the formation energy. Both empirical potentials and *ab-initio* calculations show that the energy became larger with increasing defect separation. However, these energies would be expected to remain constant as the antisite pair separation becomes larger and larger. For an infinitely separated antisite pair, *ab-initio* calculations give a value of 0.64 eV as the formation energy [71] while the empirical potentials give a value of 1.50 eV.

The formation of antisites produces some local strains which cause changes in cation-anion bond lengths around the defects. The cation-anion bond length in a perfect crystal can be compared to that around an antisite defect in table 4.4. The results show that when an Al ion replaces a Mg, the cation-anion bond length around that site decreases from 1.99 Å to 1.80 Å. In the reverse process, when a Mg ion replaces an Al ion, the cation-anion bond length around that site increases from 1.89 Å to 2.05 Å. Fig. 4.9 shows how the oxygen atoms around the antisites relax such

Table 4.4: Cation-anion bond lengths (measured in Å) in the perfect structure and around antisites. The results are in good agreement with *ab-initio* results [71].

Method of calculation	Perfect structure		Defective structure	
	Mg–O bond	Al–O bond	$Al^{\cdot}_{Mg}$–O bond	Mg'_{Al}–O bond
Empirical potentials	1.99	1.89	1.80	2.05
Ab-initio	1.92	1.90	1.79	2.03

as to compensate for the charge imbalance brought about by the antisite defect (+1 for an $Al^{\cdot}_{Mg}$ and −1 for a Mg'_{Al}). The four oxygen atoms around an $Al^{\cdot}_{Mg}$ antisite shown in fig. 4.9 (b), are attracted by the extra charge but at the same time, become over-bonded as discussed in section 2.1.4. This results in longer bonds l_4 shown in fig. 4.9 (b) as compared to l_2. However, a Mg'_{Al} antisite causes the six oxygen atoms around it to be under-bonded resulting in bonds l_5 and l_6 to shrink while bond l_7 increases as illustrated in fig. 4.9 (c).

The simulations performed at threshold energies in magnesium aluminate spinel show that interstitial defects generally occurred as split interstitials and not as isolated interstitials. Pure Mg and O split interstitials, and Mg–Al split interstitials centred around a Mg vacancy were seen. However, pure Al split interstitials or Mg–Al ions around an Al vacancy were never observed. The defect formation energies for the observed interstitial defects have been evaluated in the same way as discussed for the antisites. In each case, the system contained a vacant lattice site and a split interstitial and both defects were separated by a varying distance. The defect formation energies as function of that separation are illustrated in fig. 4.8. It can be seen that the pure Mg and O defect energies are quite similar but the energy of the $Mg^{\cdot\cdot}_i$–V''_{Mg}–$Al^{\cdot\cdot\cdot}_i$ defect is higher. For the oxygen defects, the split interstitial recombined with the vacancy when the defects were separated by 4.72 Å. In all three cases, as the separation between the interstitials and their vacant site increases, the energy of the defect also increases. Our results are in agreement with *ab-initio* calculations which

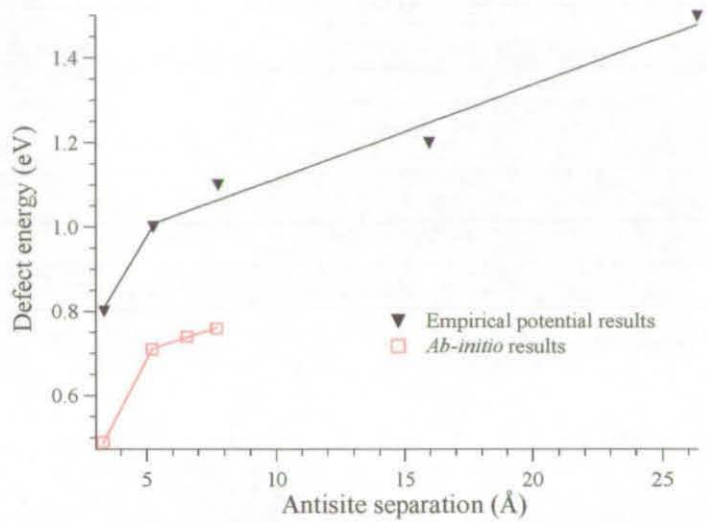

Figure 4.7: Defect energies for a Mg'_{Al} and an $Al^{\cdot}_{Mg}$ antisite pair as a function of their separation. The trend is similar for *ab-initio* calculations [71] performed using the PLATO code (Package for Linear-combination of Atomic Orbitals) [72].

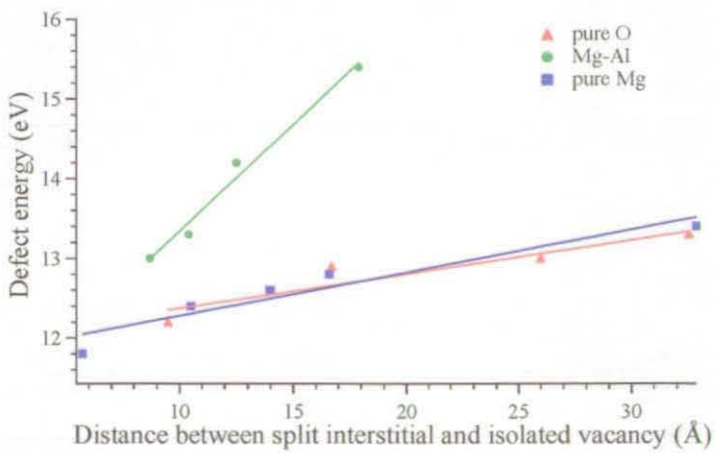

Figure 4.8: Defect energies for the different split interstitial defects as a function of the distance between the defect and its corresponding isolated vacant site.

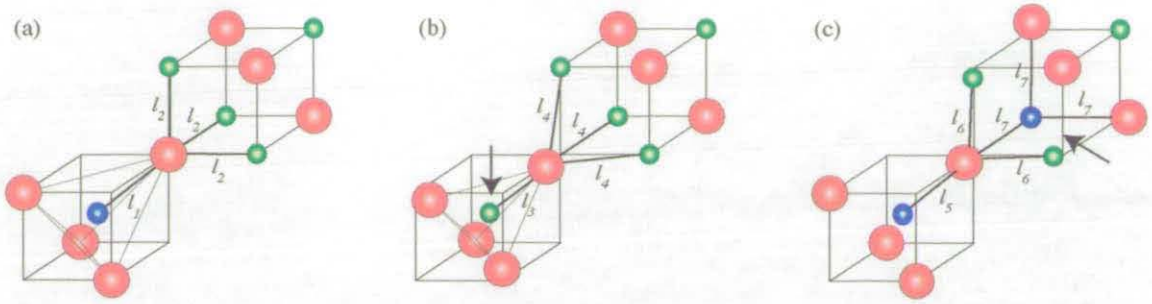

Figure 4.9: Schematic diagram representing strains induced by cation antisites (indicated by arrows). (a) Perfect spinel structure. (b) $Al^{\cdot}_{Mg}$ antisite. (c) Mg'_{Al} antisite. The bond lengths, l_x, are given in table 4.5.

also predict the Mg–Al split interstitials to be higher in energy than the pure Mg split interstitials. The formation energy for an infinitely separated split interstitial with the corresponding vacancy obtained from *ab-initio* calculations [71] is 6.40 eV for the pure Mg split interstitial as compared to 9.22 eV for the Mg–Al complex. The empirical potential calculations of the formation energy for the infinitely separated Mg split interstitial with the corresponding vacancy is 12.27 eV, this value is 15.07 eV for the mixed Mg–Al split interstitial and the isolated Al vacancy, while for the O split interstitial and the isolated O vacancy the formation energy is 12.81 eV.

Table 4.5: Table of bond lengths labelled l_x in fig. 4.9. All values are given in Å.

Perfect		$Al^{\cdot}_{Mg}$ antisite		Mg'_{Al} antisite	
l_1	1.99	l_3	1.80	l_5	1.95
l_2	1.89	l_4	2.00	l_6	1.84
				l_7	2.05

Antisite defects were found to be immobile during the threshold energy simulations whereas split interstitials could either remain in the structure as shown in fig. 4.5 or recombine with vacancies as illustrated in figs. 4.4 and 4.6. It was found that the split interstitials were all aligned along the $\langle 110 \rangle$ directions. The defects are not linear and

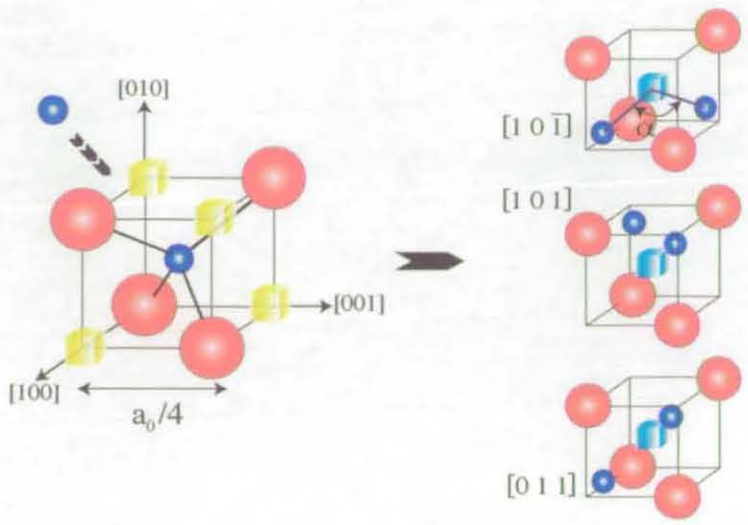

Figure 4.10: Cation split interstitial configuration in magnesium aluminate spinel. The left figure shows a tetrahedrally coordinated Mg ion in its perfect arrangement. The yellow cubes denote structural octahedral vacancies. An interstitial cation destabilises this configuration by forming a split interstitial defect which aligns along ⟨110⟩ (3 configurations are shown in the right figure). Both interstitials occupy two of the four structural octahedral vacancies, subtending an angle α with the central Mg vacancy. The rocksalt structure would arise if the two other vertices were also filled in the same way.

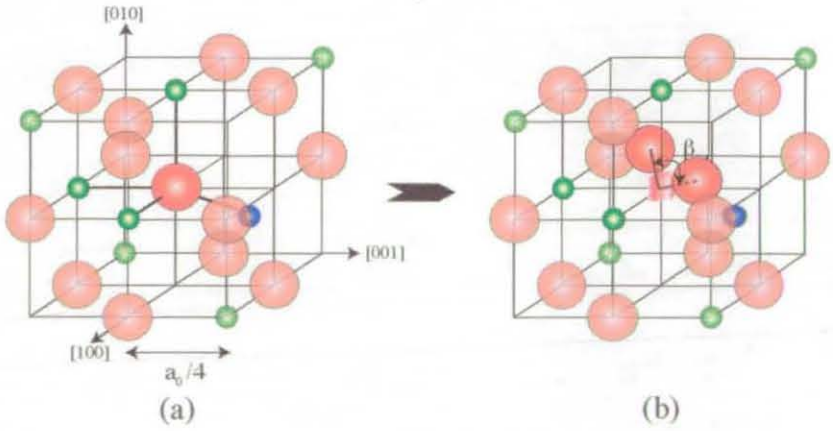

Figure 4.11: (a) The oxygen sublattice is made up of ⟨110⟩ rows in the perfect spinel structure. (b) Anion split interstitial defects form along the same ⟨110⟩ directions but both interstitials form an angle β with the central vacancy as shown.

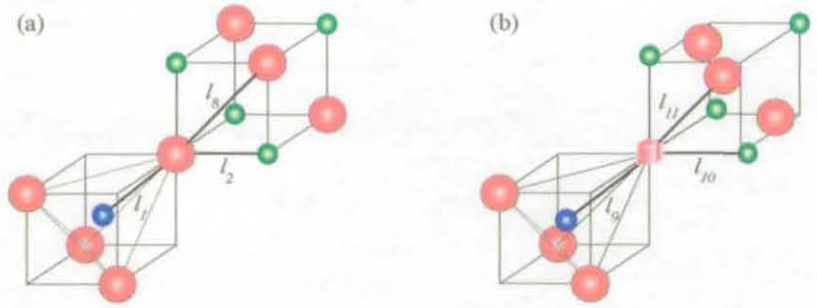

Figure 4.12: Schematic diagram showing the relaxation around an oxygen vacancy. The perfect structure is given in (a) and the $V_O^{\cdot\cdot}$ defect is shown in (b). All bond lengths, l_x, are given in table 4.6.

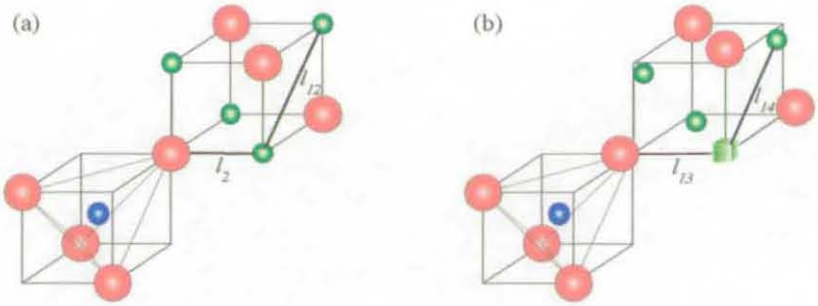

Figure 4.13: Schematic diagram showing the relaxation around an aluminium vacancy. The perfect structure is given in (a) and the $V_{Al}^{'''}$ defect is shown in (b).

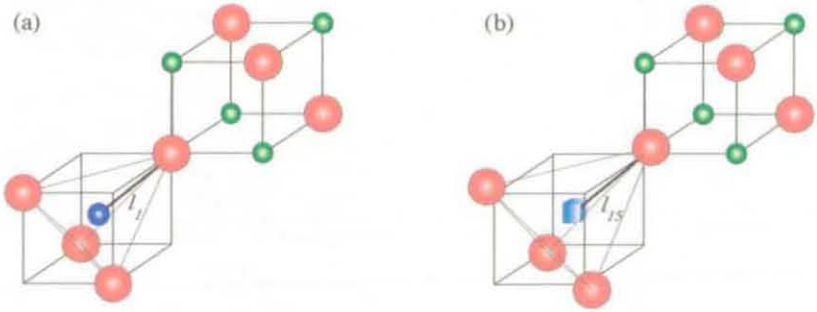

Figure 4.14: Schematic diagram showing the relaxation around an aluminium vacancy. The perfect structure is given in (a) and the $V_{Mg}^{''}$ defect is shown in (b).

the two interstitials subtend an angle with the site they share. Thus they are not pure dumbbell defects as, for example, in α-Fe where this angle is 180°. Figures 4.10 and 4.11 show the environment around the $Mg_i^{\cdot\cdot}$–V''_{Mg}–$Mg_i^{\cdot\cdot}$ and the O_i''–$V_O^{\cdot\cdot}$–O_i'' split interstitial defects respectively. The mixed Mg–Al split interstitials have the same configuration as the pure Mg split interstitials whereby the interstitials are close to the structural octahedral vacancies as shown in fig. 4.10. The angles between the two interstitials and its central vacancy for the $Mg_i^{\cdot\cdot}$–V''_{Mg}–$Al_i^{\cdot\cdot\cdot}$ defect was averaged as 128.5° ± 5.5° (mean of 9 defects ± standard deviation) and for the pure $Mg_i^{\cdot\cdot}$–V''_{Mg}–$Mg_i^{\cdot\cdot}$ this was 128.8° ± 7.8° (mean of 20 defects). This implies that the interstitials do not sit exactly on these octahedral sites because otherwise those angles would be equal to 109.5°. For a $Mg_i^{\cdot\cdot}$–V''_{Mg}–$Mg_i^{\cdot\cdot}$ defect, the $Mg_i^{\cdot\cdot}$–V''_{Mg} distance was found to be 1.34 Å, whereas in the mixed $Mg_i^{\cdot\cdot}$–V''_{Mg}–$Al_i^{\cdot\cdot\cdot}$ defect, the cation–V''_{Mg} distance was 1.42 Å. If they sat exactly on the octahedral sites, this would be 1.76 Å.

The interstitials forming anion split interstitials are relatively far from the closest unoccupied structural tetrahedral vacancies. This might be due to the presence of four oxygen ions around the structural tetrahedral vacancy sites which restricts the two interstitials closer to central the oxygen vacancy rather than away from it towards those structural vacancies. Similarly, no oxygen interstitial was found at structural octahedral vacancies because of the repulsive interaction with the six other oxygen ions around that site. The angle between the two O_i'' interstitials and the central vacancy $V_O^{\cdot\cdot}$ for the O_i''–$V_O^{\cdot\cdot}$–O_i'' defect was found to be 137.0° ± 6.2° (mean of 23 defects) and the O_i''–$V_O^{\cdot\cdot}$ distance was found to be 1.18 Å.

For the defect formation energy simulations of the split interstitial with its isolated vacancy, the relaxation around each vacancy was analysed. The relaxation around each of the $V_O^{\cdot\cdot}$, V''_{Mg} and V'''_{Al} is shown in figs. 4.12, 4.13 and 4.13 respectively. The bond lengths indicated in the corresponding figures are given in table 4.6. These results show that the cation vacancies create more local distortion as compared to the antisites.

Table 4.6: Table of bond lengths labelled l_x in figs. 4.12, 4.13 and 4.14. All values are given in Å.

Perfect		$V_O^{\cdot\cdot}$		$V_{Al}^{'''}$		$V_{Mg}^{''}$	
l_1	1.99	l_9	2.54			l_{15}	2.22
l_2	1.89	l_{10}	2.12	l_{13}	2.29		
l_8	2.46	l_{11}	2.29				
l_{12}	2.85			l_{14}	2.77		

The calculated defect energies clearly show that cation antisites are more likely to form as compared to split interstitials. Chen *et al.* [42] also predicted antisite defects to be the most energetically favourable defects in $MgAl_2O_4$ because their arrangement involves the smallest amount of distortion of the lattice as compared to other defects.

4.4 Collision cascades

Magnesium aluminate is well-known for its resistance to radiation by highly energetic particles. It is considered as a potential candidate for nuclear waste storage and other related applications which would explore its radiation resistant property. In irradiation environments, the emission of energetic particles, such as heavy actinide nuclei, occurs in the regime of 70-100 keV rather than just in the eV range [74]. In order to gain further insight of damage production in more violent conditions, collision cascades in the energy range of 400 eV to 10 keV were investigated in $MgAl_2O_4$. Sets of simulations were performed for those energies along different directions and with different PKA species, rather than just simulating very high energy cascades (> 10 keV). In this way, meaningful statistical information on the cascade behaviour can be obtained. The details of the collision cascades are given in the next subsection, followed by the results subsections.

4.4.1 Details of the cascade simulations

The energetic cascades were initiated in the same way as in the threshold displacement energy cascades by providing extra kinetic energy to the PKA along a specified path. We investigate collision cascades of defect production and relaxation occurring on the time scale of picoseconds for different PKA energies of 0.4 keV, 2 keV, 5 keV and 10 keV. The simulations were performed in cubic cells of different sizes containing 12 331, 97 669, 450 461 and 988 391 charged particles for the above mentioned energies. Each of the simulation cells were neutrally charged but were not periodically repeated. As such, three layers of atoms were fixed at the boundaries to stabilise the crystal in all simulations performed. In order to investigate the effect of the feedback resulting from the fixed layers on the cascade evolution, an identical 0.4 keV simulation was performed in two cells containing 12 331 atoms with different boundary conditions. The first cell had only three layers of fixed atoms at the boundaries, while the second cell had three extra layers of damped atoms before the three layers of fixed atoms. Both cascades remained more than 10 Å from the fixed boundaries and evolved almost identically resulting in the same defect structures. As such, all the energetic cascades were performed in the active region of the simulation cell, ensuring that they were sufficiently far from the boundaries by more than 10 Å. Only fixed boundaries were used.

The low 0.4 keV cascades were investigated because they have shown to generate defects similar to those observed at higher energies in MgO [75] while using modest computing resources. By increasing the initial knock-on energy to 2, 5 and 10 keV the evolution of larger cascades could be investigated in spinel due to an increased number of atomic collisions, thus requiring larger simulations cells. The 10 keV simulations could be contained in cells with 988 391 ions whereas for energies beyond 10 keV, simulation cells containing more than 1 million charged particles are required. We chose to limit the maximum energy studied to 10 keV because the simulations were done in three spinels ($MgAl_2O_4$, $MgGa_2O_4$ and $MgIn_2O_4$) using limited computing

resources.

In this section, the damage created in the normal $MgAl_2O_4$ spinel is investigated. A total of 27 simulations was performed at the low energy of 0.4 keV, 24 simulations at energies of 2 keV and 5 keV, and a set of 8 simulations for the 10 keV cascades. In order to ensure that each individual cascade was unique and also that the results were statistically distributed for a given energy, different PKA directions, representative of a range of solid angles, as well as different species (Mg^{2+}, O^{2-} or Al^{3+}) were selected. Each trajectory was initiated at a temperature of 0 K and followed until the system has stabilised ($\approx$ 10 ps). The temperature rise for the 0.4 keV cascades was about 170 K, for the 2 keV simulations this was about 100 K, while for the 5 keV and 10 keV simulations the temperature increase was about 50 K.

The likelihood of any specific type of ion being hit during a collision event in the polyatomic $MgAl_2O_4$ spinel is dependent on the collision cross-section of the different atomic species. For low interaction energies this can be approximated by Rutherford scattering and is proportional to the repulsive nuclear charge between the interacting ions. Under this approximation, we would expect that the largest scattering cross-section to be Al-Al followed by Al-Mg and then Mg-Mg and O-O. However, the scattering for Al-O and Mg-O is primarily determined by the ZBL potential at these energies. According to the ZBL interaction for collisions occurring at 1 keV, an Al projectile targeting an O ion has a larger scattering cross section as compared to a Mg projectile targeting an O ion.

The defects remaining at the end of the simulations characterise the damage imparted to the structure. We compare and contrast the damage caused to the different sublattices in $MgAl_2O_4$ spinel.

4.4.2 400 eV cascades

A total of nine simulations were performed for each PKA at 400 eV. The maximum number of displaced ions occurred on average 82 fs after the PKA was set in motion.

In general, most displaced ions recombined to lattice sites within the first picosecond leaving only a few surviving defects. The mean and standard deviation of the number of defects generated per trajectory for each PKA is given in table 4.7. The 400 eV cascades were characterised mainly by the formation of split interstitials, cation antisites and isolated vacancies which were already observed at the threshold energies.

Table 4.7: Mean and standard deviation of the number of defects obtained per trajectory for 400 eV PKAs in spinel. 'Al complex' refers to an Al split vacancy defect which has an O vacancy next to one of its Al vacancies.

PKA	Split interstitials			Isolated vacancies			Antisites		Al complex
type	Mg	O	Mg–Al	V''_{Mg}	V'''_{Al}	$V_O^{\cdot\cdot}$	$Al_{Mg}^{\cdot}$	Mg'_{Al}	split vac.
Mg	0.9 ± 0.3	0.1 ± 0.3	0.2 ± 0.4	1.0 ± 0.5	0.0	0.0	0.4 ± 0.5	0.7 ± 0.5	0.0
Al	0.6 ± 0.5	0.4 ± 0.5	0.1 ± 0.3	0.0	0.3 ± 0.5	0.1 ± 0.3	1.1 ± 0.3	0.6 ± 0.5	0.2 ± 0.4
O	0.0	0.6 ± 0.5	0.0	0.0	0.0	0.6 ± 0.5	0.1 ± 0.3	0.1 ± 0.3	0.0

For the Mg PKA, the predominant defects occurring were a Mg split interstitial $Mg_i^{\cdot\cdot}$–V''_{Mg}–$Mg_i^{\cdot\cdot}$, and an isolated Mg vacancy V''_{Mg} left behind by the PKA. Fig. 4.15 (a) illustrates the damage caused by a Mg PKA directed along [1 3 5] comprising of a split Mg interstitial separated from an isolated vacancy with one Al and one Mg antisites. Along the [1 7 11] path, the final damage is shown in fig. 4.15 (b).

Out of the 9 trajectories, 3 ended up without any damage to the crystal when O was the primary knock-on atom. No damage was obtained along the [2 1 0], [2 3 2] and [1 7 11] directions. During these simulations, two O split interstitials remained after the collisional phase with the corresponding number of isolated vacancies. The perfect crystal was recovered through a series of replacement mechanisms over the O sublattice, an example of which is shown in fig. 4.16. The remaining cascades typically resulted in 1 anion split interstitial O''_i–$V_O^{\cdot\cdot}$–O''_i with an isolated $V_O^{\cdot\cdot}$ (see fig. 4.15 (c)). The cation sublattice remained unaffected in most cases.

The Al PKA produced twice as many Al antisites as compared to Mg antisites. The other defect structures obtained were Mg and O split interstitials as shown in fig.

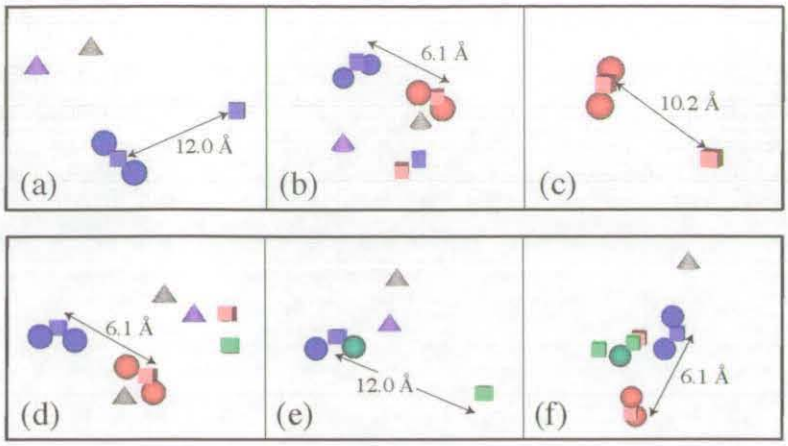

Figure 4.15: Point defects observed at 400 eV in $MgAl_2O_4$. (a) Mg^{2+} PKA initiated along [1 3 5], (b) Mg^{2+} PKA initiated along [1 7 11], (c) O^{2-} PKA along [1 7 3], (d) Al^{3+} PKA along [1 7 5], (e) Al^{3+} PKA along [1 2 3], (f) Al^{3+} PKA along [1 7 3]. Cones represent antisites (purple –Mg'_{Al}; grey – $Al^{\cdot}_{Mg}$). The arrows indicate the distance between two arbitrarily chosen defects and is a rough indication of the spread of the damage.

4.15 (d), and a mixed Mg–Al split interstitial centred about a Mg vacancy (fig. 4.15 (e)). Two simulations resulted in a defect configuration including an Al interstitial trapped between 2 adjacent Al vacancies forming a split vacancy defect. Such a situation is illustrated in fig. 4.15 (f).

The low-energy 0.4 keV cascades showed how cation interstitials form relatively stable split interstitials during the collisional phase of the cascade. In some cases, these could diffuse locally on the cation sublattice and annihilate completely or form stable antisites by the end of the cascades. For the 400 eV cascades studied, cation split interstitials centred about an Al vacancy were not observed. Oxygen split interstitials could annihilate with neighbouring vacancies if the axis of the split interstitial was in the direction of the O vacancies, leading to a one-dimensional diffusion mechanism. Conversely if the O split interstitial had its axis perpendicular to that joining its central vacancy to the neighbouring O vacancy as shown in fig. 4.15 (c) the defect was trapped. Then extra energy was required for the configuration to align along the favourable direction before migrating. Al antisites could easily pin the O split

interstitial to prevent the latter from migrating (see fig. 4.15 (b) and (d)).

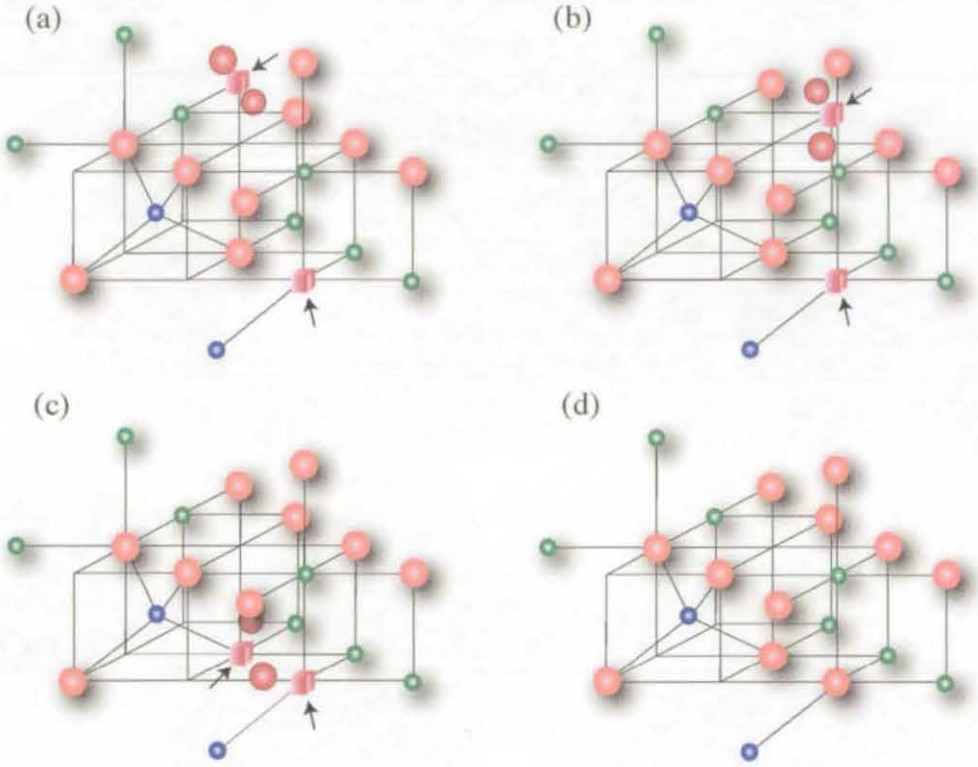

Figure 4.16: The migration path of an O split interstitial towards an O vacancy in the annealing parts of a cascade, yielding a perfect lattice structure. Initially, the defects were separated by 7.7 Å. (a) The initial interstitial formation which remained stable from 735 fs to 1485 fs after the start of the cascade; (b) 1511 fs; (c) 1536 fs; (d) 1560 fs. The vacant sites are marked by the arrows.

4.4.3 2 – 10 keV cascades

By increasing the PKA energy, more defects were created which spread over a larger volume of the simulation cell. The high energy cascades branched into smaller subcascades which resulted in similar defect structures as observed at the low 0.4 keV cascades. An example of subcascade formation at 2 keV is shown in fig. 4.17 (b) for an Al PKA directed along [1 6 2]. This cascade also depicts a typical antisite formation mechanism which is encircled in fig. 4.17.

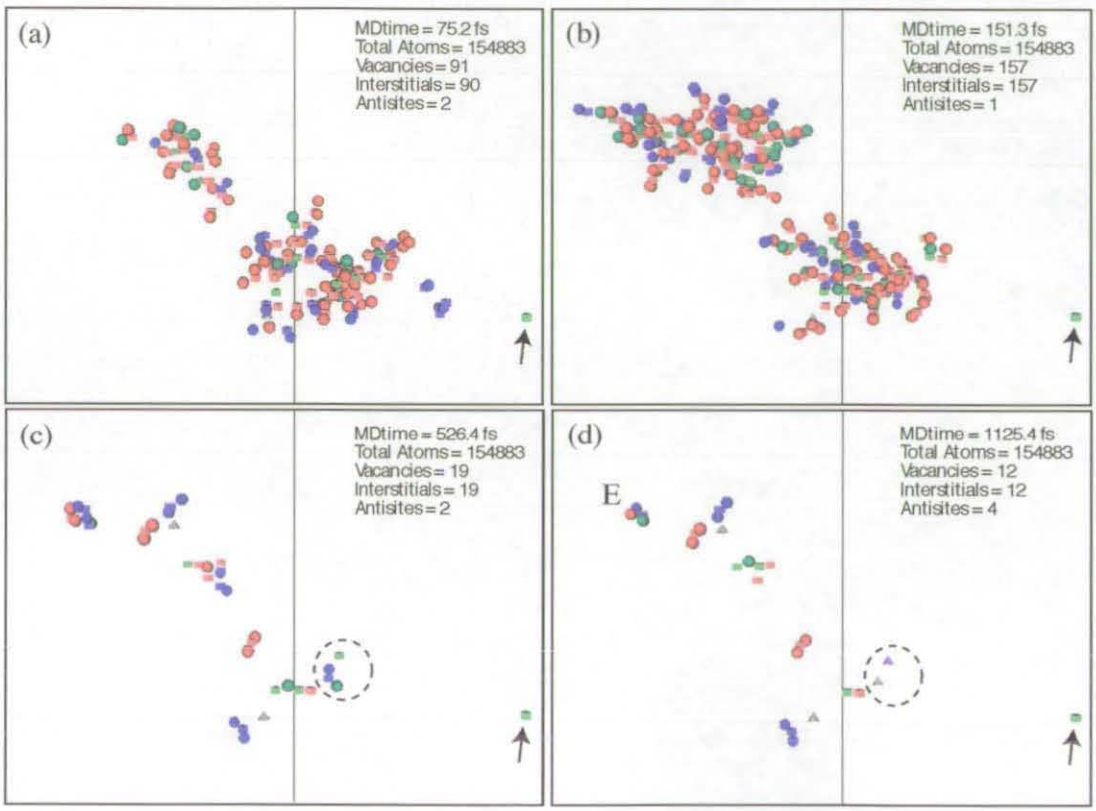

Figure 4.17: Snapshots of a 2 keV cascade in $MgAl_2O_4$ initiated along [1 6 2] by an Al PKA. The PKA site is indicated by an arrow. Two distinct subcascade regions can be observed in (b). The final damage in (d) is similar to those seen at 0.4 keV in fig. 4.15 except for defect marked E consisting of a $Mg_i^{\cdot\cdot}$–V''_{Mg}–$Al_i^{\cdot\cdot\cdot}$–O_i'' cluster. The encircled region depicts a typical antisite formation mechanism.

Beside the formation of typical split interstitials and antisites, cascades in the energy regime of 2 – 10 keV produced a few interesting ring structures on the Al^{3+} sublattice. These defects are termed 'ring' defects because of their distinctive configuration consisting of a closed loop of 3 alternate Al ions and vacancies. In the ring defects, three Al interstitials are displaced from their octahedral sites to adjacent structural tetrahedral vacancy sites in the lattice as shown in fig. 4.18. One such defect can also been seen as part of the residual damage left by a 2 keV PKA in fig. 4.19 (a) and is labelled F. The Al ring structure has a formation energy of 10.2 eV. This is much larger than the formation energy of antisite pairs but less than the vacancy-split interstitial Frenkel pairs. The formation of these ring defects can absorb a significant amount energy from the cascades but only lead to a local rearrangement of the lattice.

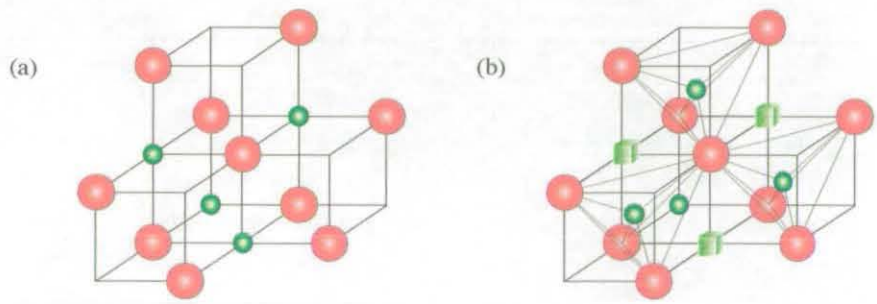

Figure 4.18: (a) Local environment in a perfect spinel around Al ions. (b) Spatial configuration of a ring defect whereby the three octahedrally coordinated Al ions moved to tetrahedral sites.

Fig. 4.19 shows the difference in final damage obtained at 2 keV when choosing different PKAs along the same [1 1 1] direction. Along that path, the cascade initiated by the O PKA spread out the most as compared to the cation PKAs. The development of a typical collision cascade at the energy of 5 keV for a Mg PKA along [1 1 3] is illustrated in fig. 4.20. The defects generated by a 10 keV Mg PKA directed along [2 4 3] are shown in fig. 4.21. Fig. 4.22 showing the damage produced by a 10 keV Mg PKA along [2 3 2] was performed in a simulation cell containing more than 3 million

atoms.

As a result of the displacement cascades on the cation sublattice, cation interstitials could occupy octahedral sites when forming split interstitials (see fig. 4.10) while the formation of split vacancy and ring defects on the Al sublattice caused interstitials to occupy tetrahedral sites. Ring defects with one or two Mg interstitials were also occasionally observed but more prevalent were isolated vacancies, cation-anion vacancy pairs and antisites, the Al vacancy often occurring paired with an anion vacancy. A few cation crowdion defects were also observed at the higher energies. Crowdions are extended split interstitials with an extra vacancy and interstitial. Two examples of cation crowdions are shown in fig. 4.21. These are $Mg_i^{\cdot\cdot}$–V''_{Mg}–$Al_i^{\cdot\cdot\cdot}$–V''_{Mg}–$Mg_i^{\cdot\cdot}$ and $Mg_i^{\cdot\cdot}$–V''_{Mg}–$Mg_i^{\cdot\cdot}$–V''_{Mg}–$Al_i^{\cdot\cdot\cdot}$. During the recrystallisation phase, interstitial-vacancy recombination occurred via the diffusion of interstitials rather than vacancies. By the end of the cascade simulations, very little defect motion was observed in the structure.

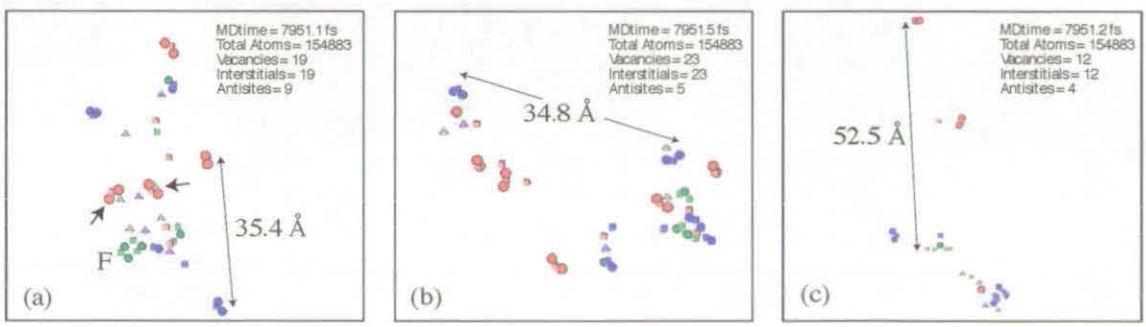

Figure 4.19: Surviving defects generated at 2 keV along [1 1 1]. (a) Mg PKA - a ring defect consisting of 3 alternate Al vacancies and interstitials is labelled F. Arrows indicate O split interstitials pinned by an Al'_{Mg} antisite, (b) Al PKA, (c) O PKA - along this direction, the oxygen PKA could channel through the crystal forming a few defects only.

For the 2 keV and 5 keV simulations, 8 different trajectories were performed for each PKA, whereas for the 10 keV simulations, only 4 trajectories were performed for Mg and Al PKAs only. O PKAs could not be investigated at the energy of 10 keV because of long range channelling. It was not possible to contain an anion PKA cascade even using a lattice of 3 million atoms. The number of defects created per

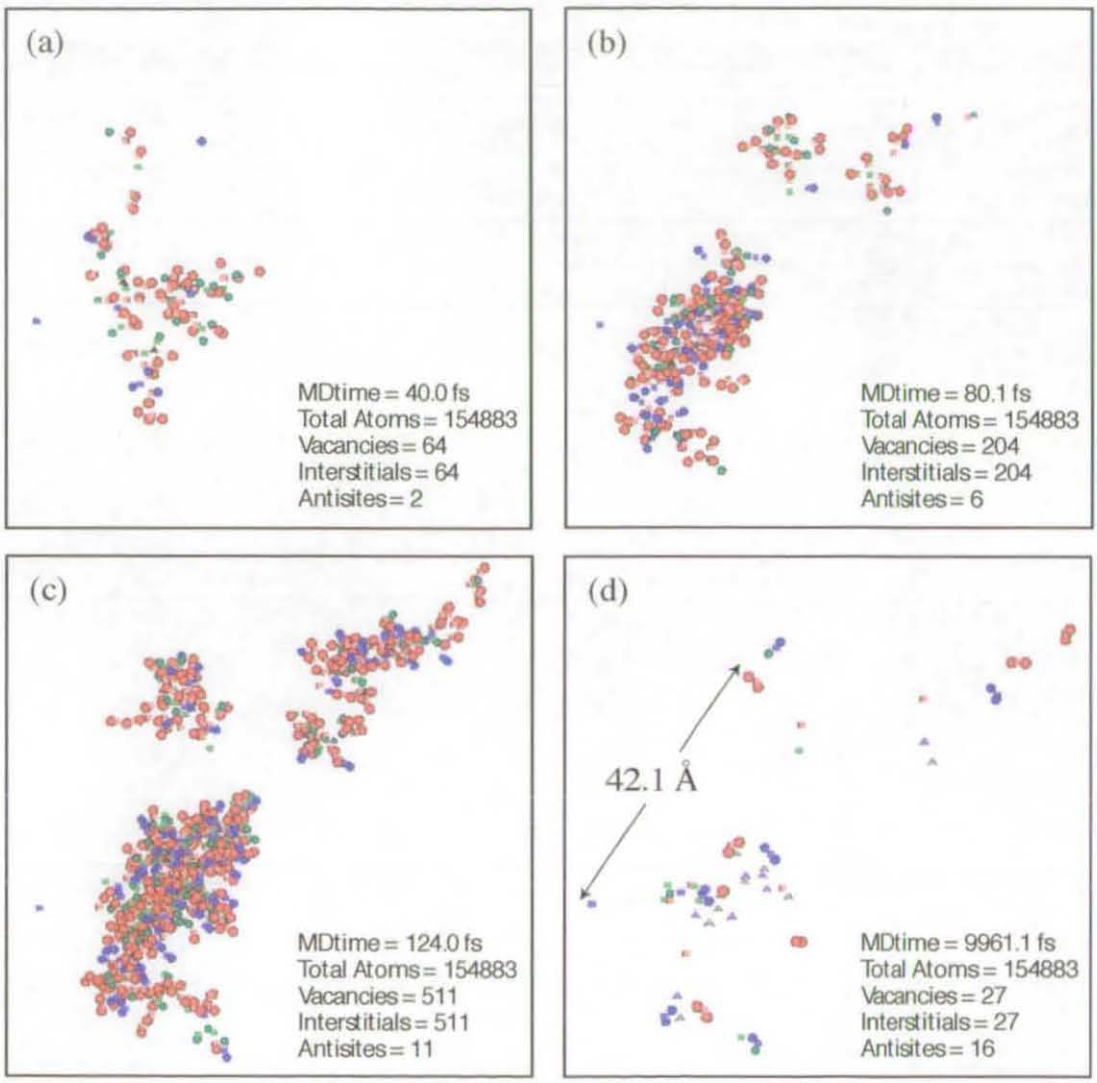

Figure 4.20: The formation and recombination of defects during a 5 keV cascade for a Mg PKA along [1 1 3].

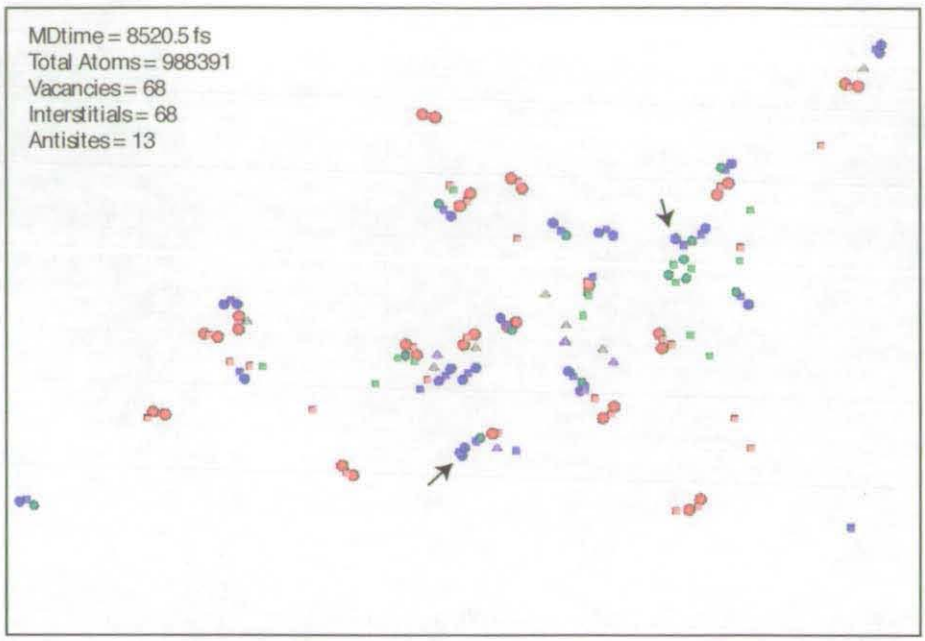

Figure 4.21: Damage caused by a 10 keV Mg PKA directed along [2 4 3] in a cubic simulation cell of length 212 Å. Cation crowdions are indicated by arrows.

simulation for each of the Al, Mg and O PKAs is given in tables 4.8, 4.9 and 4.10 respectively. In all three tables, a similar trend can be found. Firstly, irrespective of the PKA type, most simulations resulted in slightly more $Al^{\cdot}_{Mg}$ than Mg'_{Al}. The second observation is directly related to the threshold energy values determined earlier. The lowest displacement threshold was obtained for the anion sublattice which was the most affected in the cascade simulations. This is indicated by the highest numbers of oxygen interstitials and vacancies in the three tables 4.8, 4.9 and 4.10. In general, the least number of interstitials occurred on the Al sublattice.

4.5 Conclusions

In this chapter, the radiation response of normal magnesium aluminate spinel was investigated at near-threshold energies and at higher energies of 0.4 keV to 10 keV. Both threshold energy simulations and collision cascades indicate that it is easier

Table 4.8: Mean and standard deviation of the number of defects formed per simulation for an Al PKA at energies of 2 keV (total of 8 simulations), 5 keV (total of 8 simulations) and 10 keV (total of 4 simulations).

PKA energy (keV)	Antisites		Interstitials			Vacancies		
	Mg'_{Al}	$Al^{\cdot}_{Mg}$	$Mg^{\cdot\cdot}_{i}$	$Al^{\cdot\cdot\cdot}_{i}$	O''_{i}	V''_{Mg}	V'''_{Al}	$V_O^{\cdot\cdot}$
2	2.3 ± 1.3	3.1 ± 1.2	5.1 ± 1.5	4.9 ± 2.0	7.0 ± 2.9	4.3 ± 1.4	5.8 ± 1.6	7.0 ± 2.9
5	5.3 ± 1.8	7.5 ± 2.6	9.9 ± 2.7	5.5 ± 1.5	14.4 ± 3.6	7.6 ± 1.8	7.8 ± 1.7	14.4 ± 3.6
10	9.3 ± 2.2	11.3 ± 3.3	18.5 ± 3.1	13.3 ± 4.0	25.5 ± 3.1	16.5 ± 3.0	15.3 ± 4.5	25.5 ± 3.1

Table 4.9: Mean and standard deviation of the number of defects formed per simulation for a Mg PKA at energies of 2 keV (total of 8 simulations), 5 keV (total of 8 simulations) and 10 keV (total of 4 simulations).

PKA energy (keV)	Antisites		Interstitials			Vacancies		
	Mg'_{Al}	$Al^{\cdot}_{Mg}$	$Mg^{\cdot\cdot}_{i}$	$Al^{\cdot\cdot\cdot}_{i}$	O''_{i}	V''_{Mg}	V'''_{Al}	$V_O^{\cdot\cdot}$
2	2.4 ± 1.1	2.3 ± 1.8	7.0 ± 2.6	2.6 ± 2.1	7.6 ± 2.4	7.1 ± 2.7	2.5 ± 1.9	7.6 ± 2.4
5	5.4 ± 2.9	6.8 ± 2.4	10.5 ± 3.8	6.5 ± 2.7	14.1 ± 2.7	9.1 ± 3.6	7.9 ± 3.2	14.1 ± 2.7
10	6.3 ± 2.1	8.5 ± 2.4	18.5 ± 4.1	12.5 ± 2.9	35.8 ± 3.3	16.3 ± 4.2	14.8 ± 2.9	35.8 ± 3.3

Table 4.10: Mean and standard deviation of the number of defects formed per simulation for an O PKA at energies of 2 keV (total of 8 simulations) and 5 keV (total of 8 simulations).

PKA energy (keV)	Antisites		Interstitials			Vacancies		
	Mg'_{Al}	$Al^{\cdot}_{Mg}$	$Mg^{\cdot\cdot}_{i}$	$Al^{\cdot\cdot\cdot}_{i}$	O''_{i}	V''_{Mg}	V'''_{Al}	$V_O^{\cdot\cdot}$
2	1.6 ± 1.7	2.0 ± 2.0	3.1 ± 2.0	3.4 ± 2.4	7.3 ± 2.5	2.8 ± 1.8	3.8 ± 2.5	7.3 ± 2.5
5	5.1 ± 3.0	7.1 ± 3.1	9.3 ± 4.1	5.8 ± 4.7	20.1 ± 4.9	7.5 ± 3.7	7.8 ± 4.9	20.1 ± 4.9

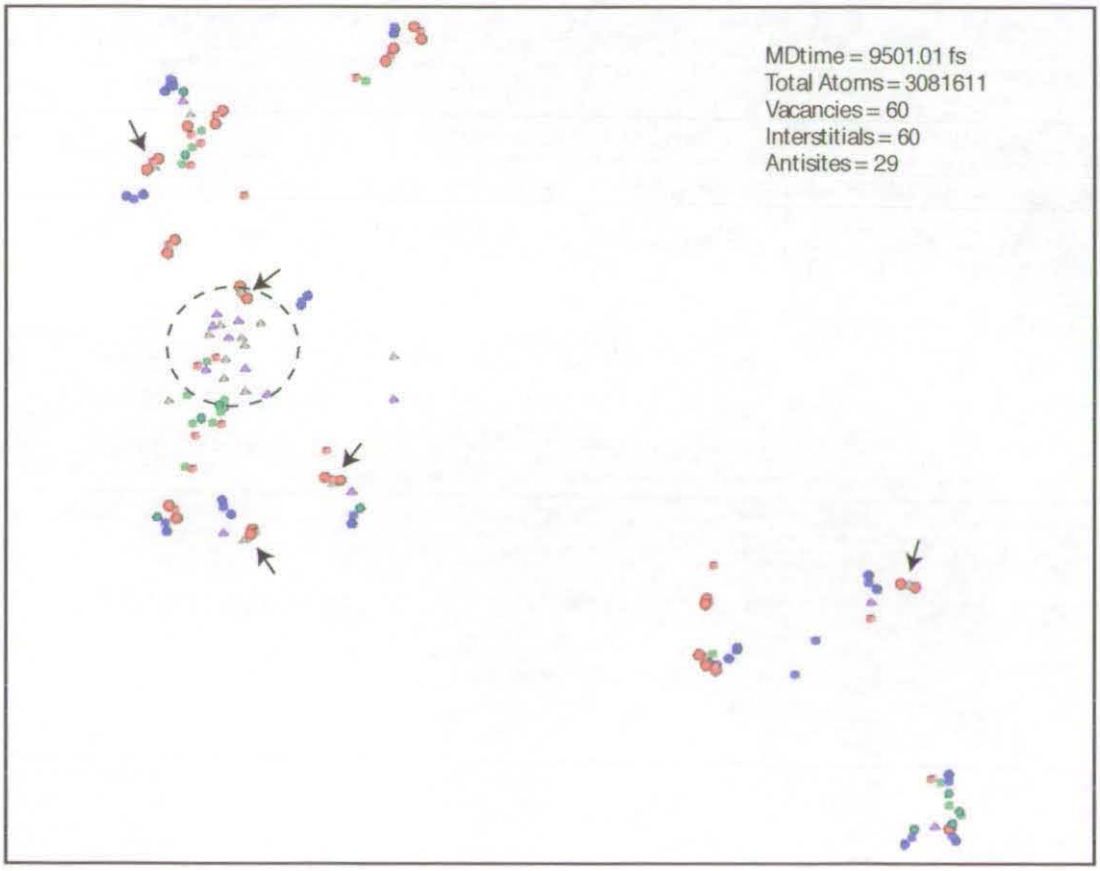

Figure 4.22: Residual defects generated by a 10 keV Mg PKA directed along [2 3 2] in a cubic simulation cell of length 310 Å. This was the largest cell employed containing more than 3 million atoms. The arrows indicate $Al^{\cdot}_{Mg}$ pinning an O''_i–$V_O^{\cdot\cdot}$–O''_i split interstitial. A core of antisites is shown by the dashed circle.

to displace anions than cations and that the resulting interstitials settled as split interstitial defects aligned along ⟨110⟩. Cation split interstitials occurred only around a magnesium vacant site with the two interstitials occupying structural octahedral vacancies as shown in fig. 4.10. Our results also show that irradiation produces a number of cation antisite defects as observed in experiments. It was found that Al ions can occupy tetrahedral sites in the spinel structure by forming split vacancy and ring defects. The high energy cascades resulted in similar defect structures as the lower energy cascades due to subcascade branching.

Further analysis of the distribution of defects in $MgAl_2O_4$ will be discussed and compared in the next chapter whereby the role of cation inversion on the process of defect formation will be investigated. In order to investigate the diffusion mechanisms and associated energy barriers for defect motion, temperature accelerated dynamics was employed to evolve over longer time scales the point defects obtained from the cascade simulations. This will be discussed in chapter 6.

Chapter 5

Effects of cation disordering on defect formation in spinels

5.1 Introduction

In this chapter, the role of cation disordering on the process of defect formation by irradiation in the spinel structure is determined using molecular dynamics simulations. This is achieved by comparing the results for the normal spinel $MgAl_2O_4$ with two other spinels which have a larger amount of naturally occurring inversion. These are magnesium gallate $Mg^{2+}Ga_2^{3+}O_4^{2-}$ and magnesium indate $Mg^{2+}In_2^{3+}O_4^{2-}$ spinels. The lattice structures of $MgGa_2O_4$ and $MgIn_2O_4$ are similar to that of $MgAl_2O_4$ but with different cation arrangements characterised by their inversion parameter, i. The inversion parameters are assumed to be 0.5 for the gallate spinel (half-inverse spinel) and 1 for the indate spinel (inverse spinel). These values are close to the cation distribution in real materials: $MgIn_2O_4$ occurs naturally as an inverse spinel with $i = 1$, whereas $MgGa_2O_4$ is a disordered spinel with $i = 0.67$ [43]. The purpose of selecting spinels with different degrees of disorder is to understand how the presence of cation disorder might affect the radiation tolerance of the material. In other words, how radiation tolerant is a normal spinel as compared to a spinel with an inherent amount

cation disorder. The energetics of the three oxides under irradiation is therefore dependent on both the corresponding disorder and the chemical effects of having different ternary cations (either Al^{3+}, Ga^{3+} or In^{3+}) in the spinel structure.

In the first section of this chapter, the methodology employed in generating the corresponding inversion in $MgGa_2O_4$ and $MgIn_2O_4$ spinels is discussed. Once the half-inverse $MgGa_2O_4$ and fully inverse $MgIn_2O_4$ structures have been setup, collision cascades in the energy regime of 0.4-10 keV are investigated in these spinels using the same methodology as described in section 4.4. In each case, the various types of defect structures and their spatial distribution within the material are analysed. Finally, the damage imparted as a function of cation disorder is analysed and compared for the normal magnesium aluminate spinel, the half-inverse magnesium gallate spinel and the fully inverse magnesium indate spinel.

5.2 Generating cation disorder in spinels

The normal spinel structure is characterised by zero inversion such that all Mg^{2+} ions occupy tetrahedral sites and all Al^{3+} occupy octahedral sites. For any normal spinel, the coordinate system provided in table 2.1 can be used to set up the lattice structure. However, because of the inversion in the gallate and indate spinels, the 2+ and 3+ cations have to be randomised over both octahedral and tetrahedral sites in order to account for the corresponding inversion. This is done by using a combination of Monte-Carlo and energy minimisation techniques [76]. Starting with a normal $MgGa_2O_4$ spinel structure with configuration I_0, the aim is to obtain a distribution of Mg and Ga ions that would reflect an inversion of 0.5. The method proceeds by iteratively interchanging a Mg ion with a Ga ion, and minimising the energy of this new configuration, I_1. At the end of the minimisation procedure, the difference in the total potential energy of systems I_0 and I_1 is calculated. In order to accept the new configuration, the energy difference has to be negative, or, it has to satisfy a certain

probability based on the Metropolis scheme [34]. Otherwise the move is rejected. The process is repeated until the corresponding inversion is obtained in the half inverse and fully inverse spinels. The computational time required for this procedure was prohibitive for systems involving more than a few hundreds of atoms.

By using the combined Monte-Carlo and energy minimisation technique described above, a number of possible cation distributions was generated within a representative 2x1x1 112 atom supercell with periodic boundary conditions for both the gallate and indate spinels at the required inversion. The lattice energies of the various 2x1x1 distributions were compared and the one with the lowest energy selected.For the cascade simulations, the lattice was generated by replicating this unit cell in space. The periodic boundary conditions used in the creation of the supercells ensured that no unrealistic energies occurred from this replication process.

The lattice parameter resulting for our model for the half-inverse gallate spinel was 8.31 Å while for a normal gallate spinel, the potential predicts a lattice parameter of 8.35 Å. For the inverse indate spinel, the lattice parameter was 8.85 Å as compared to 9.01 Å for the normal indate spinel. In both cases, the normal spinel lattice had a lower energy than for the case where inversion was included. In the half inverse spinel, the resulting distribution is such that half of the Mg ions initially at tetrahedral sites, have swapped sites with the Ga ions. In the fully inverse $MgIn_2O_4$ spinel, all Mg ions are randomised on the octahedral sublattice, whereas half of the In ions are at tetrahedral sites. The cation distribution in a 56 atoms unit cell of the inverse spinels are shown in table 5.1 and can be compared with that of the normal spinel, $MgAl_2O_4$.

Table 5.1: Distribution of cations in a unit cell of $MgAl_2O_4$ ($i = 0$), $MgGa_2O_4$ ($i = 0.5$), and $MgIn_2O_4$ ($i = 1$).

Site type	Total	$MgAl_2O_4$		$MgGa_2O_4$		$MgIn_2O_4$	
		Mg	Al	Mg	Ga	Mg	In
Tetrahedral	64	8	0	4	4	0	8
Octahedral	32	0	16	4	12	8	8

In the normal spinel we refer to an antisite defect as an Mg ion on an Al site or vice-versa. In the inverse and half-inverse spinels we refer to a change of cation species between the initial and final lattice arrangements as a cation disorder (CD) defect because their initial structures already contain disorder. However, an antisite defect in the fully inverse $MgIn_2O_4$ crystal refers to a Mg ion sitting at a tetrahedral In site. The same notation employed in chapter 4 is used to classify defects in the gallate and indate spinels whereby interstitials are denoted by spheres and vacancies as cubes. Cones represent CD defects, whereas antisites in the inverse spinel are shown as bright blue spheres. Interstitials and vacancies of the ternary cation B^{3+} (B = Al, Ga, In) are always shown green. For the half-inverse and inverse spinels, the defect geometry varies more with the local environment as compared to the normal spinel. Thus, a detailed description of the defect geometry is not provided here in contrast the normal spinel.

5.3 Collision cascades in the half-inverse spinel

5.3.1 0.4 keV simulations

The typical cascade formation and defect annihilation in the half-inverse spinel at the low energy of 0.4 keV initiated by a Ga PKA is shown in fig. 5.1. After 541 fs, anion split interstitials defects labelled A and B were seen to move one-dimensionally along the <110> anion rows. The defect B recombines with a $V_O^{\cdot\cdot}$ initially 7.6 Å away, whereas defect A remains in the structure becoming A′ after 5 ps. The movement of cations on the cation sublattice is illustrated by the cation defect chain labelled C, consisting of 3 alternate interstitials and 2 vacancies, which relaxed to form 2 cation disorder (CD) defects and 1 $Mg_i^{\cdot\cdot}$–V''_{Mg}–$Ga_i^{\cdot\cdot\cdot}$. In the normal spinel, cation split interstitials are observed to be centred about a tetrahedral vacancy. These sites are equally occupied by both Ga and Mg ions in the half-inverse spinel, where the cation

split interstitials were observed to be centred about.

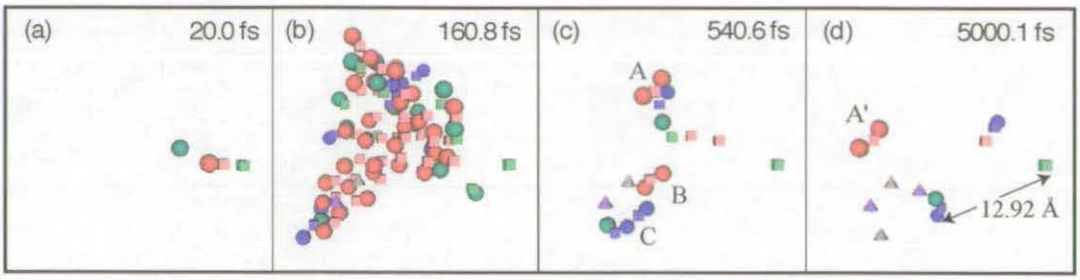

Figure 5.1: Snapshots of a 0.4 keV cascade simulation initiated by a Ga along ⟨123⟩ in the half-inverse spinel. Spheres represent interstitials and cubes denote vacancies. The red colour refers to O^{2-} defects, blue is for Mg^{2+} defects while Ga^{3+} defects are coloured green. Cation mixing is illustrated as purple and grey cones for Mg'_{Ga} and $Ga^{\cdot}_{Mg}$ defects respectively. The peak damage occurred approx. 161 fs after the cascade was initiated.

Along other PKA directions, a wider variety of defect structures was apparent as compared to the normal spinel, even at such low energies. For the Mg PKAs, the common defects consisted of O, Mg, Ga and mixed Mg–Ga split interstitials centred about either a tetrahedral Mg vacancy or a tetrahedral Ga vacancy. These defects can be depicted in figs. 5.2 (a) and (d) alongside a few cation disorder defects and vacancies. Unlike in the normal spinel where anion PKAs could not cause permanent damage to the cation sublattice in this energy regime, in the half-inverse $MgGa_2O_4$ these caused displacements on the cation sublattice as shown in fig. 5.2 (b) and (e). Figs. 5.2 (c) and (f) illustrate the damage imparted to the gallate spinel by 0.4 keV Ga PKAs along two distinct directions. A ring structure labelled D, made up of Mg and Ga vacancies and interstitials, can clearly be identified in each figure. These structures were also observed in the normal spinel but at higher energies, whereby the 3 interstitials were trapped at tetrahedral sites.

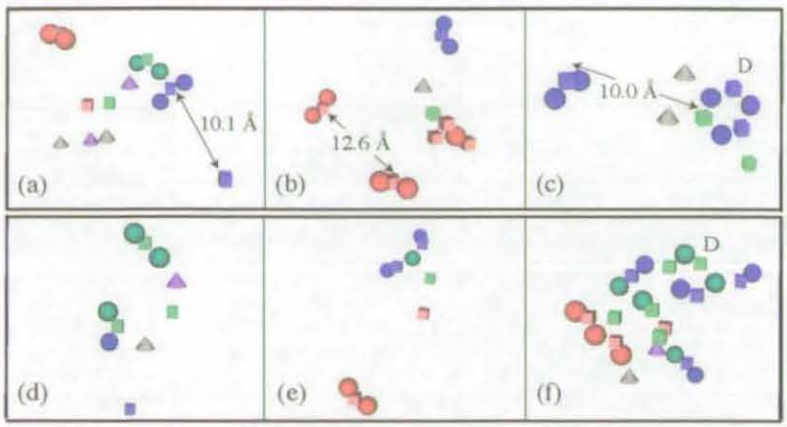

Figure 5.2: Resulting defect structures after 5 ps for the knock-on energy of 0.4 keV in the gallate spinel. (a) Mg^{2+} PKA along [1 2 3] resulting in the formation of pure O, Ga, and Mg split interstitials, one Ga–O vacancy pair and CD defects; (b) O^{2-} PKA along [1 7 5]; (c) Ga^{3+} PKA along [2 1 0] forming a distinct 'ring' structure labelled D; (d) Mg^{2+} PKA along [7 5 1]; (e) O^{2-} PKA along [2 3 2] creating a cation crowdion; (f) Ga^{3+} PKA along [1 7 3].

5.3.2 2 – 10 keV simulations

As the kinetic energy of the primary knock-on atom is increased, the complexity of the defects around the cascade cores for certain trajectories also increased. Fig. 5.3 shows the damage imparted to the half-inverse gallate spinel at the energy of 2 keV for 3 different simulations initiated by a Ga PKA. The picture in fig. 5.3 (a) shows the least damage produced by a Ga PKA at this energy and is the result of channelling of the tetrahedrally coordinated PKA along the [1 0 0] trajectory. Fig. 5.3 (b) is an example of a simulation where an average amount of damage is produced by a 2 keV Ga PKA where cation interstitial-vacancy crowdion chains are apparent. The damage in fig. 5.3 (c) is the maximum over the whole set generated by a Ga PKA at 2 keV. Here, a dense cascade core is obtained, due to small displacements of cations offset from their perfect sites, causing some local rearrangement of oxygen atoms.

The damage morphology shown in figs. 5.4 and 5.5 at 5 keV and 10 keV respectively, indicate a very similar trend as the low 0.4 keV and 2 keV cascades whereby much disordering on the cation sublattice can be seen as compared to the normal

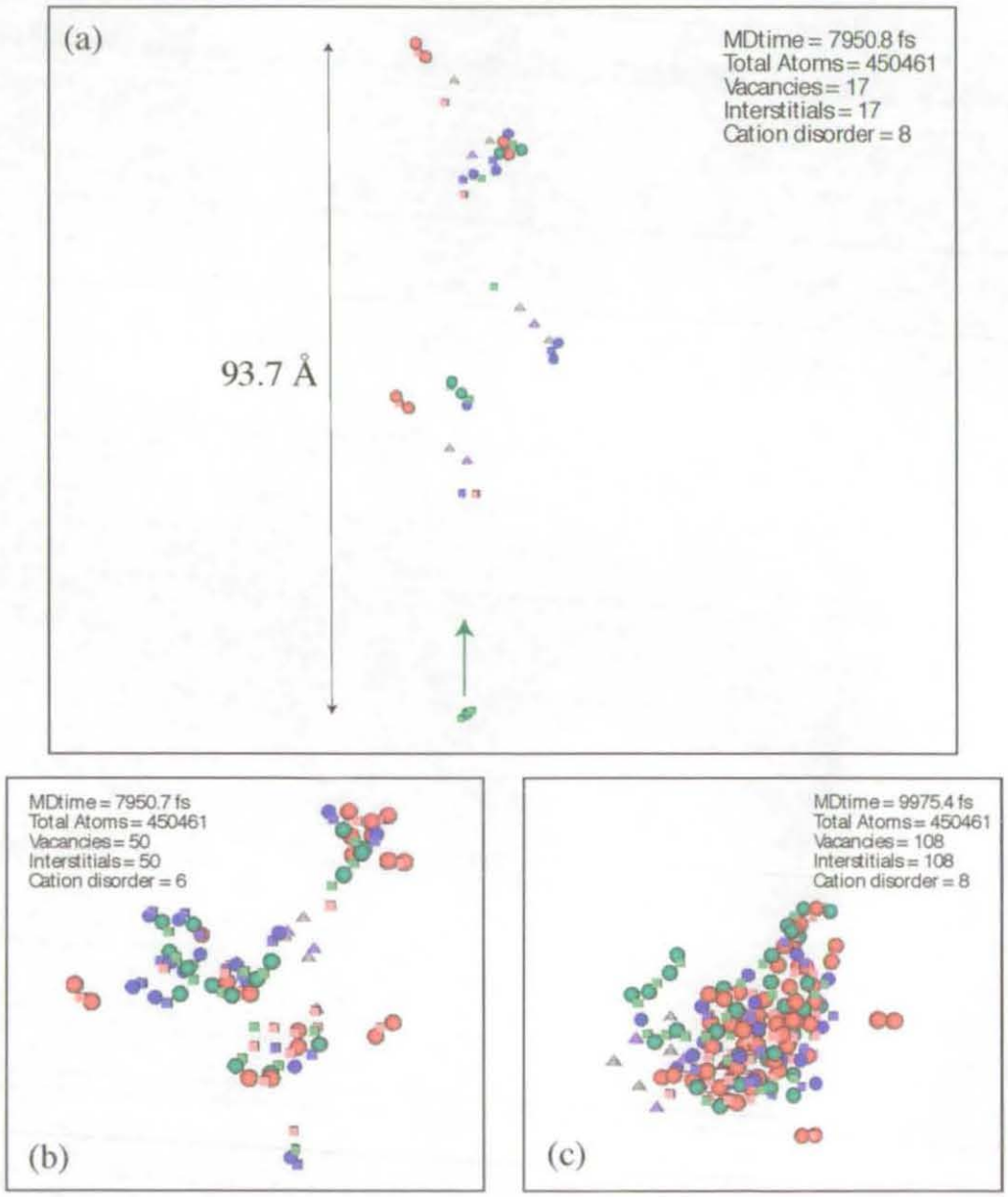

Figure 5.3: Damage distribution at 2 keV for Ga PKAs in the half-inverse spinel along the following trajectories: (a) [1 0 0] from a tetrahedral site with the channelling direction shown by the green arrow, (b) [1 0 0] from an octahedral site, (c) [1 -1 1] from a tetrahedral site.

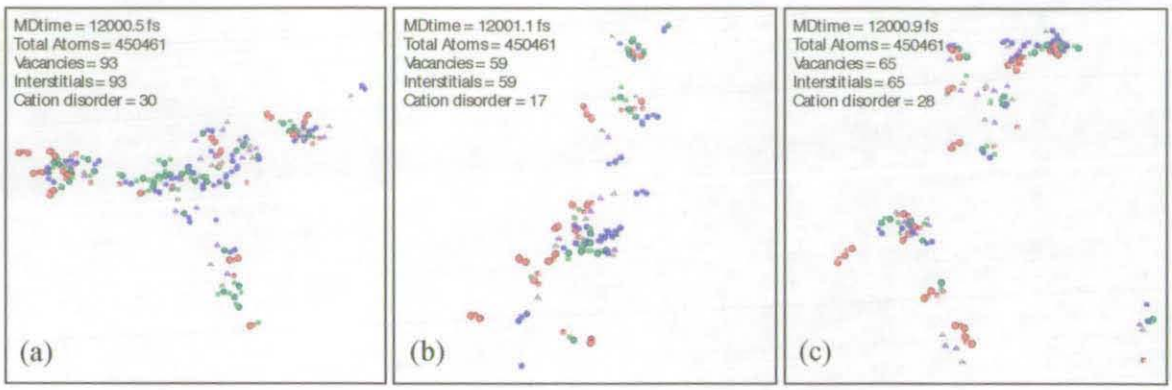

Figure 5.4: Defect distribution at 5 keV for a Ga PKA directed along [8 5 12] (a), a Mg PKA initiated along [6 14 5] (b) and an O PKA with trajectory [11 7 4] (c) in the half-inverse spinel.

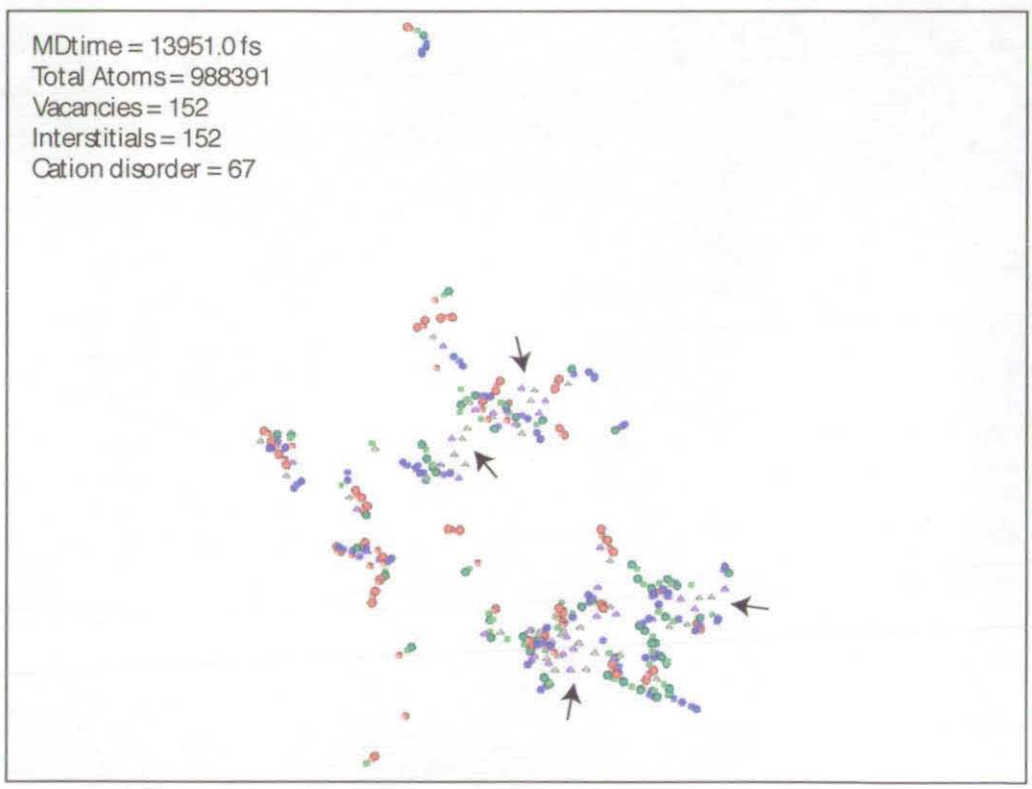

Figure 5.5: Damage formed in the half-inverse spinel crystal at the energy of 10 keV initiated by a Ga PKA along [15 7 12]. The arrows indicate regions of high concentration of cation disorder defects.

spinel where the defects are more isolated. In all the cascades studied, a significant proportion of cation interstitials are trapped at structural vacancies in the lattice, in between the actual vacancies. The arrows in fig. 5.5 show regions which contain a large number of cation disorder (CD) defects.

5.4 Collision cascades in the inverse spinel

5.4.1 0.4 keV simulations

In order to investigate the effects of radiation in a spinel with the fully inverse structure, collision cascades were setup in $MgIn_2O_4$ in the energy range of 0.4-10 keV. Fig. 5.6 illustrates a typical cascade evolution and the surviving defects generated by a 0.4 keV In PKA. The anion interstitials relaxed into a crowdion defect labelled E, which oscillated one-dimensionally along <110> at the end of the collisional phase of the cascade. The anion vacancy, F, created some local distortion pushing the first nearest neighbour tetrahedral In ion off its perfect lattice position. In analogy to the normal $MgAl_2O_4$ spinel where cation split interstitials were centred about a tetrahedral Mg vacancy, the same defect structures in the inverse spinel were also centred about the tetrahedral cation vacancy, with the interstitials occupying the neighbouring structural octahedral vacancies (an example is the defect G in fig. 5.6 (d)).

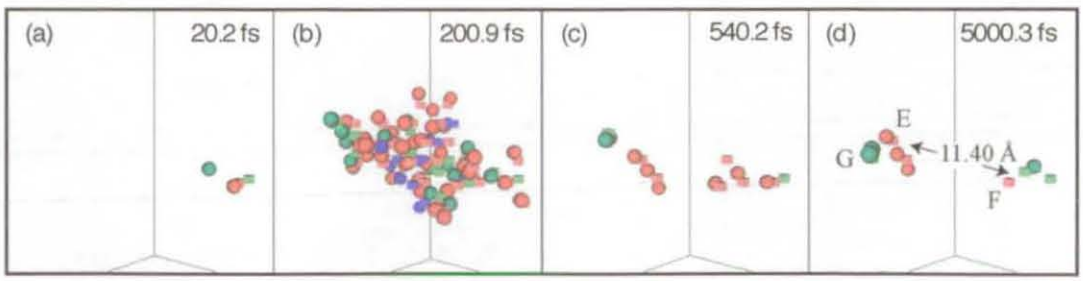

Figure 5.6: Snapshots of a 0.4 keV cascade simulation initiated by a In along ⟨123⟩ in the the inverse spinel. Spheres represent interstitials and cubes denote vacancies. The red colour refers to O^{2-} defects, blue is for Mg^{2+} defects while In^{3+} defects are coloured green.

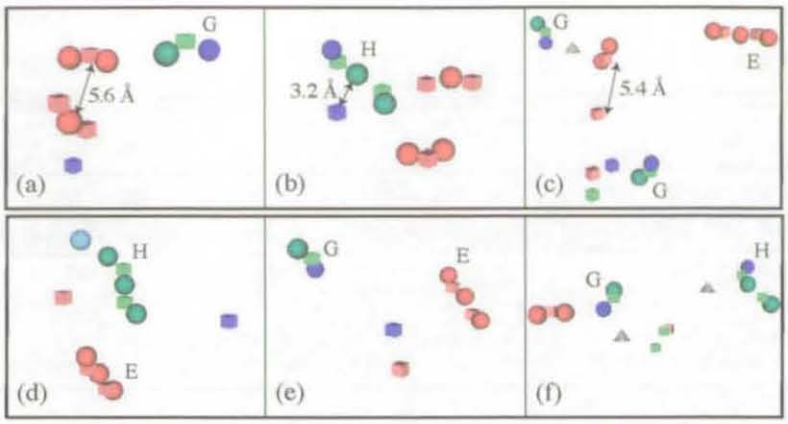

Figure 5.7: Residual defects generated by 400 eV cascades in the inverse indate spinel. (a) Mg^{2+} PKA along [2 1 0]; (b) O^{2-} PKA along [1 2 3]; (c) In^{3+} PKA along [7 3 1]; (d) Mg^{2+} PKA along [1 7 3]; (e) O^{2-} PKA along [2 3 2]; (f) In^{3+} PKA along [2 3 2]. Cones represent CD defects (purple - Mg'_{In}; grey - $In^{\cdot}_{Mg}$ on the octahedral sublattice). The bright blue sphere in (d) denotes a Mg'_{In} antisite (on the tetrahedral sublattice).

The defects in fig. 5.7 for six different simulations show that in the inverse spinel, all cation split interstitials and crowdions are centred around a tetrahedral In vacancy. These are labelled G and H respectively. The results therefore indicate that irrespective of the spinel type and the degree of inversion in the structure, cation interstitials prefer to be centred about a tetrahedral vacancy site, forming either split interstitials or crowdions. Crowdion structures were also observed on the anion sublattice and were seen to oscillate forth and back one-dimensionally, but did not diffuse over long distances (these are labelled E in fig. 5.7). The cascade collisions resulted also in a few antisite defects, which is a Mg'_{In} defect, where the magnesium atom replaces an indium atom originally occupying a tetrahedral site (one example can be found in fig. 5.7 (d)).

5.4.2 2 – 10 keV simulations

As the energy of the initial knock on event was increased, the same defect structures obtained at the low 0.4 keV cascades were observed at the higher energies. Cascades in the inverse spinel were distinct from the normal and half-inverse spinels because

the resulting damage was made up of mainly anion crowdion defects and indium crowdion defects. Those defects are apparent in figs. 5.8, 5.9 and 5.10 which show the damage imparted to the lattice at energies of 2 keV, 5 keV and 10 keV respectively. However, along certain directions, networks of cation interstitials and vacancies could be identified in the core of the cascade.

There were some differences in the cascade morphology due to the choice of In and Mg PKAs at the energy of 10 keV. Mg PKAs resulted in more subcascade branching and defect spreading as in the normal spinel, whereas In PKAs produced dense cascade cores which took longer to annihilate. However, the types of defects were similar to those seen at the 2 keV and 5 keV energies irrespective of the PKA type.

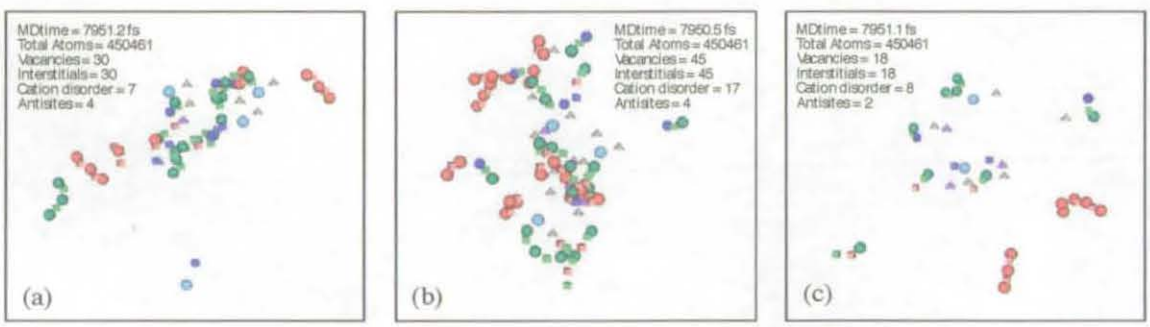

Figure 5.8: Damage distribution at 2 keV for In PKAs in the inverse magnesium indate spinel along the following trajectories: (a) [1 0 0] from a tetrahedral site, (b) [1 0 0] from an octahedral site, (c) [1 1 1] from an octahedral site.

5.5 Comparison of damage in the three spinels

The final damage shown in figs. 5.11 and 5.12 result respectively from 2 keV and 5 keV cascades in the normal magnesium aluminate, the half-inverse magnesium gallate, and the fully inverse magnesium indate spinels and are typical for these materials. The figures compare the spatial distribution of defects in the three compounds as a function of cation disorder. The defects in the normal spinel are more isolated than in the other two compounds. Selected regions, A in fig. 5.11 (b) and R in fig. 5.12

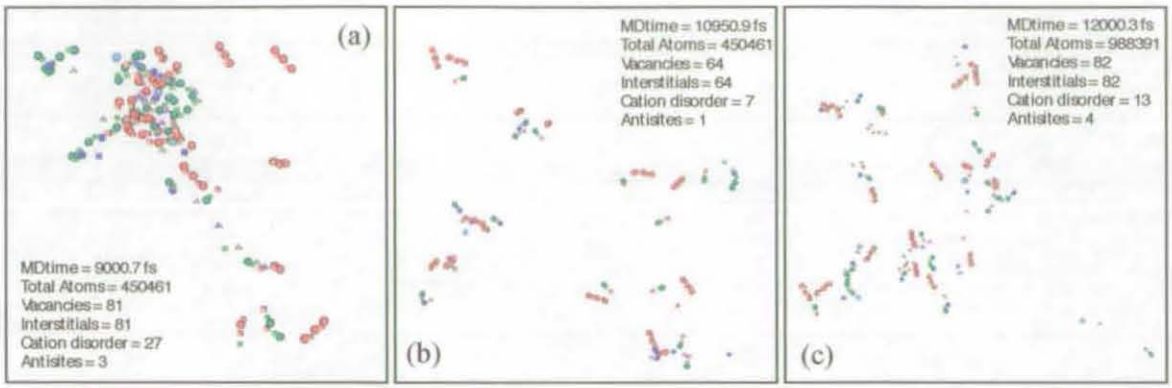

Figure 5.9: Defect distribution at 5 keV for a In PKA directed along [5 1 1] (a), a Mg PKA initiated along [1 9 5] (b) and an O PKA with trajectory [3 7 1] (c) in the inverse spinel.

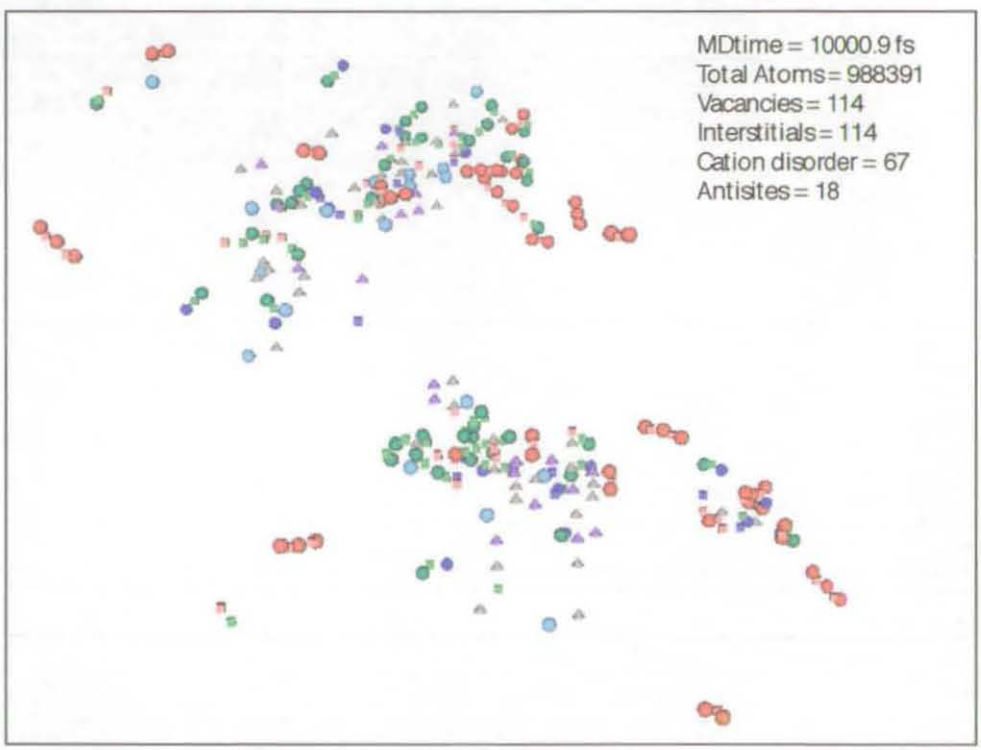

Figure 5.10: Damage formed in the inverse spinel at the energy of 10 keV initiated by a In PKA along [3 4 7].

(b), depict a considerable amount of rearrangement on the cation sublattice in the half-inverse spinel. The defect in region A is made up of 6 cation interstitials and 4 vacancies in a loop structure. The region defined by the label R in the half-inverse spinel contains one oxygen antisite defect O_{Ga}, which under normal conditions would be an energetically unfavourable defect. However, in this case, the anion antisite defect is surrounded by 3 Ga interstitials, offset from their normal lattice sites, which partially balance the charge. Figs. 5.11 (c) and 5.12 (c) for the inverse spinel contain mainly cation and anion crowdions labelled B and C respectively.

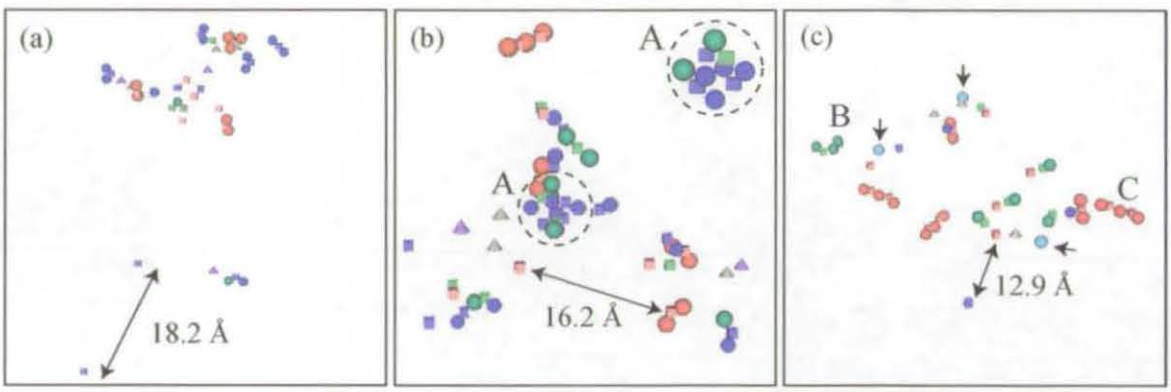

Figure 5.11: Comparison of damage created at 2 keV by Mg PKAs in spinels with varying inversion. (a) Normal magnesium aluminate and [2 1 0] direction, (b) Half-inverse magnesium gallate and [7 8 9] direction - region A is enlarged on the top right corner; (c) Inverse magnesium indate and [1 3 5] direction - the arrows indicate antisites.

Fig. 5.13 shows the peak damage and the remaining defects at the end of 5 keV cascades in the three compounds. The crystalline ordering around the cation interstitials reveal distinct characteristics in each of the three spinels. Selected regions of interest around cation interstitials are taken from the 5 keV cascades in fig. 5.13 and are plotted with their nearest oxygen neighbours also shown in fig. 5.14. In fig. 5.14 (a) for the normal spinel, typical cation split interstitials aligned along <110> are obtained. The same types of defects were seen in the half-inverse spinel, but these are connected to regions whereby cation interstitials move to tetrahedral sites (see

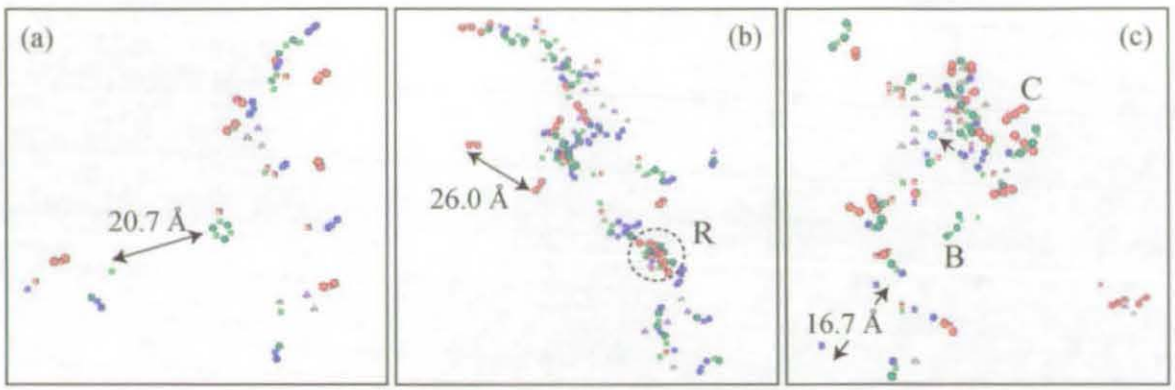

Figure 5.12: Comparison of defects obtained from 5 keV cascades initiated by Mg PKAs in spinels with varying disorder. (a) Normal magnesium aluminate and [1 5 7] direction, (b) Half-inverse magnesium gallate and [5 1 2] direction; (c) Inverse magnesium indate and [1 2 3] direction.

encircled regions in fig. 5.14 (b)), reforming locally the spinel structure but offset from the original half-inverse system. Fig. 5.14 (c) depicts regions in the inverse spinel where the cascade has caused a depletion of cations from their tetrahedral sites. The interesting feature about these defects is that, three of the four empty 16c octahedral sites around each vacancy are now occupied by cation interstitials. In the normal spinel, the split interstitials in fig. 5.14 (a) occupy only 2 of the four empty octahedral sites. This implies a slightly different and more complete post-cascade disordered rocksalt structure transformation in the inverse spinel compared to the normal spinel.

The evolution of the number of interstitials with time for a 5 keV B^{3+} PKA (B = Al, Ga or In) in the three materials is shown in fig. 5.15. These show that the peak damage increases and occurs at longer times as we go from the normal Al spinel to the half-inverse Ga spinel and the inverse In spinel. The immediate post-cascade annealing process also takes longer. The trend shown in these figures are typical of all cascades initiated by ternary cations in these materials.

The defect production by 10 keV cascades in all three materials is shown in fig. 5.16. The least damage was observed in the normal spinel where isolated defects were

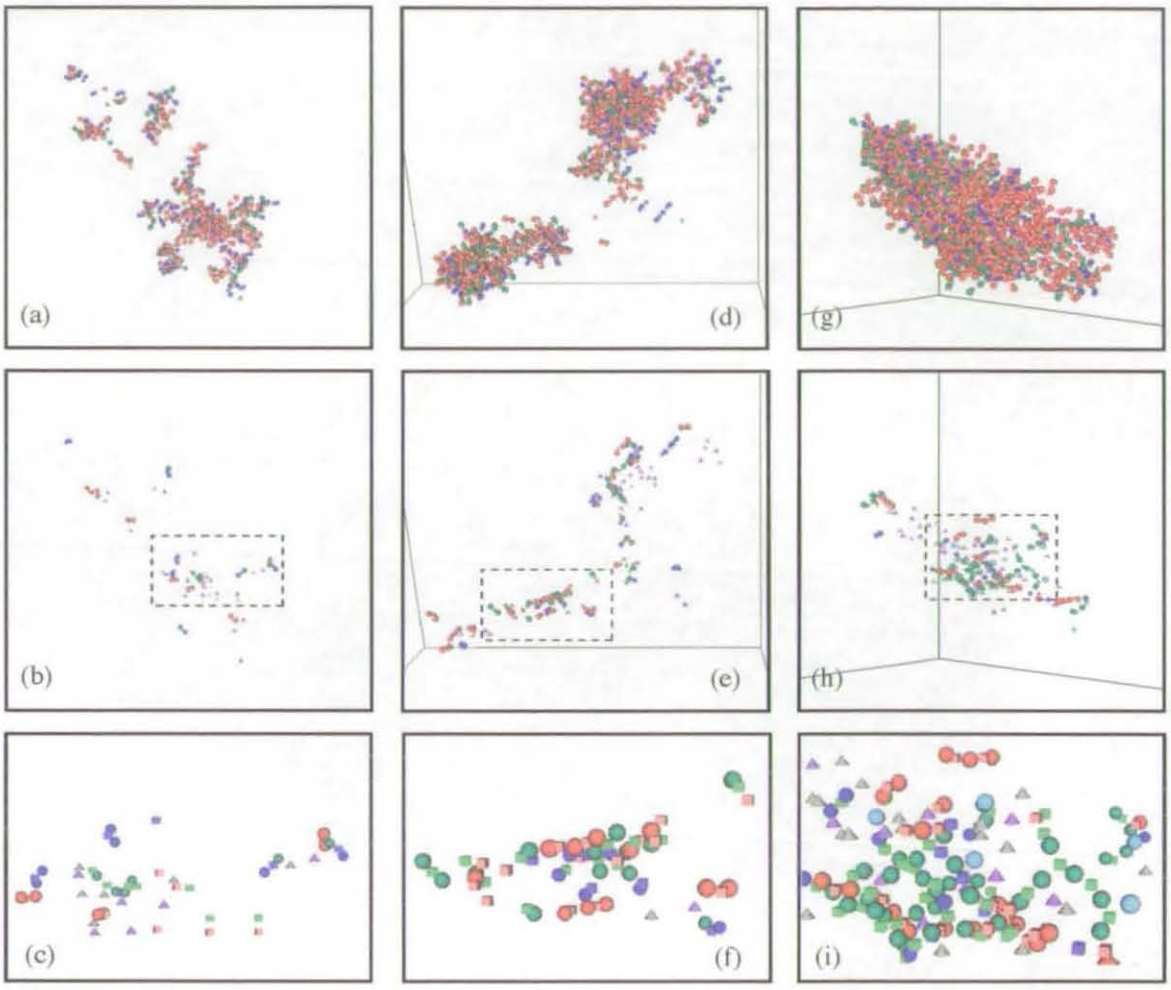

Figure 5.13: Cascades generated by a 5 keV PKA in the three spinels showing the displacement of ions when there is peak damage and also at the end of the collisional phase of the cascade. (a) 150 fs, (b) and (c) 9975 fs, normal $MgAl_2O_4$ spinel and Al PKA; (d) 250 fs, (e) and (f) 7250 fs, half-inverse $MgGa_2O_4$ spinel and Ga PKA; (g) 400 fs, (h) and (i) 9001 fs, fully inverse spinel, $MgIn_2O_4$ and In PKA. (c), (f) and (i) are zoom-ins of the core of the cascades.

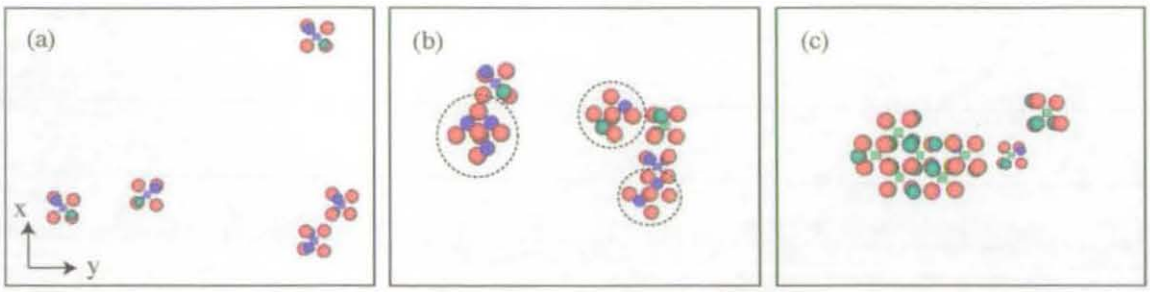

Figure 5.14: Differences in the crystalline ordering around cation interstitials taken from regions of the 5 keV cascades in fig. 5.13. The red spheres denote oxygen atoms at perfect sites, blue spheres refer to Mg interstitials, green spheres denote B interstitials (B = Al, Ga or In) and the cubes denote cation vacancies. (a) The cation split interstitials in $MgAl_2O_4$ are similar to those obtained at the low 0.4 keV cascades and are arranged as shown in fig. 4.10. (b) The regions encircled denote cation interstitials having tetrahedral coordination in the half-inverse $MgGa_2O_4$ spinel. (c) The green cubes denote tetrahedral vacancies in the inverse $MgIn_2O_4$ spinel - around each tetrahedral vacancy, 3 cation interstitials fill up 3 of the 4 empty 16c octahedral interstices.

obtained due to subcascade branching. Figs. 5.16 (b) and (c) represent the densest cascades in the half-inverse spinel and in the inverse spinel at 10 keV respectively. Damage in the half-inverse spinel was characterised by more interstitial-vacancy networks sometimes forming closed loops as shown in region (4) of fig. 5.16 (b) where cations are displaced from their initial sites to adjacent structural vacancy sites in the crystal. Fig. 5.16 (c) in the inverse spinel shows that cation and anion crowdions typically occur under irradiation at those energies which can sometimes form very close to each other (an example is shown in region (6) of fig. 5.16 (c)).

5.6 Post cascade defect distribution

In order to have a better insight of the defect distribution and proportion of cation and anion defects that remain in the irradiated structures, the average number and species of the interstitials (solid lines), vacancies (dashed lines) and cation disorder (CD) defects per simulation in the three spinels is shown in fig. 5.17 (a)–(c). These

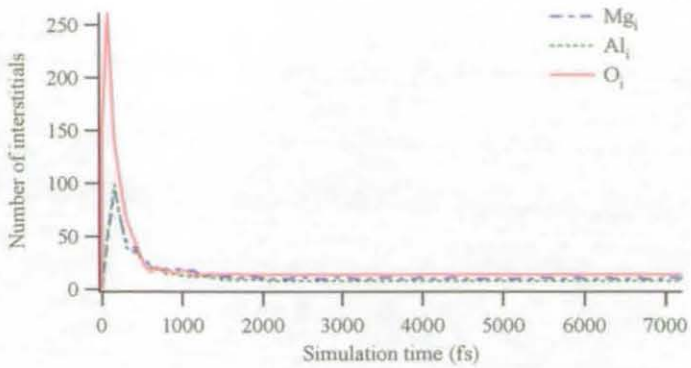

(i)

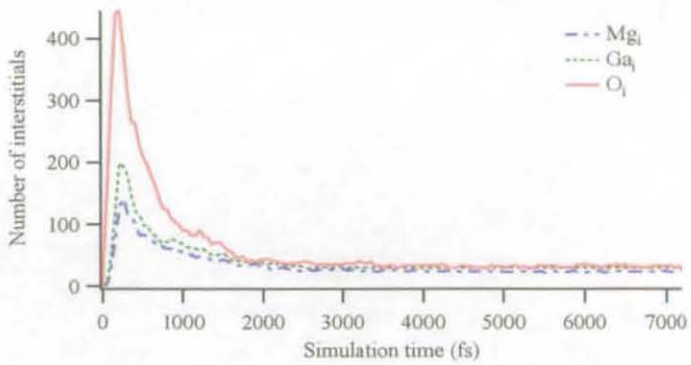

(ii)

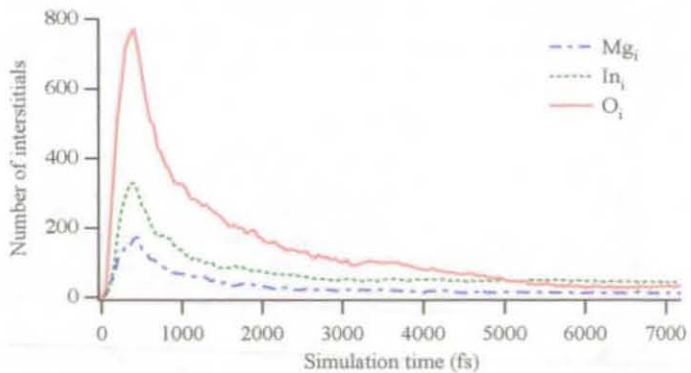

(iii)

Figure 5.15: Comparison of the defect evolution (number of interstitials) with time in the corresponding 5 keV cascades shown in fig. 5.13 in (i) $MgAl_2O_4$, (ii) $MgGa_2O_4$ and (iii) $MgIn_2O_4$. The peak damage and the recombination process takes longer in the inverse spinels where a dense cascade core is formed.

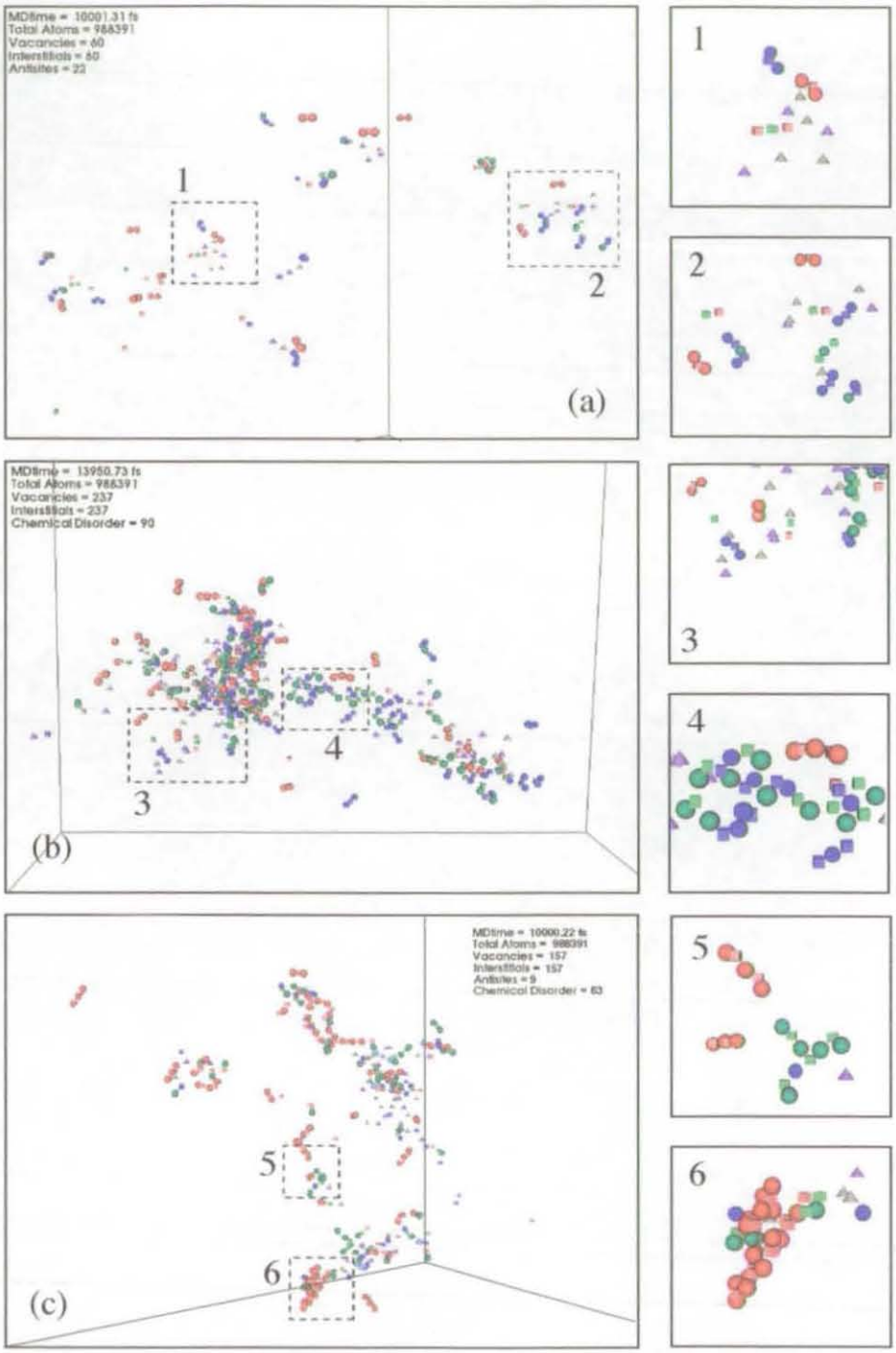

Figure 5.16: Defects remaining at the end of the collisional phase of a 10 keV cascade in (a) $MgAl_2O_4$ initiated by an Al PKA along [8 13 7]; (b) $MgGa_2O_4$ and Ga PKA along the [1 3 2] trajectory that caused the most damage over a set of 8 simulations; (c) $MgIn_2O_4$ and In PKA along [2 3 5] resulting in the most defects over a set of 8 simulations. The length of the cubic simulation cells were approximately 23 nm.

results must be treated with some caution since they are dependent on the precise definition of what forms a defect. For example the crowdion is counted as 3 interstitial defects and 2 vacancies whereas the split interstitial is counted as 2 interstitials and 1 vacancy. Notwithstanding this proviso, from this plot, magnesium aluminate spinel produced the least number of point defects as compared to the half and fully inverse spinels. For the normal and fully inverse spinels (as would be expected since there are more O ions) there are more displaced O ions than cations. This is in accordance with the threshold energy calculations which was found to be lowest for the anion sublattice in the normal spinel. There are slightly more displaced Mg ions than Al in normal spinel despite there being twice as many Al ions in the lattice than Mg. This situation is reversed in the fully inverse spinel due to the fact that in the first case tetrahedral sites are occupied by Mg^{2+} but in the second case these sites are filled by In^{3+}. It thus appears to be much easier to displace ions from tetrahedral sites than octahedral.

Figs. 5.17 (a)–(c) indicate differences in the number of cation interstitials and vacancies of the same species because of the formation of antisites/cation disorder defects in the spinels. The difference is most apparent in the normal spinel, showing that there are more Al vacancies than Al interstitials due to the formation of more Al_{Mg} antisites than Mg_{Al} antisites. The same plot in the half-inverse spinel reveals an almost identical number of cation vacancies and interstitials remaining in the irradiated structure and these are comparable with the number of anion defects and cation disorder defects. This is due to the fact that cations tend to be displaced from their lattice sites around O defects, not that more cations are formed by the ballistic displacement. In the normal and fully inverse spinels, the number of O interstitial defects is equal to the number of O vacancies (red curves in fig. 5.17), but not in the half-inverse spinel because of the formation of a small number of anion antisites in the disordered cascade core. The highest number of anion defects was recorded in inverse spinel due to a preference for the formation of crowdion defects rather than split

interstitials. The average number of total interstitial defects for the 10 keV cascades in $MgAl_2O_4$ was 62, 148 in $MgGa_2O_4$ and 129 in $MgIn_2O_4$, with standard deviations of 7, 40 and 16 respectively. This indicates a wider spread of damage range in the half-inverse spinel.

Cation disordering in all three compounds is the most common defect resulting from the dynamical cascades. These defects result from cations swapping from octahedrally to tetrahedrally coordinated sites or vice versa producing antisites in the normal spinel, but could also involve interchange of cations of different species over similar sites in the half-inverse and inverse spinels. The plot in fig. 5.17 (d)–(f) shows the average number of cation disorder defects per simulation distributed over tetrahedral and octahedral sites. In the normal spinel radiation creates antisites of the form Mg^{O}_{Al} and Al^{T}_{Mg}, where the superscripts O and T refer to the octahedral and tetrahedral sites. Fig. 5.17 (d) indicates a slightly higher number of Al antisites than Mg antisites created in the normal spinel at all three energies. This can be partly explained by the fact that during the cascade relaxation, the mixed split interstitial, $Mg^{\cdot\cdot}_{i}$–V''_{Mg}–$Al^{\cdot\cdot\cdot}_{i}$, could form an Al_{Mg} antisite and a pure $Mg^{\cdot\cdot}_{i}$–V''_{Mg}–$Mg^{\cdot\cdot}_{i}$ split interstitial which could then move locally on the tetrahedral Mg sublattice before stabilising. In the half-inverse $MgGa_2O_4$ spinel, radiation causes a redistribution of cations as shown in fig. 5.17 (e). This indicates that the Ga_{Mg} cation disorder defects are almost equally distributed on both the tetrahedral and octahedral Mg sites whereas the Mg_{Ga} defects prefer octahedral coordination over tetrahedral coordination. This implies that the half-inverse spinel (initially with an inversion of 0.5) can become more inverse as a result of irradiation. In the inverse spinel, Mg^{T}_{In} antisite defects were seen, which were not present in the original lattice. This induces a partial reversion from the inverse to the normal spinel structure. However, the plot in 5.17 (f) also shows more In^{O}_{Mg} and Mg^{O}_{In} cation disorder defects that remain in the structure than the antisites. These results show that every spinel accommodates a large amount of cation site interchange under irradiation which helps in maintaining

the crystalline structure.

In order to investigate the preferential segregation of cation interstitials to certain sites, we filter out those interstitials that are trapped at structural vacancies and regain coordination four (tetrahedral site) or six (octahedral site) with the anions. The figures shown in table 5.2 represent the distribution of cation interstitials at tetrahedral or octahedral structural vacancies for a given energy. It should be noted that the percentages do not add up exactly to 100 % because not all the interstitials are located at those structural vacancies but can be trapped between other defects. A similar approach is employed to investigate the nature of the cation vacancies left over at the end of the cascades and is presented in table 5.2. This information reveals the extent by which the octahedral and tetrahedral sites are depleted of their cations under irradiation.

Table 5.2: The percentage of cation interstitials occupying structural tetrahedral (*Tetra*) and octahedral (*Octa*) sites at the end of the collision cascades. The standard deviation is also included to show how this percentage is spread among the different trajectories for a specific PKA energy.

Spinel	2 keV		5 keV		10 keV	
	Tetra	*Octa*	*Tetra*	*Octa*	*Tetra*	*Octa*
$MgAl_2O_4$	23.9 ± 18.7	74.2 ± 18.7	21.6 ± 12.8	74.2 ± 13.9	19.9 ± 7.4	76.9 ± 7.5
$MgGa_2O_4$	35.8 ± 12.8	50.1 ± 16.6	33.2 ± 9.1	52.8 ± 7.9	33.2 ± 5.5	55.6 ± 7.0
$MgIn_2O_4$	17.7 ± 9.9	62.2 ± 15.9	17.6 ± 9.1	66.5 ± 9.7	17.4 ± 3.5	67.2 ± 8.9

Table 5.3: The percentage of tetrahedral (*Tetra*) and octahedral (*Octa*) cation vacancies remaining at the end of the cascade simulations.

Spinel	2 keV		5 keV		10 keV	
	Tetra	*Octa*	*Tetra*	*Octa*	*Tetra*	*Octa*
$MgAl_2O_4$	54.1 ± 20.8	45.9 ± 20.8	50.9 ± 9.7	49.1 ± 9.7	52.2 ± 6.3	47.8 ± 6.3
$MgGa_2O_4$	44.4 ± 7.6	55.6 ± 7.6	48.4 ± 6.9	51.6 ± 6.9	48.4 ± 2.9	51.6 ± 2.8
$MgIn_2O_4$	65.5 ± 8.7	34.5 ± 8.7	67.8 ± 8.4	32.2 ± 8.4	65.3 ± 5.4	34.7 ± 5.4

Table 5.2 shows a clear difference between the percentage of octahedral and tetrahedral interstitial site occupancies in the normal $MgAl_2O_4$ and inverse $MgIn_2O_4$

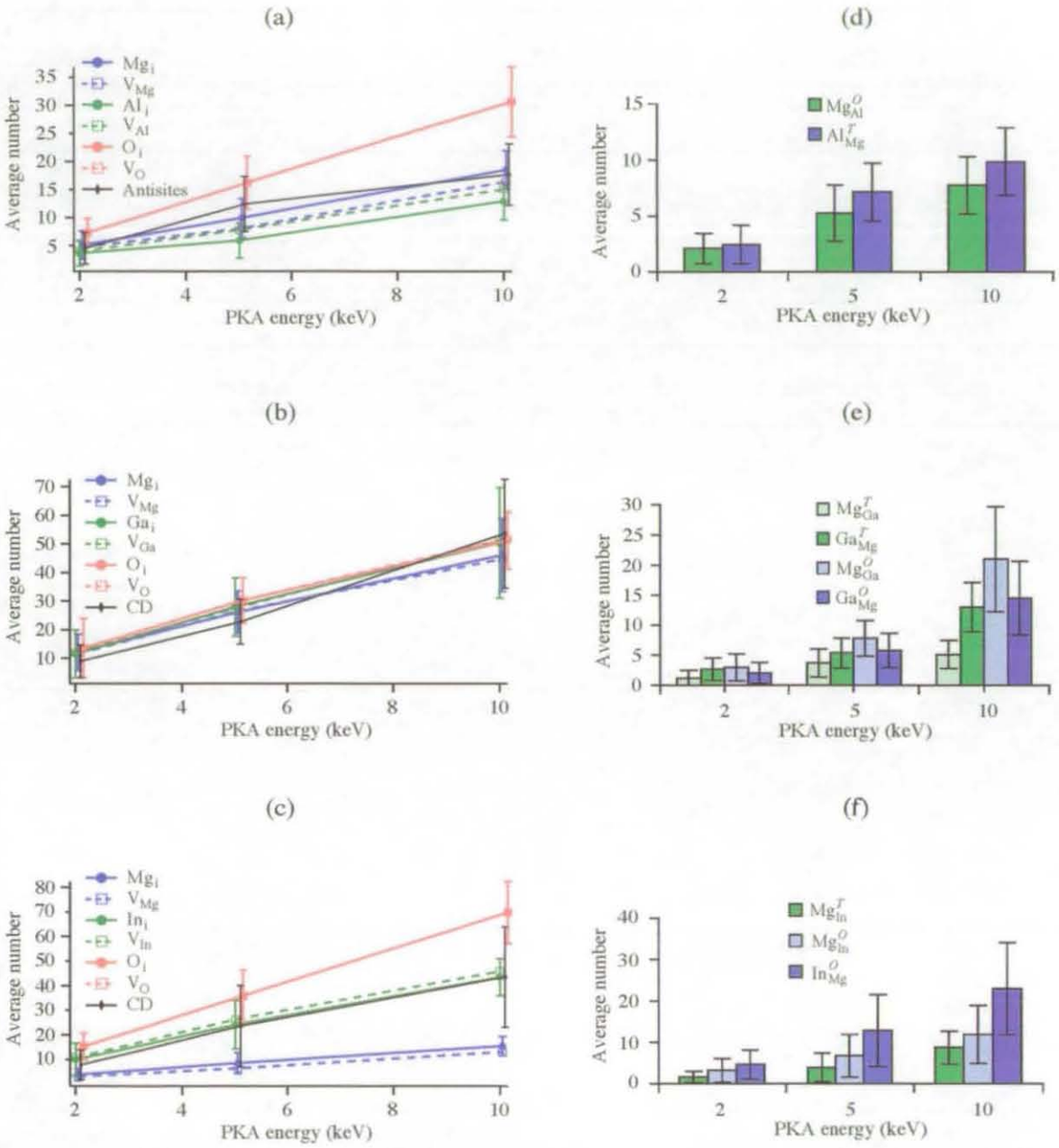

Figure 5.17: Average number of interstitials, vacancies and antisites/cation disorder (CD) defects created per simulation at energies of 2, 5 and 10 keV in (a) normal spinel, $MgAl_2O_4$, (b) half-inverse $MgGa_2O_4$ and (c) inverse spinel. Error bars are shown for interstitials and antisites/CD defects but not for vacancies which are similar to the interstitials. The average number and type of cation disorder defects and their coordination are shown in (d), (e) and (f). The superscripts T and O refer to tetrahedral and octahedral coordination respectively.

spinels with more octahedral sites being occupied at all three PKA energies. However, this is smallest for the intermediate $MgGa_2O_4$ spinel which has the highest tetrahedral site occupancies among the three spinels of 35.8 %, 33.2 % and 33.2 % for energies of 2, 5 and 10 keV respectively. Nevertheless, in all three spinels, the cation interstitials preferentially move to octahedral sites rather than tetrahedral sites under irradiation.

The vacancy distribution shown in table 5.3 indicates that in the normal spinel and in the semi-inverse gallate spinel, both the octahedral and tetrahedral cation sublattices are almost equally affected. However, in one unit cell of spinel, there are twice as many occupied cation octahedral sites (16) than tetrahedral sites (8) - one would expect more displaced octahedral ions (and hence more octahedral vacancies) than displaced tetrahedral ions - yet both sublattices are depleted by a similar amount. Therefore, it ought to be easier to displace tetrahedrally coordinated ions than octahedrally coordinated ions. This observation was also recorded under neutron irradiation during which diffraction patterns in the irradiated sample were reduced by 20 % for the tetrahedral sites but increased by 8 % for the octahedral sites [23]. This is more evident in the inverse $MgIn_2O_4$ spinel where more tetrahedral vacancies than octahedral vacancies remain in the structure coupled with an increased octahedral site occupancy (see table 5.2), at all three energies investigated. Therefore, the inverse spinel is more susceptible to undergo a rocksalt type transformation as compared to the normal and half-inverse spinels.

5.7 Discussions and conclusions

The defect production by irradiation in spinels with an inversion parameter of 0.5 and 1 was investigated by molecular dynamics simulations and compared to a normal spinel. In all three spinels, the normal $MgAl_2O_4$, the half-inverse $MgGa_2O_4$ and the fully inverse $MgIn_2O_4$ spinel, the onset of damage production resulted in simple defect structures consisting of split interstitials/crowdions and cation disorder defects. Over

the timescale of the collisional phase, a cation split interstitial could remain in the structure, diffuse on the tetrahedral sublattice to annihilate with a nearby vacancy in the structure, or form an immobile antisite/cation disorder defect. Oxygen split interstitials/crowdions were aligned along the <110> array of anions and could diffuse along that path with occasional orientation change to another <110> direction.

The higher energy cascades in normal spinel only produced distinct point defects characteristic of the low energy cascades due to subcascade branching. On the other hand, dense cascades in the half-inverse and fully inverse spinels created complex damage zones consisting of chains of interstitials and vacancies on the cation sublattice. In the half-inverse spinel, cation interstitials could occupy both tetrahedral and octahedral sites whereas cation defects in the inverse spinel were primarily In^{3+} defects. Cascades spread out more in the normal spinel compared to the inverse spinels and relaxation also occurred more quickly in the normal spinel.

The simulations showed that cation interstitials preferentially occupied octahedral sites irrespective of the spinel type. However, in the inverse spinel, the increased octahedral site occupancy was coupled with a depletion of ions on the tetrahedral In sublattice indicating that a faster structural transformation under radiation than in the normal spinel, with the half-inverse $MgGa_2O_4$ spinel showing the least propensity for this transformation. In the latter case, regions of the crystal could recrystallise among the point defects by forming cation chains of interstitials and vacancies with the interstitials residing at adjacent tetrahedral and octahedral vacancy sites.

The process of defect recombination in this particular group of spinels is dependent on at least three factors: first on the presence of cation disorder, secondly on the nature of the chemical bonding in the spinel and thirdly on the steepness of the repulsive wall between the trivalent cations and the O ions. Isolating these three factors is not trivial in this work. Based on structural considerations only, one would predict a better damage recovery in an isotropic crystal as compared to an anisotropic one. The random distribution of divalent and trivalent cations in the inverse spinels

contributes to changes in bond lengths locally in the crystal resulting to some degree of anisotropy. This affects the damage recovery process as compared to the normal spinel which resulted the least number of surviving defects at the end of the cascade simulations. The second factor is attributed to chemical effects arising from the increase in atomic number of the trivalent B^{3+} ions from Al^{3+} to Ga^{3+} to In^{3+}. It is known that the ability of a crystal structure to regain its crystalline ordering depends on the degree of ionicity or covalency of the material [77]. The hypothesis in Ref. [77] is that this is determined by the short-range term of the potential energy function. It was found that different damage recovery can be obtained depending on the steepness of the O-O interaction near equilibrium [78]. In our simulations, the short range O-O pair interaction is the same for all three spinels, whereas the B-O interaction changes according to the trivalent cation. The repulsive walls for the B-O interactions are shown in fig. 3.5 along with the forces near the equilibrium separation. The steepness of the potential curves is partially correlated with the remaining damage after the cascade in that the normal spinel, which has the least repulsive wall, shows the least damage. This is also a feature of cascades in metals where the cascade evolution and the resultant damage is highly dependent on the steepness of this curve in the region 1-100 eV [79, 80]. The steepness ordering is also the same near equilibrium where the forces are plotted in fig. 3.5 (b). Thus there is also qualitative agreement with the hypothesis of Ref. [77] which associates damage recovery with this near-equilibrium steepness. However it is difficult to quantify this as damage depends on so many other features of the model such as the initial degree of inversion, other parts of the potential interaction regime, the relative mass of the ions and especially the barriers for defect recombination.

Over the timescales studied, two diffusion mechanisms have been depicted in the normal spinel (1-D motion of the O split interstitial and the cation split interstitial moving on the tetrahedral sublattice). For the half-inverse and inverse spinels the crowdion/split interstitial defects oscillate locally but do not move long distances

after the ballistic phase is over. These preliminary results seem to indicate that defect recombination is easier in the normal spinel structure. The energy barriers for point defect diffusion and the associated mechanisms for motion are investigated in the next chapter.

Chapter 6

Temperature accelerated dynamics on point defects in spinels

6.1 Introduction

As exemplified in the two previous chapters, molecular dynamics is ideal to investigate the development and relaxation of a collision cascade on the time scale of several picoseconds. However, the response of a material to particle bombardment is determined not only by the number and nature of the residual defects created by the collision cascade, but also on the long-time evolution of those defects. Over time scales greater than ps, point defects can diffuse within the crystal structure and can either annihilate via harmless interstitial-vacancy recombination mechanisms, or, on the other hand, they can aggregate and form clusters of defects. These diffusion mechanisms are often characterised by a sequence of infrequent activated events that move the system from basin to basin on the potential energy hypersurface. The time gap between successive jumps can be of the order of millions of thermal vibrations depending on the height of the dividing surface between the basins and cannot be investigated by conventional MD simulations. In order to access longer time scales so that these dynamical but infrequent events can be investigated, accelerated dynamics

methods such as hyperdynamics, parallel-replica dynamics and temperature accelerated dynamics, have been devised. A review of each of these methods can be found in Refs. [81, 82].

The hyperdynamics method [83] is based on the formulation of a bias potential that raises the energy within the potential basins. This bias term has the effect of lowering the activation barrier for state to state transitions while preserving the relative probabilities for these transitions - thus the transitions occur at a faster rate. A boost factor in the time, dependent on the strength of the bias potential, is included at each integration step of the hyperdynamics simulations.

The parallel replica method [84] exploits parallelism to span the time scales of a dynamical simulation. The first step involves replicating the system of interest on M processors. On each processor, the replica undergoes a momentum randomisation stage so as to remove correlations between replicas. Each configuration is then evolved independently using normal MD such that the probability of escape from the current basin becomes M times more likely as compared to a single trajectory. Whenever a transition is detected on any processor, all processors are notified to stop. At this point, the simulation clock is advanced by the accumulated time over all the replicas. The system for which the transition was detected is then evolved for a predefined time during which new transitions can occur. This time is added to the total simulation time, and the process is repeated using the new configuration.

The temperature accelerated dynamics technique (TAD) [3] determines the state to state transitions of an infrequent event system by performing MD at a high temperature which can then be used to determine the dynamics at the lower temperature of interest. In a simplified approach, the TAD method can be viewed as one that uses high temperature MD to determine a single diffusion event at a time. When this event is detected, the diffusion barrier can be calculated using the nudged elastic band method since the initial and final configurations are known. The simulation time of the event at the high temperature is extrapolated to the lower temperature of inter-

est. The TAD method uses certain conditions to determine whether this detected (or attempted) transition is likely to happen at the lower temperature of interest. If the conditions are satisfied, then the transition is accepted and the new state becomes the starting point. The simulation proceeds in the same way as before by performing MD at a high temperature to determine possible escape paths from this new state. In this way, the state to state evolution of the system can be determined over a certain period of time. The diffusive behaviour of point defects can be investigated and at the same time, the corresponding energy barriers can be calculated.

In this chapter, TAD was employed to study the diffusion of point defects in the spinel structure. The mechanisms and activation barriers for motion were determined using TAD. An overview of the TAD method is provided in the first section of this chapter. However, a complete derivation of the method can be found in the original paper by Sørensen and Voter [3]. The point defect configurations obtained from the collision cascades were utilised as input for the TAD simulations to follow their long time evolution. The results for the normal magnesium aluminate, the half-inverse magnesium gallate and the fully inverse magnesium indate spinels are presented in the remaining sections of this chapter.

6.2 The TAD method

For an infrequent-event system of N atoms vibrating in a basin of the potential energy surface, the waiting time t, spent in that basin before escaping to the next basin, is exponentially distributed with a probability distribution given by

$$f(t)dt = k_i e^{-k_i t} dt, \tag{6.1}$$

where, k_i is the rate constant for the transition i. Under the harmonic approximation [85], the rate constant is given by the Arrhenius equation

$$k_i = \nu e^{-E_a/k_B T}. \tag{6.2}$$

Here, E_a is the activation energy of the process, ν is the attempt frequency typically in the range of 10^{12}–10^{13} s^{-1}, and k_B is the Boltzmann's constant. The temperature accelerated dynamics method [3] is based on the above assumptions.

A system at a certain temperature T_{low}, can move from one state to another through a number of possible escape paths. These events occur at a faster rate at a higher temperature T_{high}. The TAD method performs basin-constrained MD (BCMD) at T_{high} so as to explore the possible escape paths from a particular basin, and to filter out the transition that would occur at the temperature of interest. The BCMD method evolves the system from some initial state A, until a transition to another state B is detected, records that transition as well as the time of the event, and places the system back to its initial state A in order to find other escape paths. For each transition, the activation energy is determined using the nudged elastic band method [86] and the high temperature (t_{high}) waiting time is extrapolated to the low temperature (t_{low}) which is of interest using the equation

$$t_{low} = t_{high} e^{E_a(1/k_B T_{low} - 1/k_B T_{high})}. \tag{6.3}$$

Both t_{low} and t_{high} belong to the waiting time distribution given in eqn. 6.1. For two different attempted transitions happening at $t_{high,1}$ and $t_{high,2}$ where $t_{high,2} > t_{high,1}$, it is not necessary that $t_{low,2} > t_{low,1}$. The chronological order can change at the low temperature as shown by the two solid lines in fig. 6.1.

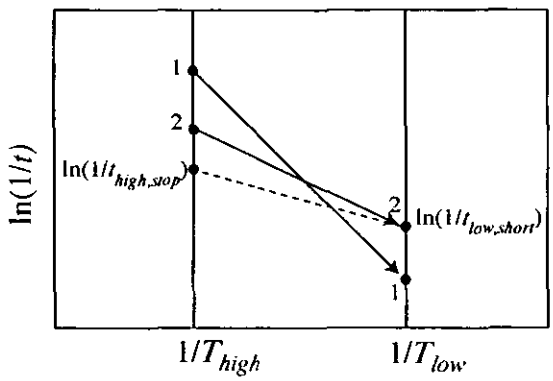

Figure 6.1: Each attempted transition at the high temperature is extrapolated to the low temperature. The gradient of the line represents the negative of the activation energy. The high temperature MD simulation is continued until the high temperature time becomes $t_{high,stop}$, and the event with the shortest extrapolated time is accepted. (Adapted from [3])

The stopping criterion for the BCMD procedure is given by

$$t_{high,stop} = \frac{\ln(1/\delta)}{\nu_{min}} \left(\frac{\nu_{min} t_{low,short}}{\ln(1/\delta)} \right)^{T_{low}/T_{high}}, \tag{6.4}$$

where δ is a control parameter, ν_{min} is an assumed minimum of the attempt frequency and $t_{low,short}$ is the current minimum escape time determined for T_{low}. δ denotes the level of uncertainty that after $t_{high,stop}$ no new transition with extrapolated time shorter than $t_{low,short}$ would occur.

At the end of the BCMD procedure, a list of escape paths and attempted escape times at T_{high} for a particular basin is obtained. Out of this list, the transition with the fastest extrapolated time at T_{low} is accepted and the system is moved to the state that this transition leads to. The process is repeated in this new state. By simulating a total time $t_{high,stop}$ at the high temperature, the simulation time at the low temperature is advanced by $t_{low,short}$, yielding to boost factor of $t_{low,short}/t_{high,stop}$ for the accepted transition.

An important part of the method relies on the calculation of the activation energy

for each attempted transition. This is done by using the nudged elastic band method (NEB) [86]. The NEB method constructs a number of images of the system with intermediate configurations between the initial and final states of the system. Starting with the initial state and ending with the final state, a continuous chain is obtained by connecting every successive image to the next via a spring interaction, thus mimicking an elastic band. An iterative procedure is used to minimise the force acting on the images so as to converge the elastic band of images towards the minimum energy path (MEP) between the initial and final states. The activation energy of the transition is then determined by finding the saddle point which is the position along the MEP with the maximum energy.

The chain of images can be represented by the positional vectors [$\mathbf{R}_0$, $\mathbf{R}_1$, $\mathbf{R}_2$,..., $\mathbf{R}_N$], where $\mathbf{R}_0$ and $\mathbf{R}_N$ denote the initial and final states respectively. The positional vectors of the $N-1$ intermediate images are determined by linear interpolation of atomic coordinates:

$$\mathbf{R}_i = \mathbf{R}_0 + \frac{i}{N}(\mathbf{R}_N - \mathbf{R}_0). \tag{6.5}$$

The effective force $\mathbf{F}_i$, acting on each image is given by the sum of the spring forces along the tangent of the elastic band and the perpendicular component of the true force due to the interatomic potential V:

$$\mathbf{F}_i = \mathbf{F}_i^s|_{\parallel} - \nabla V(\mathbf{R}_i)|_{\perp}. \tag{6.6}$$

The force component perpendicular to the elastic band is given by

$$\nabla V(\mathbf{R}_i)|_{\perp} = \nabla V(\mathbf{R}_i) - \nabla V(\mathbf{R}_i) \cdot \hat{\mathbf{T}}_i \, \hat{\mathbf{T}}_i, \tag{6.7}$$

and the spring force along the tangent path is determined by

$$\mathbf{F}_i^s|_{\parallel} = k\left[(\mathbf{R}_{i+1} - \mathbf{R}_i) - (\mathbf{R}_i - \mathbf{R}_{i-1})\right] \cdot \hat{\mathbf{T}}_i \, \hat{\mathbf{T}}_i, \tag{6.8}$$

where k is the spring constant and the term $\hat{\mathbf{T}}_i$ denotes the unit vector parallel to the elastic band's tangent at image i. In this way, the spring force does not affect the relaxation of the images perpendicular to the elastic band and the atomic configuration of the relaxed images satisfies $\nabla V(\mathbf{R}_i)|_\perp = 0$.

In general, none of the images in the relaxed configuration lands at or close to the saddle point and the saddle point energy needs to be estimated by interpolation. However, this estimation can sometimes underestimate the activation energy if two consecutive images lie on opposite sides of the saddle point. A variant of the regular NEB, called the climbing image NEB (CI-NEB), has been devised in order to get a better convergence to a saddle point [87]. The CI-NEB performs a few steps of the regular NEB, after which the image with the highest energy is identified. While the force on the remaining images is determined by eqn. 6.6, the force on the highest energy image, called the climbing image, is given by

$$\mathbf{F}_i = -\nabla V(\mathbf{R}_i) + 2\nabla V(\mathbf{R}_i) \cdot \hat{\mathbf{T}}_i \, \hat{\mathbf{T}}_i. \tag{6.9}$$

This is the force due to the potential with the component along the elastic band inverted. In this way, the climbing image tries to maximize its energy along the band, and minimize it in all other directions. The remaining images reproduce the trajectory along which this maximisation is carried out so that the climbing image eventually converges exactly to the saddle point. Since no spring interaction is included between the climbing image and its neighbours, the spacing on either side of this image will be different.

Both the NEB and CI-NEB methods do not have any restriction on the number of atoms involved in any particular transition and therefore make it suitable for collective jumps. The CI-NEB method was employed to find the energy barriers in our TAD simulations. The TAD code was obtained from Art Voter and Blas Uberuaga from Los Alamos National Laboratory, USA. The input variables used for the simulation

of point defects in spinels are given below.

The TAD algorithm was set to record a transition if any atomic movement exceeding 0.3 Å occurred. We assumed a minimum prefactor ν_{min} of 10^{12} s^{-1} and an uncertainty parameter δ of 0.05. Typical temperatures of 300 K and 2000 K were assigned to T_{low} and T_{high} respectively. The simulations were performed in systems containing 448 atoms with periodic boundary conditions along the three coordinate axes. Earlier work in MgO by Uberuaga *et al.* showed that the energy barriers were within 0.05 eV of the converged values when using a 512 atom cell as compared to a cell containing 1728 atoms [88]. A similar convergence is expected for the energy barriers computed in this work. The standard Ewald sum was used to calculate the electrostatic part of the potential. The CI-NEB method with 13 images and a spring constant of 2.72 eV/Å^2 (0.1 Hartrees/Å^2) was used to determine the energy barrier for each attempted transition. The simulations were run long enough so that the diffusion paths of the point defects can be analysed.

6.3 Normal spinel, $MgAl_2O_4$

Table 6.1 shows the activation energies and the corresponding mechanisms for point defects to diffuse in the normal magnesium aluminate spinel.

The oxygen split interstitial defect, O_i''–$V_O^{\cdot\cdot}$–O_i'', has the lowest activation energy of 0.29 eV for diffusion. It diffuses along the ⟨110⟩ direction via a one-dimensional interstitialcy mechanism as illustrated in fig. 6.2 (a)-(b). This mechanism allows the oxygen split interstitial to migrate very quickly along this path. The defect can also diffuse by re-orienting along a different ⟨110⟩ direction via two mechanisms. These are illustrated in fig. 6.2 (b)-(e). The O_i''–$V_O^{\cdot\cdot}$–O_i'' defect in (b) overcomes an energy barrier of 0.67 eV to move to the configuration shown in (c), while the defect transition from configuration (d) to (e) requires an activation energy of 0.64 eV.

The complex nature of the oxygen split interstitial diffusion has consequences

Table 6.1: Activation energies (E_a) and mechanisms for point defect diffusion in the normal spinel.

Defect	E_a (eV)	Diffusion mechanism
O_i''–$V_O^{\cdot\cdot}$–O_i''	0.29	1-D along ⟨110⟩
	0.64, 0.67	Re-orientation to new ⟨110⟩ direction
$Mg_i^{\cdot\cdot}$–V_{Mg}''–$Mg_i^{\cdot\cdot}$	0.56, 0.74	3-D diffusion
$Al_i^{\cdot\cdot\cdot}$		forms a split interstitial with Mg atom under minimisation
	0.57	results in an $Al_{Mg}^{\cdot}$ antisite and a Mg split interstitial
$V_O^{\cdot\cdot}$	1.49, 1.66	Direct ⟨110⟩ hops with 2 possible mechanisms
V_{Mg}''	0.68	Step 1: Intermediate divacancy V_{Mg}''–$Mg_i^{\cdot\cdot}$–V_{Mg}''
	0.09	Step 2: $Mg_i^{\cdot\cdot}$ can move toward any of the two V_{Mg}''
V_{Al}'''	2.00	Step 1: Divacancy formation V_{Al}'''–$Al_i^{\cdot\cdot\cdot}$–V_{Al}'''
	0.33	Step 2: $Al_i^{\cdot\cdot\cdot}$ recombines with any of the two vacancies
	3.28	a Mg atom moves to the Al vacancy site

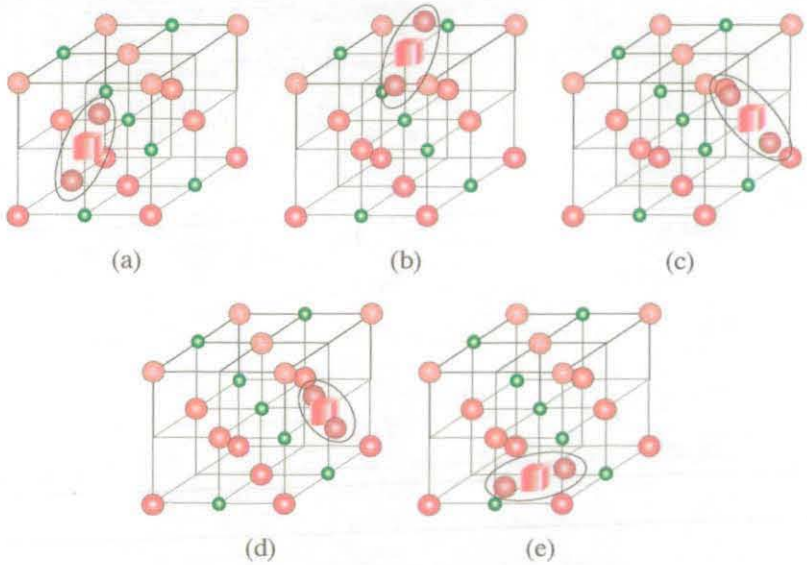

Figure 6.2: Diffusion of oxygen split interstitial in $MgAl_2O_4$. The defect overcomes an activation energy of 0.29 eV to diffuse along its axis, as shown in (a) and (b). Re-orientation mechanisms occur with barriers of 0.67 eV and 0.64 eV for transitions from configuration (b) to (c), and from (d) to (e) respectively.

for the interstitial-vacancy recombination. If a vacancy lies along the same ⟨110⟩ direction as a split interstitial, both defects can effectively annihilate via the one-dimensional split interstitial diffusion. However, if the two defects are not aligned, the oxygen split interstitial is still attracted to the vacancy such that it minimises the distance between the two defects given the constraint that it has to remain on the path along its axis. Once this distance is minimised, the split interstitial is trapped by the vacancy, but it cannot recombine until a longer timescale associated with the re-orientation barrier has passed. Assuming an attempt frequency of 10^{13} /s, this time will be about 5 ms. Thus, while the oxygen defects will essentially trap one another, eliminating their mobility, they will not necessarily recombine. This re-orientation mechanism has a much longer waiting time as confirmed by the residual defects of the collision cascade simulations, which did not see recombination when the split interstitial and vacancy were not aligned (for example in fig. 4.15 (c)). However in some cases where the anion split interstitial had sufficient kinetic energy, the split interstitial could annihilate with a vacancy via the rotation mechanism as shown in fig. 4.16.

The magnesium split interstitial diffuses in the spinel structure via an interstitialcy mechanism by keeping the same configuration throughout the motion, i.e. the two interstitials always occupy structural octahedral vacancies around the tetrahedral magnesium vacancy. There are two diffusion mechanisms for the $Mg_i^{\cdot\cdot}$–V''_{Mg}–$Mg_i^{\cdot\cdot}$ defect with activation energies of 0.56 eV and 0.74 eV. The lower energy saddle involves a rotation of the axis plus translation of the split interstitial as shown in fig. 6.3, while the higher energy saddle, shown in 6.4, is a pure translation. The higher energy mechanism would yield a one-dimensional diffusion while the lower energy mechanism allows for isotropic diffusion.

The isolated Al interstitial is unstable. It was never observed in the collision cascades. The TAD simulation on an Al interstitial resulted in a split Mg–Al interstitial centred about a Mg vacancy upon minimisation of the defect. The resulting struc-

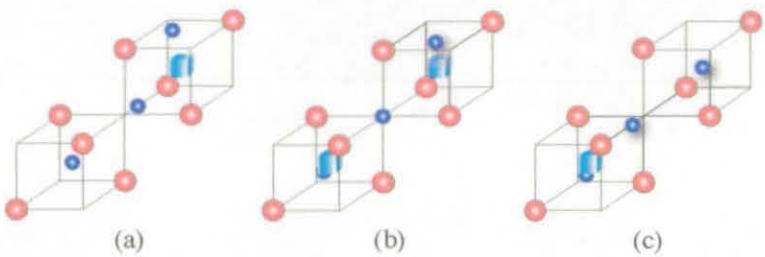

Figure 6.3: $Mg_i^{\cdot\cdot}$–V''_{Mg}–$Mg_i^{\cdot\cdot}$ split interstitial diffusion in spinel. The defect moves from (a) to (c) via the saddle shown in (b). The activation barrier for this process is 0.56 eV.

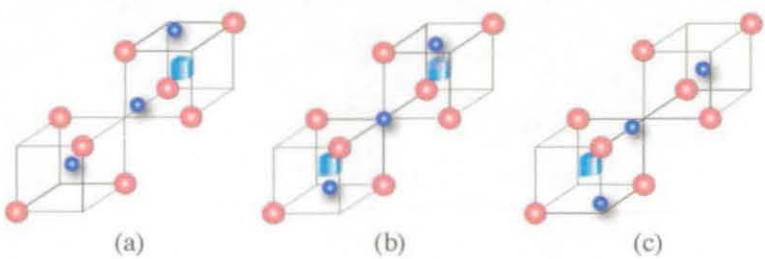

Figure 6.4: Second diffusion mechanism for a Mg split interstitial. The initial and final defect configurations are along the same axis. The activation barrier for the mechanism is 0.74 eV.

ture is metastable. It can oscillate about the Al interstitial which remains fixed, or it can transform to a pure Mg split interstitial and an $Al^{\cdot}_{Mg}$ antisite with a barrier of 0.57 eV, bringing the system into a lower energy state. In the latter situation, the two positively charged defects repel one another with the result that the Mg split interstitial is free to migrate.

The oxygen vacancy has 12 nearest oxygen ions which can take part in the diffusion process as shown in fig. 6.5. Because of the oxygen dilatation in the spinel structure, the anion sublattice is slightly distorted, resulting in three different distances of 2.47 Å for the oxygen ions numbered 4, 5 and 6 with the central O vacancy, 2.89 Å for the ions numbered 7-12 and 3.27 Å for the anions at 1, 2 and 3. In the perfect structure, these distances would have been equal to 2.87 Å. Here, the oxygen vacancy can therefore make three different types of moves. It can move to sites 4, 5 and 6 with a barrier of 1.49 eV. Motion in the intermediate range (7-12) has a larger barrier of 1.66 eV. Finally, diffusion to the furthest neighbours (1,2 or 3) never occurred. The path for diffusion was along ⟨110⟩ with the saddle point midway between the two vacancies. For net diffusion to occur, hops to the intermediate neighbours must occur; otherwise, the oxygen vacancy just hops between the nearest set of oxygen positions.

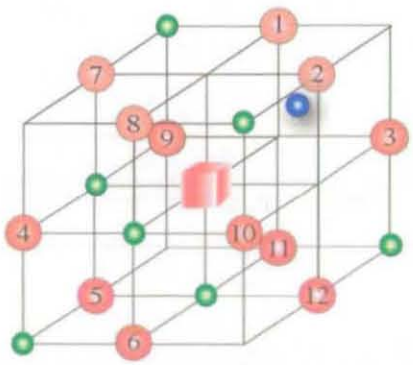

Figure 6.5: Part of the normal spinel structure containing an oxygen vacancy (red cube) is shown with its 12 first n.n. anions. The barriers for diffusion of the central vacancy to sites 4, 5, 6 and 7-12 are 1.49 eV and 1.66 eV respectively.

Cation vacancy diffusion is very similar for both types of cations. First, there is an intermediate state of split vacancy formation, where the displaced cation sits at an interstitial position midway between the two vacancies. For example, the V''_{Mg} results in a split vacancy V''_{Mg}–$Mg^{\cdot\cdot}_{i}$–V''_{Mg}, with the moving Mg ion occupying an octahedral site as illustrated in fig. 6.6 (c). The activation energy for this process is 0.68 eV. From this site, there is a small energy barrier of 0.09 eV for this ion to recombine to either vacancy. The barrier for the Al vacancy migration is much higher, 2.00 eV, so that Al vacancies are practically immobile at 300 K. Likewise, the exchange of a Mg ion with the Al vacancy has a very high energy barrier of 3.28 eV.

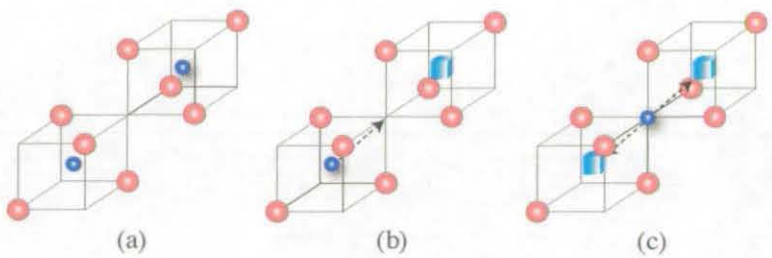

Figure 6.6: Mg vacancy diffusion in normal $MgAl_2O_4$ spinel. (a) The perfect lattice. The Mg vacancy in (b) overcomes a barrier of 0.68 eV to form the split vacancy in (c) where the interstitial occupies an octahedral site. The Mg interstitial in (c) can recombine to either of the two V''_{Mg} with a small barrier of 0.09 eV.

In conclusion therefore, the diffusive behaviour of point defects in the normal $MgAl_2O_4$ shows that the fastest diffusing species is the oxygen split interstitial. It diffuses one-dimensionally along the ⟨110⟩ direction with a barrier of 0.29 eV and has a barrier of 0.64 eV to re-orient. The Mg split interstitial diffuses three-dimensionally with a barrier of 0.56 eV while the Al interstitial is not stable and decays to an Al antisite and a Mg split interstitial. Vacancy diffusion on both the oxygen and aluminium sublattices is much slower than the magnesium vacancy.

6.4 Half-inverse spinel, $MgGa_2O_4$

Unlike in the normal spinel where point defects diffuse via well-defined pathways, diffusion in the half-inverse and inverse spinels is much more complex. The environment around each oxygen ion in the normal spinel is identical, whereas in spinels with disorder, there are many different local environments around the anions. These sites are characterised by the over/under bonding value of the oxygen ion as described in section 2.1.4. As the level of inversion of the spinel is increased, more local environments become available. This is illustrated in fig. 6.7 showing the energetics of the oxygen vacancy as a function of the over/under bonding value in $MgGa_2O_4$. It is clear that the oxygen vacancy energy is strongly correlated with the local environment. Roughly, as the local environment goes from Mg-rich to Ga-rich, the energy of the oxygen vacancy increases. Thus, the oxygen vacancy strongly prefers Mg-rich regions.

The variation of the vacancy energy as a function of local environment in the $MgGa_2O_4$ system with $i = 0.5$, employed for the TAD simulations, is illustrated in fig. 6.8. The figure shows that for the same type of ion, different vacancy energies are obtained at different locations in the lattice. This has important implications on the diffusive behaviour of point defects as discussed below.

While in the normal spinel, defects diffuse throughout the simulation cell, defects in the half-inverse and inverse spinels are typically confined to just few sites and are unable to diffuse throughout the cell. Moreover, the same defect located at different sites has different barriers for motion depending on the initial and final states. The defect kinetics in the half-inverse spinel is summarised table 6.2 showing the energy barriers for motion and the associated mechanism.

The oxygen split interstitial primarily moves by a similar one-dimensional mechanism along the ⟨110⟩ and can re-orient to other ⟨110⟩ directions as in the normal spinel. However, it can also change to a different ⟨110⟩ alignment via a new rotation

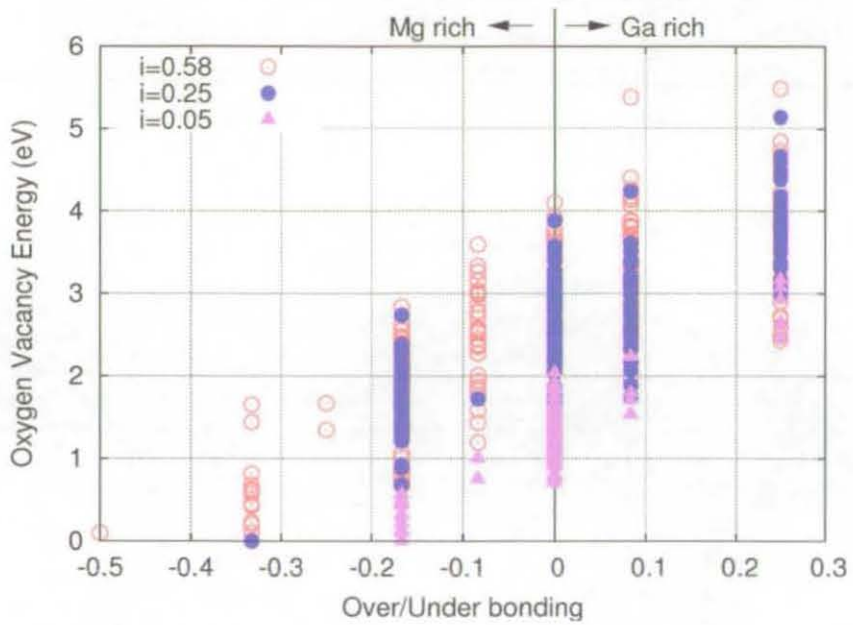

Figure 6.7: Energy of oxygen vacancy states versus over/under bonding values for $MgGa_2O_4$ as a function of inversion, relative to the lowest energy site. As the inversion is increased, more local environments become available. There is a clear preference of the oxygen vacancy for sites that are under bonded, or Mg-rich. Figure courtesy of Blas Uberuaga [89].

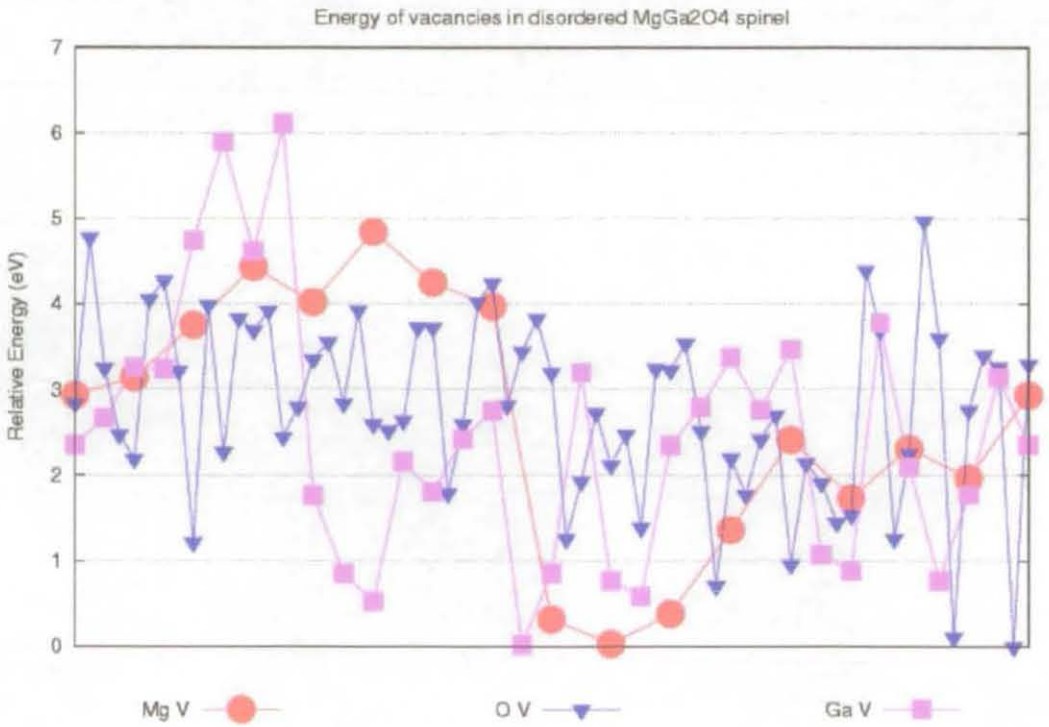

Figure 6.8: Vacancy energies in the half-inverse spinel. V''_{Mg} are shown by the red circles, $V_O^{\cdot\cdot}$ are denoted by the dark blue inverted triangles, and V'''_{Ga} are shown by the pink squares. Energies span up to 6 eV for the same defect but at different locations in the lattice. Figure courtesy of Blas Uberuaga.

Table 6.2: Point defect motion in the half-inverse spinel. A range of energy barriers is obtained for the same defect because of different cation environments in the spinel. The notation 'T' and 'O' within brackets refer to tetrahedral and octahedral coordination with oxygen atoms respectively.

Defect	E_a (eV)	Mechanism for motion
O_i''–$V_O^{\cdot\cdot}$–O_i''	0.09 – 0.89	1-D motion along ⟨110⟩
	0.51 – 0.99	Re-orientation mechanism to another ⟨110⟩ direction
	0.33 – 0.86	New rotation mechanism to another ⟨110⟩ alignment
$Mg_i^{\cdot\cdot}$–V''_{Mg}–$Mg_i^{\cdot\cdot}$	0.15 – 0.57	3-D interstitialcy motion
	0.09 – 0.60	Changes to new ⟨110⟩ orientation by a 1-atom move
	0.56 – 0.69	⟨110⟩ to ⟨311⟩ orientation about the vacancy
$Mg_i^{\cdot\cdot}$–V''_{Mg}–$Ga_i^{\cdot\cdot\cdot}$	0.23	forms $Mg_i^{\cdot\cdot}$–V''_{Mg}–$Mg_i^{\cdot\cdot}$ + $Ga_{Mg}^{\cdot}$
$Mg_i^{\cdot\cdot}$–V'''_{Ga}–$Ga_i^{\cdot\cdot\cdot}$	0.01	recombination of $Ga_i^{\cdot\cdot\cdot}$ with V'''_{Ga} leaving pure Mg split
$Ga_i^{\cdot\cdot\cdot}$–V'''_{Ga}–$Ga_i^{\cdot\cdot\cdot}$		breaks into $Ga_i^{\cdot\cdot\cdot}$–V''_{Mg}–$Mg_i^{\cdot\cdot}$ under minimisation
V''_{Mg} (T)	0.18 – 0.39	split vacancy formation with next Mg (T) atom
	0.18 – 1.07	V''_{Mg} (T) to next V''_{Mg} (T) site
	0.40 – 1.37	V''_{Mg} (T) to next V''_{Mg} (O) site
	0.62, 0.71	split vacancy formation with next Ga (T) atom
V'''_{Ga} (T)	0.09	results in a Mg'_{Ga} and V''_{Mg} (T)
V''_{Mg} (O)	0.14, 0.32	$V''_{Mg} \rightarrow V''_{Mg}$–$Mg_i^{\cdot\cdot}$–$V''_{Mg}$
	0.90 – 1.93	$V''_{Mg} \rightarrow V''_{Mg}$–$Ga_i^{\cdot\cdot\cdot}$–$V'''_{Ga}$
	0.14 – 1.08	direct vacancy moves V''_{Mg} (O) $\rightarrow$ V''_{Mg} (O)
	2.02	direct vacancy moves resulting in V'''_{Ga} + $Ga_{Mg}^{\cdot}$
V'''_{Ga} (O)	0.63	Step 1: V''_{Mg}–$Mg_i^{\cdot\cdot}$–V'''_{Ga} split vacancy formation with Mg
	0.04	Step 2: split vacancy resulting in V'''_{Mg} (O) + Mg'_{Ga}
$V_O^{\cdot\cdot}$	0.59 – 0.85	Motion towards Mg rich region
	2.05 – 2.33	Motion from Mg rich environment to Ga rich

mechanism as shown in fig. 6.9. Here, the central vacancy of the O split interstitial acts as a pivot, around which the two anions rotate to align along an adjacent ⟨110⟩ anion row with a different orientation. In this case the energy barrier to perform the move is 0.86 eV but barriers as low as 0.33 eV are possible for this move with a different local arrangement of ions. When the TAD simulation reached a time of 14 ms at the lower temperature of 300 K, the system's energy was 0.63 eV lower as compared to the initial state due to the defect motion in the system.

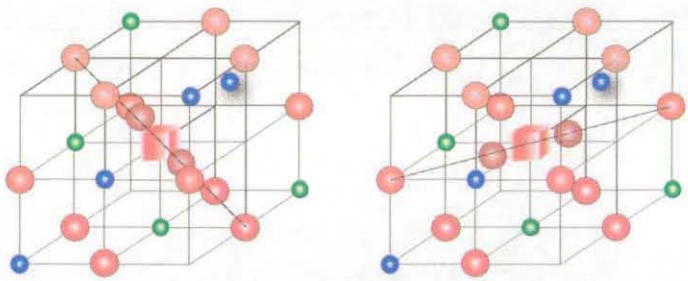

(a) (b)

Figure 6.9: Rotation mechanism for the O_i''–$V_O^{\cdot\cdot}$–O_i'' split interstitial in the half-inverse spinel, $MgGa_2O_4$. The activation energy is 0.86 eV for the transition from configuration (a) to (b).

The constrained defect motion in the half-inverse spinel is evident for the $Mg_i^{\cdot\cdot}$–V_{Mg}''–$Mg_i^{\cdot\cdot}$ split interstitial. Only three distinct types of events were seen during one simulation of a Mg split interstitial in which 526 events were accepted. One event, shown in fig. 6.10 (b)-(c), has a barrier of 0.15 eV for motion of the split interstitial to a neighbouring site via a similar mechanism as in the normal spinel. The other two mechanisms, with barriers of 0.09 eV and 0.56 eV, resulted in the re-orientation of the split interstitial. The defect changes to a different ⟨110⟩ orientation by the rearrangement of one interstitial from its current octahedral site the next unoccupied one as illustrated in fig. 6.10, (b) to (d) transition (E_a = 0.09 eV). In the third mechanism shown by the transition (b) to (e) in fig. 6.10, both interstitials move to adjacent sites along the ⟨311⟩ direction around the same vacancy. In this new

configuration, one interstitial occupies an octahedral site while the other interstitial occupies a tetrahedral site.

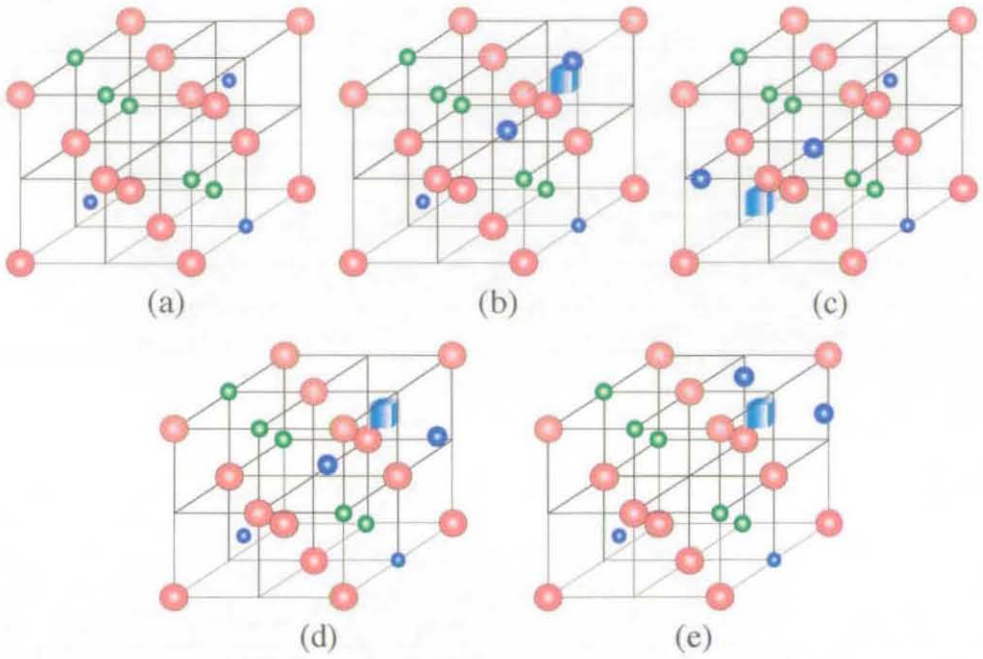

Figure 6.10: Motion of a Mg split interstitial in the disordered $MgGa_2O_4$ spinel. (a) Perfect structure, (b) $Mg_i^{\cdot\cdot}$–V''_{Mg}–$Mg_i^{\cdot\cdot}$ aligned along ⟨110⟩ with both $Mg_i^{\cdot\cdot}$ filling octahedral sites. Three observed mechanisms are shown from configurations (b) to (c), (b) to (d) and (b) to (e) with corresponding barriers of 0.15 eV, 0.09 eV and 0.56 eV respectively.

Cation split interstitials made up of Ga interstitials or/and vacancies were found to be only metastable. Split interstitial structures $Mg_i^{\cdot\cdot}$–V''_{Mg}–$Ga_i^{\cdot\cdot\cdot}$, $Mg_i^{\cdot\cdot}$–V'''_{Ga}–$Ga_i^{\cdot\cdot\cdot}$ and $Ga_i^{\cdot\cdot\cdot}$–V'''_{Ga}–$Ga_i^{\cdot\cdot\cdot}$ fairly quickly decay to other defects. The first structure results in a Mg split interstitial and a $Ga_{Mg}^{\cdot}$ defect after a fraction of a μs at 300 K, accompanied by a decrease of 0.69 eV in the system's energy. The second defect decays much faster, after only 29 ps at 300 K, to a Mg split interstitial after the Ga ion recombines with the Ga vacancy, with the new configuration lower in energy by 1.20 eV. The third structure is not stable at all; upon minimisation, it transforms to the first structure, which again decays to a Mg split interstitial and a $Ga_{Mg}^{\cdot}$.

There is a strong electrostatic influence on the motion of the oxygen vacancy in

the half-inverse spinel. The oxygen vacancy preferentially migrates towards Mg rich regions. An oxygen vacancy, starting with four Ga neighbours, very quickly moves via a sequence of transitions with activation energies of 0.78 eV, 0.59 eV, and 0.85 eV, to a site with one Ga and three Mg neighbours and is essentially trapped there for the duration of the simulation. This final state is a lower energy by 4.06 eV. On the other hand, high activation barriers were required for the vacancy to move from Mg rich region to the Ga rich region.

The Mg vacancy, when placed on an octahedral site, is essentially trapped there. It can either form a split vacancy structure with a nearby tetrahedrally coordinated Mg ion, or directly move to a neighbouring site, but always returns to the original structure. It is also able to convert into a $Ga^{\cdot}_{Mg}+V'''_{Ga}$ with a barrier of 2.02 eV. When the Mg vacancy was placed at a tetrahedral site, it made several diffusive jumps via mechanisms similar to that shown in fig. 6.6, until it induced the formation of a cation disorder pair: $Ga^{\cdot}_{Mg}+Mg'_{Ga}$. This was accompanied by the Mg vacancy moving to an octahedral position where it was trapped. The TAD time for this to occur was 6.4 μs at 600 K.

An octahedrally coordinated Ga vacancy could move via a two-step mechanism allowing a neighbouring octahedral Mg ion to form first a split vacancy defect with the octahedral Ga vacancy, before transforming to a $Mg'_{Ga}+V''_{Mg}$. Motion of the octahedral Mg vacancy could then follow as described above. The tetrahedral Ga vacancy also decayed to a tetrahedral Mg vacancy and a stable Mg'_{Ga} defect, a process with an activation barrier of 0.09 eV only. The mobility of the resulting Mg vacancy was similar to that of the isolated tetrahedral Mg vacancy described above.

The conclusions from the TAD simulations on the half-inverse spinel is that defect mobility is significantly hindered compared to the normal spinel. While elementary motions are similar to those in the normal spinel, defects are essentially trapped by the disorder in the half-inverse spinel and cannot easily diffuse through the cell, at least on the time scales accessible with TAD. Often, point defects induce cation

mixing. This is especially true for Ga defects, which tend to decay to cation disorder defects and Mg point defects.

6.5 Inverse spinel, $MgIn_2O_4$

Defect motion in the inverse spinel is constrained in a similar way as in the half-inverse spinel. The defects only move locally in a restricted way due to the disorder. Table 6.3 shows the main mechanisms for point defects to move in the inverse spinel.

Table 6.3: Energy barriers and mechanisms for defect motion in the inverse spinel, $MgIn_2O_4$.

Defect	E_a (eV)	Diffusion mechanism
O_i''–$V_O^{\cdot\cdot}$–O_i''–$V_O^{\cdot\cdot}$–O_i''	0.32, 0.89 0.80 – 1.33	1-D diffusion back and forth rotation barrier to next ⟨110⟩ alignment
$In_i^{\cdot\cdot\cdot}$–V_{In}'''–$In_i^{\cdot\cdot\cdot}$	0.07 0.11 – 0.60	ground state is In crowdion, $In_i^{\cdot\cdot\cdot}$–V_{In}'''–$In_i^{\cdot\cdot\cdot}$–V_{In}'''–$In_i^{\cdot\cdot\cdot}$ crowdion to crowdion movement
$V_O^{\cdot\cdot}$	0.60 – 1.36	different diffusion mechanisms
V_{Mg}''	1.02 – 1.12	motion on the Mg sublattice by direct hops
V_{In}''' (O)	1.24, 1.34	decays to V_{Mg}'' and Mg_{In}'
V_{In}''' (T)	0.23	ground state split vacancy V_{In}'''–$In_i^{\cdot\cdot\cdot}$–V_{In}'''

The one-dimensional oscillatory motion of the O crowdion structure, observed during the collision cascade simulations, is the main mechanism in the TAD simulation. This motion is illustrated in fig. 6.11. Two of the three oxygen interstitials making the crowdion has three In and one Mg nearest neighbours while the third oxygen (encircled in fig. 6.11) has four In nearest neighbours. The extra attractive forces between the one oxygen ion and the 4 In ions meant that more energy was required for the crowdion to break that bond and diffuse as compared to a sliding mechanism over that bond. The latter mechanism is schematically represented by the transition from (a) to (b) in fig. 6.11 having an energy barrier of 0.32 eV, while the former mechanism, illustrated by the transition from (a) to (c), has a higher activation energy of 0.89 eV. The crowdion could change to other ⟨110⟩ directions with

energy barriers between 0.80 and 1.33 eV, but it never left the immediate vicinity of its starting location over the ms time scales at 300 K.

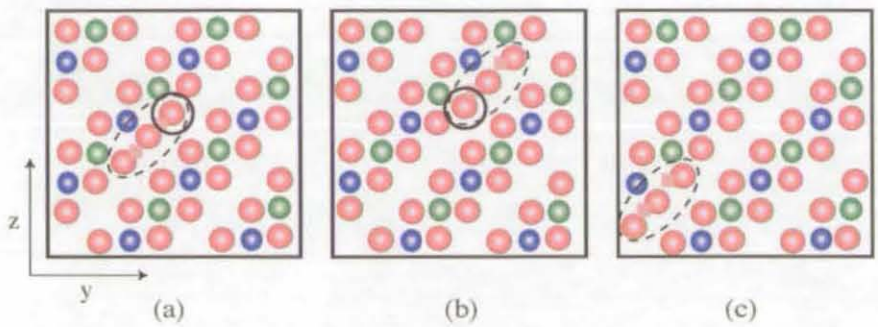

Figure 6.11: Diagram illustrating the 1-D motion of the O_i''–$V_O^{\cdot\cdot}$–O_i''–$V_O^{\cdot\cdot}$–O_i'' crowdion in the $MgIn_2O_4$ crystal. The defect is identified by the dashed ellipse while the continuous circle denotes the O interstitial with four nearest In neighbours. E_a = 0.32 eV for transition (a) to (b) but E_a = 0.89 eV for transition (a) to (c).

An In split interstitial defect immediately relaxed to a typical crowdion structure, $In_i^{\cdots}$–V_{In}'''–$In_i^{\cdots}$–V_{In}'''–$In_i^{\cdots}$, similar the defect shown in fig. 5.7 (d) and labelled H. The local environment around the defect is illustrated in fig. 6.12 (b). The crowdion showed no net diffusion over μs timescales but only hopped from one crowdion configuration to another with activation barriers between 0.11 eV and 0.60 eV. The motion of two other types of cation split interstitials, namely the $In_i^{\cdots}$–V_{In}'''–$Mg_i^{\cdot\cdot}$ and the $Mg_i^{\cdot\cdot}$–V_{In}'''–$Mg_i^{\cdot\cdot}$, also resulted in no net diffusion.

The oxygen vacancy was typical of what was seen during the collision cascades for example in fig. 5.6 (d) and labelled F; it displaces its nearest tetrahedral In ion slightly off its perfect site. The vacancy preferentially moved from In-rich environments to Mg-rich environments, just as in the half-inverse spinel. This diffusion occurred via barriers between 0.60 eV and 1.36 eV.

In the inverse $MgIn_2O_4$ structure, all Mg ions reside on octahedral sites. The Mg vacancy moves only on the Mg sublattice via direct jumps with a barrier of about 1 eV. The octahedrally-coordinated In vacancy decays to an Mg vacancy and a Mg_{In}' defect via mechanisms with 1.24/1.34 eV barrier. Motion of the Mg vacancy followed

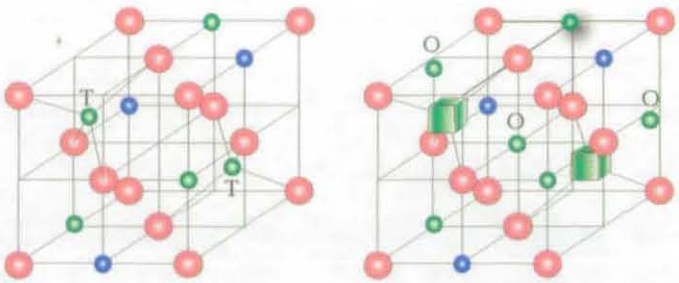

(a) (b)

Figure 6.12: (a) Part of the inverse $MgIn_2O_4$ spinel with 'T' denoting In ions with tetrahedral coordination. (b) Stable crowdion defect where an extra In interstitial displaces the tetrahedral ions to octahedral sites labeled 'O'. The cubes denote In vacancies.

whereas the cation disorder defect remained immobile.

The tetrahedrally-coordinated In vacancy could move to an In split vacancy defect with the In ion located at the octahedral interstice midway between the two tetrahedral vacancies. The activation barrier for this process is 0.23 eV while the final configuration is lower in energy by 1.39 eV. The stability of the In ion at an octahedral interstice in the inverse spinel was also consistent with the arrangement in the In crowdion, and the observation from the collision cascades that indicate the preferential segregation of In ions to octahedral sites under irradiation.

The results show that no net diffusion of point defects occurred in the inverse spinel over the time scales accessible to TAD. The simulations on the In interstitial showed that the defect formed a stable crowdion defect which is a dominant defect seen in the collision cascade simulations.

6.6 Discussions and conclusions

The kinetics of point defects in the normal spinel, in the half-inverse spinel and in the inverse spinel was examined using temperature accelerated dynamics. While in the normal spinel, point defects diffuse via well defined pathways, their diffusivity is

greatly inhibited in the spinels with inversion. Because of the disorder, each potential defect site has a different local environment and thus a different energy, leading to preferred sites for different types of defects. Over the timescales accessible to TAD, no net diffusion was observed in the half-inverse and inverse spinels.

The most direct measurement for point defect migration was for irradiated $MgAl_2O_4$ for which the shrinkage speed of dislocation loops was monitored and a diffusion barrier for the rate-limiting (slowest) vacancy was estimated [90]. The migration energy of this vacancy was found to be 2.0±0.7 eV but the identity of this vacancy was not established. This corresponds to the value of 2.00 eV obtained for V'''_{Al}. The barrier for V''_{Mg} is significantly lower (0.68 eV) while that of $V_O^{\cdot\cdot}$ is just slightly lower (1.67 eV) than the experimental value. This would suggest that V'''_{Al} is the rate controlling species for this process.

The activation energy for self-diffusion of oxygen ions in magnesium aluminate spinel was found to be 4.55±0.69 eV [91]. In the same publication, this parameter was quoted as 3.73 eV for the self diffusion of the magnesium ion from the work by Lindner and Akerstrom [92]. These values include the formation energy as well as the migration energy and are not directly comparable to our results.

It has been assumed in experimental analysis [93] that at cryogenic temperatures vacancy mobility is much smaller than interstitial mobility in $MgAl_2O_4$. TAD simulations in MgO showed that interstitials diffuse quickly while vacancies are immobile at room temperature [88], in agreement with experimental estimates [63]. Similarly in Al_2O_3, interstitials were found to be more mobile than vacancies [63]. However, in $MgAl_2O_4$, V''_{Mg} diffuses with a barrier (0.68 eV) very similar to $Mg_i^{\cdot\cdot}$ (0.58 eV) and only about two times larger than the fastest diffusing species O_i'' (0.29 eV). Thus, the assumption that vacancy mobility is insignificant at low temperatures, may be erroneous for spinels.

The mobility of point defects in ionising environments has been investigated experimentally in $MgAl_2O_4$ by irradiation with ions of varying mass and energy [94, 95].

It is found that changing the charge state of point defects by ionisation can have a significant impact on the defect dynamics. Ionisation-enhanced diffusion is one example which can lead to the suppression of amorphisation. However, our model is unable to deal with different charge states in the system, and thus predicting these mechanisms is not trivial.

The radiation tolerance of complex oxides such as spinels is mainly attributed to efficient interstitial-vacancy recombination mechanisms and the ability to accommodate disorder [62]. However, disorder also leads to reduced diffusivity of point defects as seen in the half-inverse and inverse spinels. At first glance, it seems reasonable that reduced defect mobility would be detrimental from a radiation recovery perspective as defect recombination will be inhibited. On the other hand, reduced mobility of point defects will necessarily suppress the nucleation and growth of defect clusters, which leads to enhanced tolerance (through reduced swelling). These effects are at cross-purposes and we do not know which, in fact, will dominate to determine damage evolution. In addition, because of disorder, different defect types tend to segregate to different (either Mg-rich or Ga-rich) regions in the material, further reducing the possibility of aggregation.

The TAD simulations in the spinels with disorder were unable to reach the time scales for which net diffusion could be observed. By using kinetic Monte Carlo (KMC) much longer time scales can be reached. KMC was used our collaborator Blas Uberuaga to investigate the diffusivity of the oxygen vacancy in $MgGa_2O_4$ with inversion parameters of 0.05, 0.25 and 0.58 [89]. It was found that, as the level of inversion is increased, more types of local environments are available in the structure. These local environments become more and more effective, in trapping the oxygen vacancy, slowing its diffusion. The trajectory simulated by KMC in the cell with $i = 0.25$ at a temperature of 2000 K, showed that the diffusion path of the oxygen vacancy was pseudo-one-dimensional and that the defect could diffuse over a distance of about 0.57 μm in 0.8 s [89].

Chapter 7

Low energy cascades at MgO/Al_2O_3 interfaces

7.1 Introduction

Materials consisting of oxide-oxide or oxide-metal interfaces have a wide range of applications in engineering and advanced technologies. At elevated temperatures, these compounds can chemically react by forming intermediate phases at the interfacial region. This process can continue as reactants can diffuse from the bulk to the interface. It is therefore important to investigate the material's microstructural evolution under these conditions, so that any changes in the material's properties can be anticipated. Conversely, the solid state reactions between two solids can be utilised to fabricate materials with desirable properties.

Spinel formation by solid state reactions between a rocksalt-structured (AO) and a corundum-structured oxide (B_2O_3), is among the most widely studied systems. Among the processes investigated experimentally are: the formation of $NiAl_2O_4$ spinel from thin film deposition of NiO on (0001) oriented Al_2O_3 followed by thermal treatment (fig. 7.1) [96, 97]; the production of dendrites of $MgFe_2O_4$ spinel at the interfacial region of a Fe_2O_3/MgO system under the application of an electric field at

high temperatures [96]; the $MgAl_2O_4$ formation (solid-gas reaction) at the surface of Al_2O_3 in the presence of MgO vapour products in a hydrogen atmosphere at elevated temperatures [98]; the growth of a $MgAl_2O_4$ interface between contacting MgO and Al_2O_3 at different temperatures and pressures [99].

Figure 7.1: Cross section TEM image of spinel formation at a NiO/Al_2O_3 interface at 1375 K. NiO was first deposited on Al_2O_3 by pulsed laser deposition, then the system was heat treated to initiate the spinel reaction. Courtesy of M. T. Johnson *et al.* [96].

These solid state reactions occur via complex diffusion mechanisms which are thermally activated. In analogy to thermal activation, the formation of spinel at these interfaces might also be expected under irradiation. Such an experiment is in the process of being analysed by collaborators at Los Alamos. In this chapter, we model the effect of low-energy displacive radiation in a system of MgO/Al_2O_3 using molecular dynamics simulations. The crystal interface orientations are taken to be (111) for MgO and (0001) for Al_2O_3. Displacement cascades in the energy regime of 0.6 keV were initiated in MgO and in Al_2O_3 close to the interface at different orientations. In this preliminary work, the low energy of 0.6 keV was chosen to initiate rearrangements at the interface because of the small system size investigated.

7.2 Crystal structures

7.2.1 MgO

MgO has the rocksalt structure which consists of a face-centred cubic arrangement of oxygen ions with the Mg ions sitting at each of the octahedral sites. This arrangement can be viewed simply as Mg ions alternating with O ions along the three coordinate axes. The MgO crystal can be cleaved to produce the (100) surface, as shown in fig. 7.2 (a), which has the lowest surface energy [100]. However, cleaving the crystal along ⟨111⟩ produces a crystal which has monolayer of Mg ions on one surface and a monolayer of oxygen ions on the other as shown in fig. 7.2 (b)-(c). The (111) oriented crystal was used to set up the MgO/Al_2O_3 system so that the anion layer in MgO matches that of the Al_2O_3 crystal (see section 7.2.3). The interatomic potential gives a lattice parameter of 4.21 Å for MgO which is the same as the experimental value.

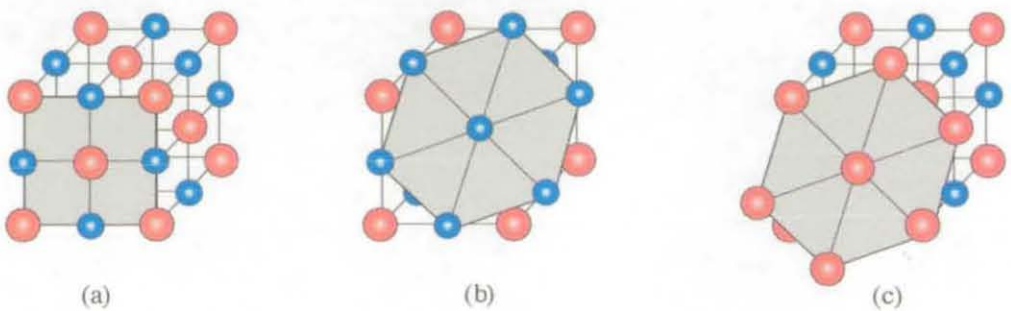

Figure 7.2: The structure of MgO; blue spheres denote Mg^{2+} ions and red spheres denote O^{2-} ions. (a) (100) charge-neutral plane consisting of cations and anions. (b) (111) plane of Mg^{2+} ions. (c) (111) plane of O^{2-} ions.

7.2.2 Al_2O_3

Aluminium oxide, or alumina, crystallises either as α-Al_2O_3, γ-Al_2O_3, or η-Al_2O_3 with α-Al_2O_3 being the most stable phase. γ- and η- alumina are widely used as catalysts and their structures are not very well characterised. The α phase of Al_2O_3 has the

corundum structure and is the only thermodynamically stable oxide of aluminium [101]. Its structure consists of a hexagonal close packed array of oxygen ions where the Al ions occupy 2/3 of the octahedral sites. This structure is complicated to visualise in 2-D as shown in fig. 7.3 with the lattice parameters being $a = 4.76$ Å and $c = 13.00$ Å. These values are the same as the experimental lattice parameters of α-Al_2O_3 [102]. There are two nearest neighbour Al-O bond lengths of 1.83 Å and 2.02 Å around each octahedra. This is only a metastable phase using empirical potentials which give the bixbyite structure as the most stable phase, albeit with a small energy difference [103].

As in the MgO (111) crystal, the α-Al_2O_3 (0001) structure is composed of alternate layers of cations and anions as shown in fig. 7.3 (b). The uppermost layer forms hexagonal structures, as shown by the black spheres in fig. 7.3 (c), and is similar to the MgO (111) terminated surface, such that the two oxides can be brought into contact with each other along these respective orientations.

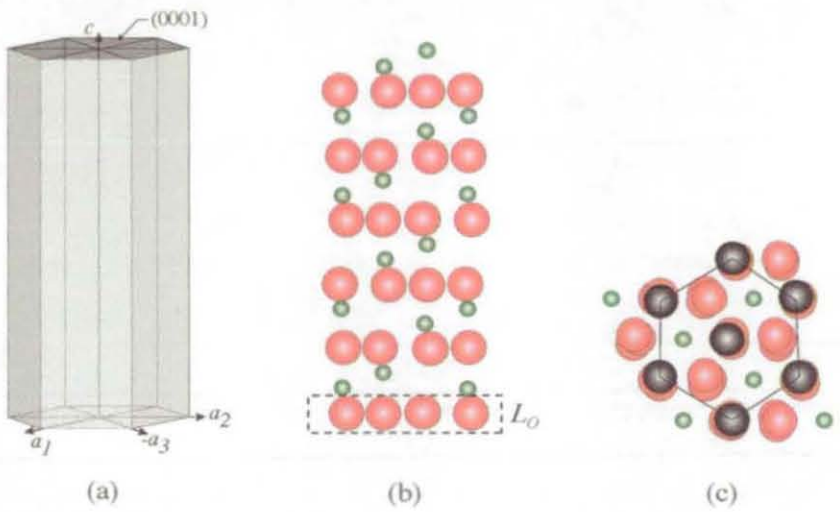

Figure 7.3: Bulk structure of Al_2O_3; green spheres denote Al^{3+} ions and red spheres denote O^{2-} ions. (a) Hexagonal outline. (b) Side view. (c) Top view (the black spheres denote O ions on the uppermost layer).

7.2.3 MgO/Al_2O_3

The MgO/Al_2O_3 system was set up from the individual lattices of MgO (111) and α-Al_2O_3 (0001) with the interatomic interactions determined by the spinel potential as described in section 3.2.4. The same crystal orientations are going to be used in experiments to look at the formation of a spinel structure between MgO and Al_2O_3 at Los Alamos. In our model, the Al_2O_3 lattice with a missing oxygen layer (L_O in fig. 7.3(b)), was placed above the oxygen-terminated MgO crystal as shown in fig. 7.4. The system's charge neutrality was restored by halving the charges of the Al ions in the topmost layer and the Mg ions in the bottommost layer. To find out the lattice mismatch at the interface, the distance between two oxygen ions lying in opposite corners of the hexagonal unit (as shown by the black spheres in fig. 7.3 (c)) was measured in both oxides. From there, the lattice mismatch was found to be 8 %.

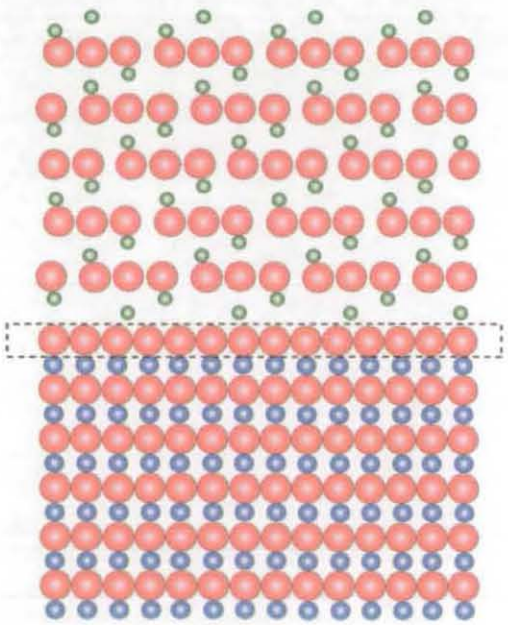

Figure 7.4: The MgO/Al_2O_3 system is constructed by placing the Al_2O_3 crystal on top of the MgO lattice (along the z-axis). The dashed section denotes the oxygen-terminated layer of MgO, shared by Al_2O_3.

Both crystals were joined together by keeping the lower MgO crystal fixed, and

by varying the position of the Al_2O_3 crystal along the x-, y- and z-axes until the minimal energy configuration was reached. In order to obtain a stable configuration, no periodic boundary conditions were used and the simulation cell was held by 9 Å of fixed atomic layers at the boundaries along the x- and y-axes. The thickness of the fixed boundaries along the vertical axis was 3.5 Å. The bonding at the interface was made optimal by thermalising four atomic layers above and four atomic layers below the interfacial region and keeping all other atoms fixed. This was done using the Nosé-Hoover thermostat, with the desired temperature set to 1200 K for 10 ps. Then, preserving the atomic velocities of the interfacial atoms, the whole system was damped until most of the energy was dissipated. At that point, the system could then be used for the production runs. However, before performing the collision cascades, the atomic positions close to the interface were analysed. It was found that some atoms formed spinel-like tetrahedra at the end of the relaxation phase. This rearrangement is depicted in fig. 7.5 showing only cations that have four oxygen nearest neighbours in the plane of the interface.

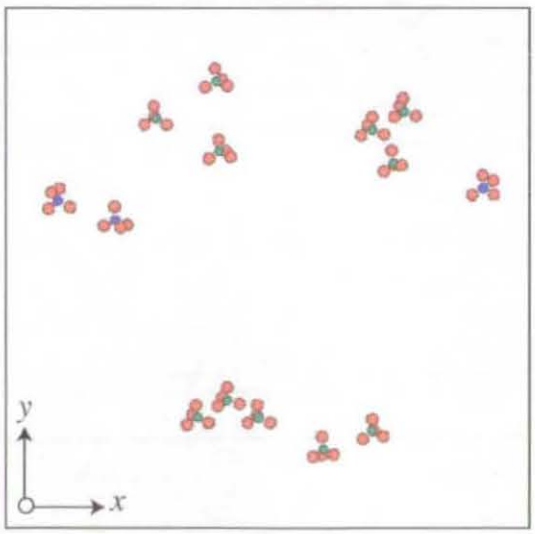

Figure 7.5: Cations and anions forming spinel-like tetrahedra due to interfacial reconstruction after thermalisation and damping in MgO/Al_2O_3. Only cations with coordination number four at the interface are shown.

7.3 Results

The dynamical cascades were initiated in the MgO crystal with the PKA oriented towards the Al_2O_3 region. We also investigated cascades originating from Al_2O_3 and directed towards MgO. A simulation cell of dimensions 71×71×55 Å^3 and made up of 29,760 atoms was utilised for the 0.6 keV cascades. Six trajectories were selected for each PKA, making a range of angles with respect to the interface. Each simulation started at the temperature of 0 K and was run for 8 ps.

For the cation PKAs, a second PKA was initiated in the structure, at the end of the first cascade. This was done by preserving the energy of the first simulation in the system. The second trajectory was chosen so that the cascade could be started on the opposite side of the cell relative to the first PKA and towards the defects created by the first PKA. The simulation was monitored for another 8 ps. The final temperature in the system at the end of the first displacement cascade was 130 K, while this was 260 K at the end of the second simulation.

7.3.1 Mg PKAs

Figs. 7.6(a)-(f) show the damage produced in the MgO/Al_2O_3 system when the simulation was initiated by a Mg PKA directed along [0 0 1], [5 7 14], [6 2 11], [10 0 17], [1 0 1], and [1 1 2] respectively.

The simulations show that no damage was left in the MgO region except for the Mg vacancy, V''_{Mg}, left by the PKA. However, when the PKA trajectory was perpendicular to the interface, i.e. along [1 0 0], the V''_{Mg} migrated to the interface where it formed an antisite, $Al^{\cdot}_{Mg}$, as shown by a grey cone in fig. 7.6(a). The same simulation resulted in some local rearrangements of anions at the interface, while the oxygen interstitials in the bulk Al_2O_3 formed split interstitials. More anion split interstitials can be identified in figs. 7.6 (c) and (e).

One typical feature of these cascades is that cation interstitials in Al_2O_3 occupied

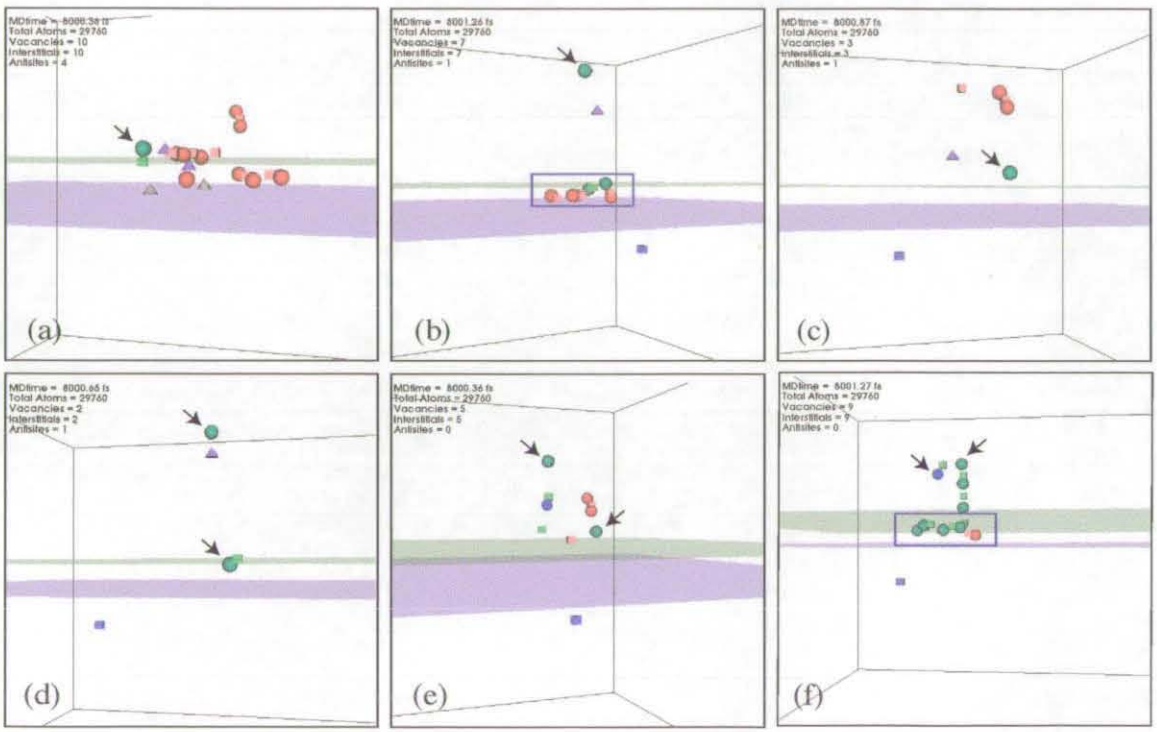

Figure 7.6: 0.6 keV cascade defects in MgO/Al_2O_3 generated by Mg PKAs. The blue plane denotes the uppermost Mg layer while the green plane defines the first plane of Al ions. Arrows indicate cations sitting at octahedral sites. Interfacial regions in (b) and (f) contain at least one cation with tetrahedral coordination.

empty octahedral sites in the structure. These can be identified by arrows in fig. 7.6. The Mg interstitials could also form antisites in the Al_2O_3 region as shown by the purple cones in figs. 7.6(a)-(d). The slight displacements of oxygen ions in the interfacial layer is due to the presence of irregular sites between the Al layer just above and the Mg layer just below it. It did not prove possible to classify this movement with any simple defect terminology.

Among the anion defects in the region of space bounded by the solid outline in fig. 7.6(b), there are two Al vacancies and two Al interstitials. By visual inspection, it was found that one Al interstitial had four oxygen nearest neighbours forming a tetrahedral arrangement, while the other Al interstitial had six anion neighbours forming a distorted octahedral arrangement around it. The local rearrangements depicted at the interfacial region in fig. 7.6(f) include two Al interstitials trapped at tetrahedral sites.

For each cascade, the atomic configuration at the end of the 8 ps was used as the starting configuration for a second 0.6 keV Mg PKA cascade. The final damage resulting from the configuration in fig. 7.6(a)-(f) is shown in fig. 7.7(a)-(f) in the same order. The defects in figs. 7.7(a)-(f) result from Mg PKAs set along [0 $\bar{2}$ 11], [$\bar{5}$ $\bar{7}$ 14], [$\bar{6}$ $\bar{2}$ 11], [$1\bar{0}$ 0 17], [$\bar{1}$ 0 1] and [$\bar{1}$ $\bar{1}$ 2] respectively.

Figs. 7.7(d) and (f) show that the second cascade did not change the morphology of the initial damage and did not induce any interfacial reconstruction. However, more anion displacements occurred at the interface in figs. 7.7(a)-(c). The simulation initiated along [$\bar{5}$ $\bar{7}$ 14] by a Mg PKA also resulted in the V''_{Mg} diffusing to the interface as part of the defect labelled *A* in fig. 7.7(b). The environment around defect *A* shows that the MgO structure has lost three Mg ions around the Mg interstitial; this structure was initially formed in the bulk MgO and it then migrated to the interface in a concerted motion. This indicates that around that cell, a spinel structure starts to form in MgO.

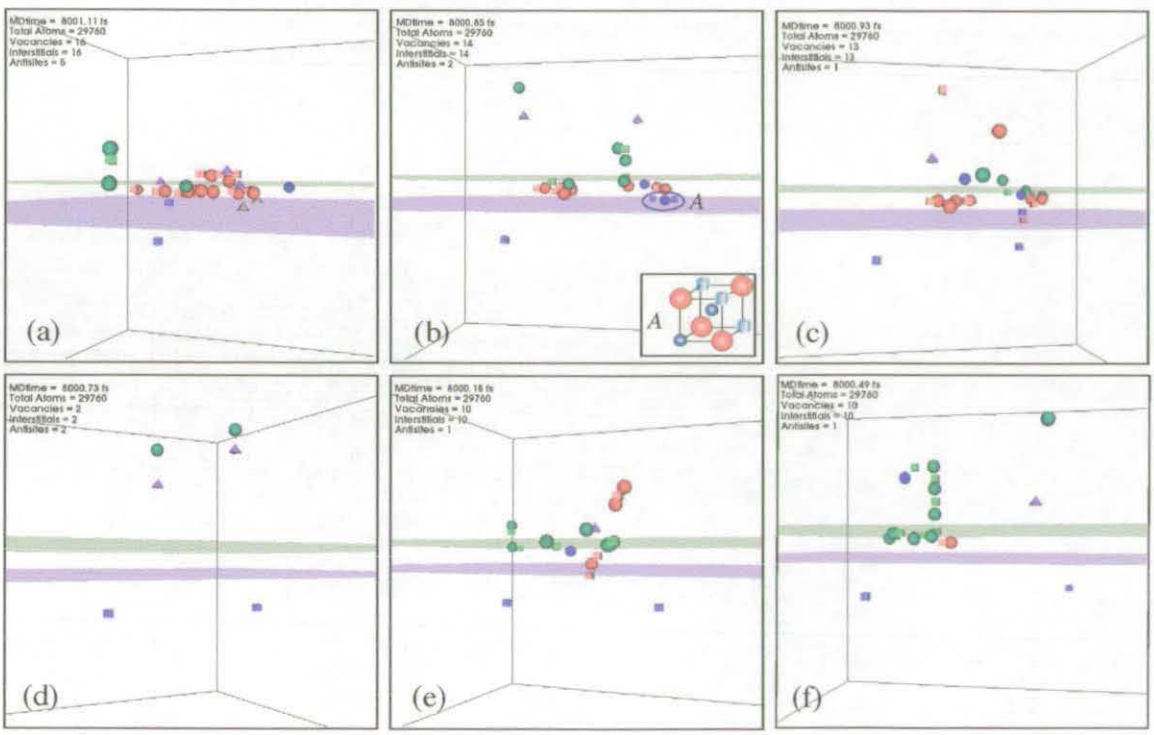

Figure 7.7: Residual damage in MgO/Al_2O_3 when a second 0.6 keV Mg PKA was initiated in the corresponding lattices shown in fig. 7.6.

7.3.2 Al PKAs

The damage caused to the MgO/Al_2O_3 system when choosing Al PKAs, directed from the Al_2O_3 region towards the MgO region, is shown in figs. 7.8(a)-(f) and figs. 7.9(a)-(f). The defects in figs. 7.8(a)-(f) result from the first knock-on event while the damage caused by the second PKA to the configurations in figs. 7.8(a)-(f) corresponds to those shown in figs. 7.9(a)-(f) in the same order. The PKA trajectories for the first simulation were [0 0 $\bar{1}$], [5 7 $\bar{14}$], [6 2 $\bar{11}$], [1 0 $\bar{1}$], [10 0 $\bar{17}$] and [1 1 $\bar{2}$], while for the second simulation,the following directions were chosen: [0 $\bar{2}$ $\bar{13}$], [$\bar{5}$ $\bar{7}$ $\bar{14}$], [$\bar{6}$ $\bar{2}$ $\bar{11}$], [$\bar{1}$ 0 $\bar{1}$], [$\bar{10}$ 0 $\bar{17}$] and [$\bar{1}$ $\bar{1}$ $\bar{2}$].

An important feature of all the cascades is the formation of $Al^{\cdot}_{Mg}$ antisites in the MgO crystal. These are encircled in figs. 7.8(a)-(f) and are also generated in fig. 7.9(a)-(f). Once an Al ion penetrates the MgO region, it preferentially displaces a Mg ion to form an antisite, rather than occupying an interstitial site in MgO. The displaced Mg ion can then sit at an interstitial site in the bulk MgO.

The arrows in fig. 7.8 denote cation interstitials with six anion neighbours. The two Al interstitials located by the bounded regions in fig. 7.8 (b) and (e) are centred around four oxygen neighbours in a distorted tetrahedral geometry. Three cations in the interfacial region in fig. 7.8 (d) also occupied tetrahedral sites in the structure. The defect structure labelled B in fig. 7.8 (e) consisted of three Mg interstitials and one O interstitial around a Mg site. It was immobile over the 8 ps time scale. The defect then became B' by getting an extra O and Mg interstitials during the second knock-on event as shown in fig. 7.9 (e). The defect B' was seen to dance in the lattice in a concerted motion similar to the mechanism observed for a hexa-interstitial in MgO [75].

The first PKA did not create a large amount of anion displacements while the second caused some local anion rearrangements at the interfacial region. The damage created at the interfacial region in fig. 7.9(b) consisted of clusters of defects. Among those identified are a vacancy cluster consisting of two Al and one Mg vacancies

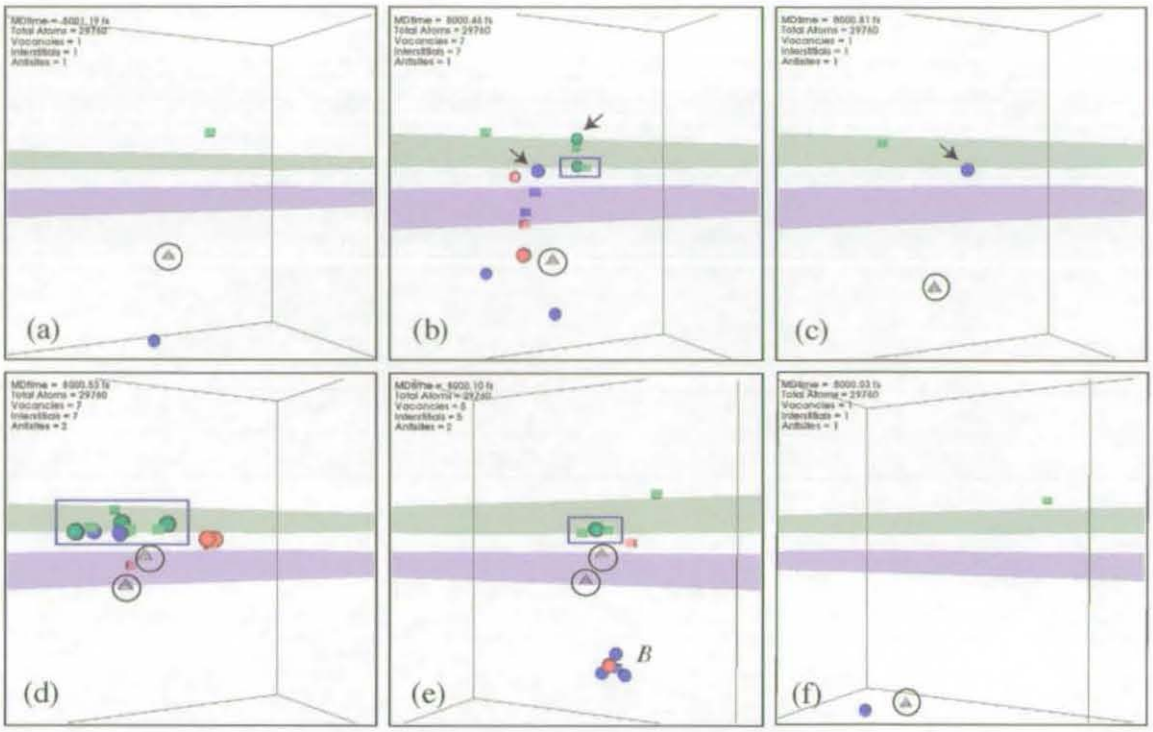

Figure 7.8: Defects generated by 0.6 keV Al PKAs in MgO/Al_2O_3.

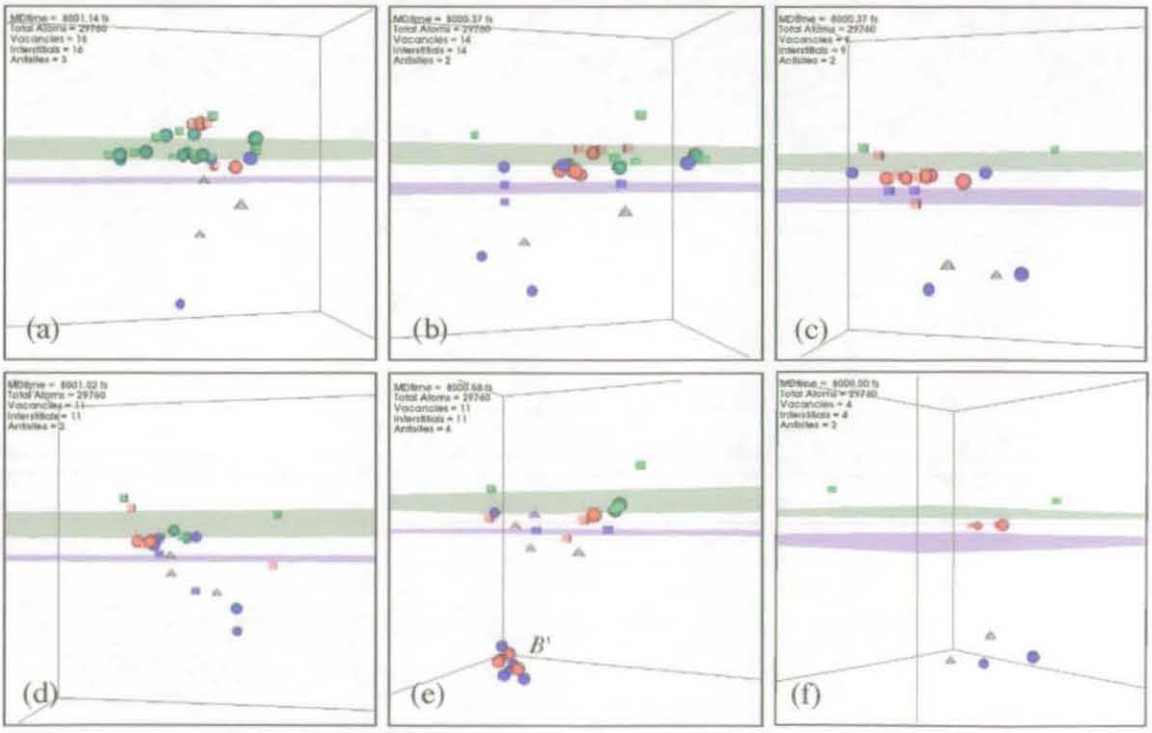

Figure 7.9: Final damage at the end of a second energetic recoil initiated in the corresponding lattices shown in fig. 7.8.

around a central Al interstitial, and an anion cluster of three interstitials sharing one vacancy site. The Al defects shown in fig. 7.9(a) were mainly of the split vacancy type. The precise environment around these defects is not well defined.

7.3.3 O PKAs

The damage incurred to the lattice by 0.6 keV O PKAs is shown in figs. 7.10(a)-(f) for the six simulations initiated in MgO and directed towards Al_2O_3 along the trajectories [0 0 1], [5 7 14], [6 2 11], [10 0 17], [1 0 1] and [1 1 2] respectively. Figs. 7.11(a)-(f) show the damage created at the end of another set of six simulations initiated in Al_2O_3 towards the MgO region along similar trajectories but in the opposite z-direction.

Most of the trajectories initiated from the MgO region resulted in channelling across the interface. These trajectories generally resulted in anion split interstitials to form in the Al_2O_3 crystal as illustrated in figs. 7.10(a)-(d) and (f). The densest cascade in the first set of simulations was obtained when the PKA was oriented along the [1 0 1] direction resulting in the defects shown in fig. 7.10(e). Here, the cascade propagated in the MgO region, in the interfacial region and in the bulk Al_2O_3, with a peak damage of 44 interstitials, 44 vacancies and 1 antisite after 75 fs. The surviving cation interstitials occupying octahedral sites in the structure are shown by arrows in the figures. Two cases whereby Al ions occupied distorted tetrahedral sites are identified by the squared outline in figs. 7.10(a) and (e).

The anion PKAs originating from Al_2O_3 created typical defects in the MgO crystal consisting of isolated vacancies and interstitials, and di- vacancies and interstitials. However, the presence of irregular sites at the interface acted as localised traps for ions undergoing a small displacement. Such situations are shown in figs. 7.11(b)-(f). Among the defects obtained are an anion cluster consisting of three vacancies and one interstitial, shown in fig. 7.11(c), and an oxygen ion sitting at an Al site in the disordered interfacial region of fig. 7.11(e). The least damage out of this set of simulations was generated along the [0 0 $\bar{1}$] trajectory and is shown in fig. 7.11(a).

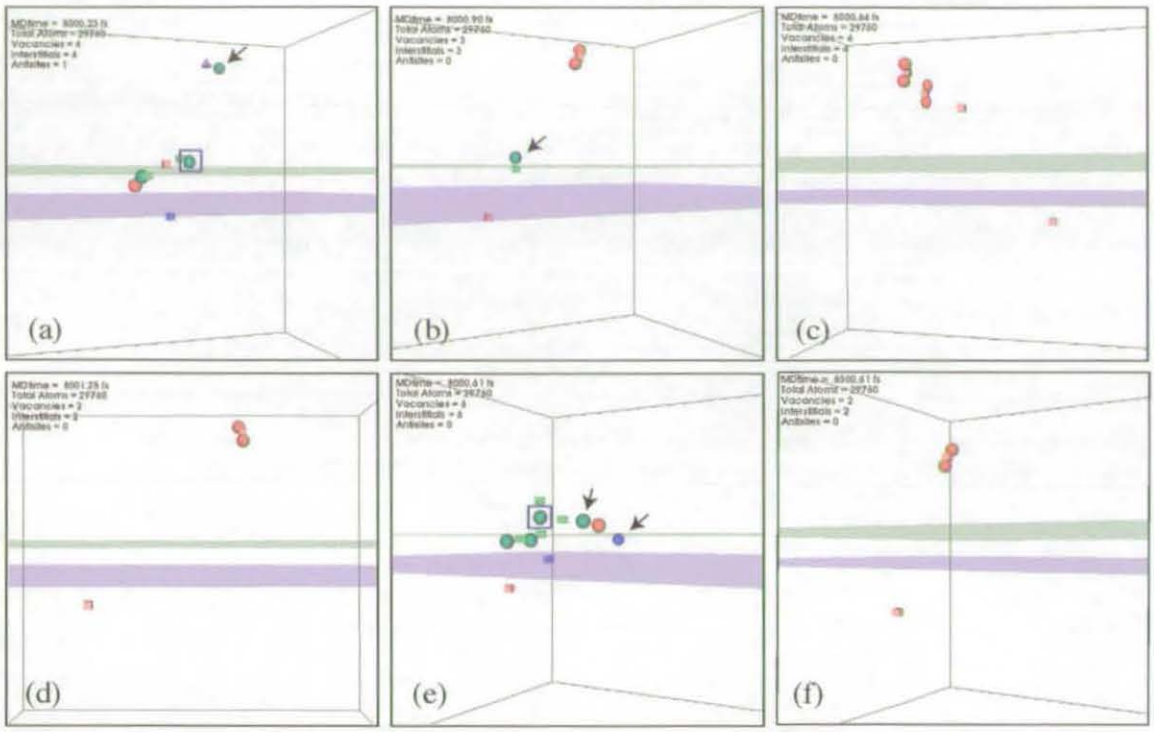

Figure 7.10: Defects produced by 0.6 keV anion PKAs initiated in MgO and directed towards Al_2O_3.

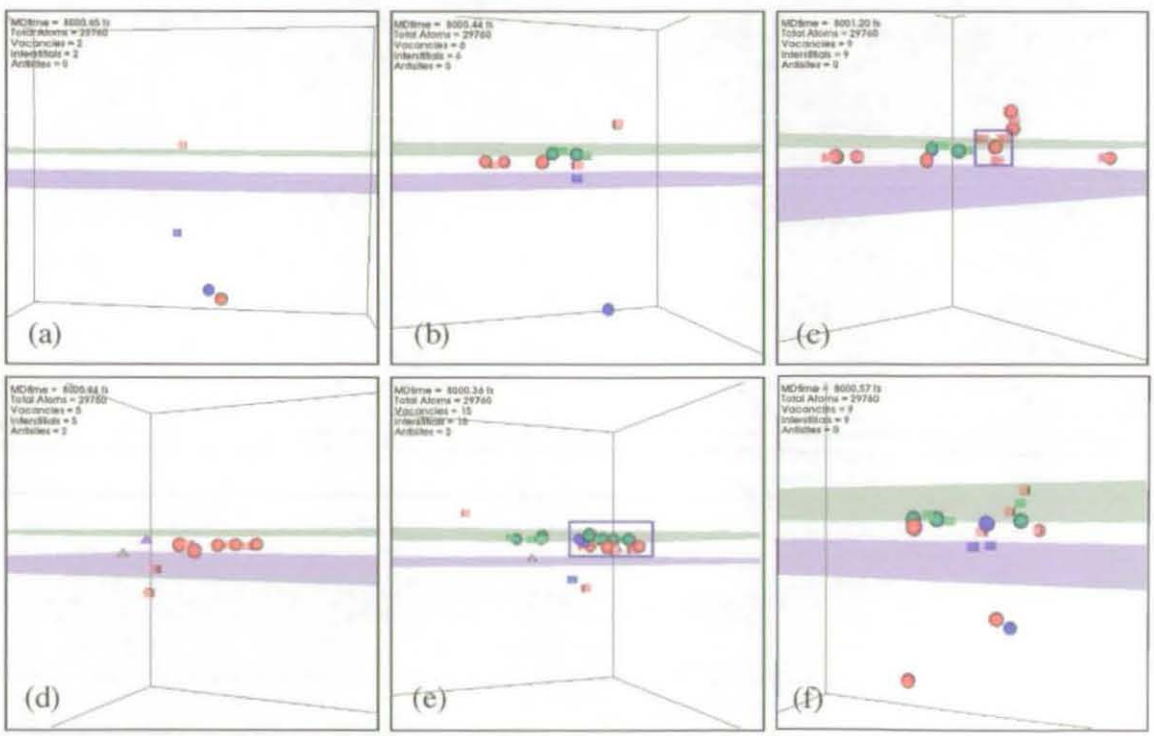

Figure 7.11: Surviving defects in MgO/Al_2O_3 due to anion PKAs set in the bulk Al_2O_3 towards MgO.

7.4 Discussions and conclusions

Low energy cascades were performed in a system consisting of (111) oriented rocksalt-structured MgO and (0001) oriented corundum-structured Al_2O_3 in order to investigate the formation of a spinel-structured interface between the two oxides. Growth of the spinel structure necessitates the presence of both octahedral and tetrahedral sites which can accommodate cation species. The first partial spinel transformations were obtained during the system preparation, after the interface thermalisation to 1200 K followed by a gradual damping of the atomic velocities. It was evident from fig. 7.5 that some tetrahedral interstices (fourfold coordinated with anions) started to form at the interface with trapped cations. By performing displacement cascades, interlayer mixing was anticipated. However, it proved difficult to analyse the defect distribution in the interfacial region itself. The lattice mismatch between MgO and Al_2O_3 resulted in irregular interstices with varying coordination with the anions. It was found that both cations and anions could rearrange themselves at those sites at the end of the simulations, but in a way that could not be classified.

In the MgO structure, the interstitial sites lie in the centre of the unit cell and are eight-fold coordinated by four Mg ions and four O ions. It suffices that three Mg ions around that site get displaced somewhere else in the structure while the fourth Mg ion settles at the interstitial site so that a spinel-like tetrahedral site is obtained. This is a bit like the reverse process of the rocksalt transformation in spinel described earlier. Part of that transformation has been found during the 0.6 keV displacement cascades as shown by the crystal arrangement labelled *A* in fig. 7.7(b). This structure was formed in the bulk MgO a few angstroms away from the interface, and migrated to the interface at the end of the 8 ps.

Another proposed mechanism that could contribute to the formation of spinel in MgO is the formation of $Al^{\cdot}_{Mg}$ antisites. Every penetrating Al ion in the bulk MgO resulted in an antisite occupying an octahedral site, while the displaced Mg ion be-

came an interstitial. The repulsive charges between the antisite and the displaced Mg ion would cause the latter defect to migrate away from the former. The over-bonding of the six oxygen ions around this Al antisite could result in an easier release of other neighbouring Mg ions. In the presence of oxygen interstitials, the Mg interstitials can form mobile clusters which could diffuse somewhere else in the MgO structure.

Watson *et al.* [99] investigated the rate of spinel growth in the MgO/Al_2O_3 system at various temperatures and pressures. It was observed that at the temperature of 1500 K, the rate of spinel formation was too slow to be measured. The growth process itself is attributed to the interdiffusion of Mg and Al ions through the spinel layer, but the precise mechanism is unknown. In their experiment, they found that the amount of corundum and MgO consumed during the spinel growth was in a ratio of 3:1. The cascade simulations reported here were initiated at 0 K. The amount of energy imparted to the system might be too small (0.6 keV) in order to activate significant lattice reconstruction at the interface. Even the second cation PKAs could hardly create observable amounts of spinel. This means that more overlapping cascades need to be investigated at this energy and at higher energies. A systematic way of doing that could be to remove the energy out of the system after each cascade.

Johnson *et al.* [96] found that under thermal treatment, $NiAl_2O_4$ spinel growth was more significant in nickel oxide as compared to Al_2O_3. This was due to the presence of a twin boundary in NiO that acted as a nucleation site for the spinel. In our model, perfect MgO and Al_2O_3 crystals were joined together, without any grains. A improvement to the existing model could be by modelling grain boundaries in these crystals so that a better picture of the diffusion process and the spinel formation can be obtained.

An alternative approach is to investigate diffusion only in the MgO/Al_2O_3 system without performing the dynamical cascades. This can be done by using accelerated dynamics techniques such as TAD or even kinetic Monte-Carlo simulations. Over longer time scales, the diffusion mechanisms unaccessible by normal MD simulations

can thus be determined.

Chapter 8

Conclusions and Future Work

8.1 Conclusions

Molecular dynamics was used to investigate the structural evolution of three Mg-based spinels under the impact of an energetic projectile with kinetic energy ranging between a few hundreds of electron-volts up to several thousands of electron-volts. First, the threshold energy was determined along different crystallographic directions and for each sublattice in the normal magnesium aluminate spinel, $MgAl_2O_4$. It was found that, in general, anions could be displaced more easily from their sites as compared to cations, with energies as low as 27.5 eV.

The energetic cascades in the normal spinel resulted in well-defined defects consisting of split interstitials, isolated and pairs of vacancies, split vacancies and ring structures on the Al sublattice, and cation antisite defects. The cation split interstitials consisted of two interstitials sharing one tetrahedral vacancy with the two interstitials close to octahedral interstices, while in the ring structures and split vacancy defects, interstitials could occupy tetrahedral interstices. The same typical defects observed at the low energies were seen at energies of 5 keV and 10 keV mainly because of subcascade branching and efficient interstitial-vacancy mechanisms.

The formation of antisites resulted in some local distortion of the lattice due to

the amount of under/over bonding of the surrounding anions. The defect formation energies calculated from empirical potentials and *ab-initio* techniques [71], showed that antisites are the most favourable defect types in spinel. This is in accordance to the fact that spinel naturally exhibits various amounts of cation disordering whereby Mg^{2+} ions can interchange sites with Al^{3+} ions in the structure. Over the time scales investigated by the MD simulations, antisites were the predominant defects obtained at all energies.

The half-inverse magnesium gallate and fully inverse magnesium indate were investigated to look at the impact of cation disorder on defect production by displacive radiation in compounds having the spinel structure. It was found that radiation damage became more complex and took longer to anneal in the spinels with non-zero inversion as the energy of the knock-on event was increased. Along certain trajectories, different atomic rearrangements were observed in the half-inverse and inverse spinels as compared to the normal spinel. In the fully inverse spinel, a rock-salt type region started to form whereby a larger number of interstitials occupied octahedral sites around empty tetrahedral sites.

The kinetics of point defects in the three spinels was investigated using temperature accelerated dynamics [3]. The energy barriers and the mechanisms for defect motion have been elucidated for the normal magnesium aluminate spinel. The most mobile species was the oxygen split interstitial having an activation energy of 0.29 eV for diffusing one-dimensionally. However, in the spinels with inversion, the random distribution of cations induced local traps that hindered the diffusion process. Here, the defects were found to oscillate locally without diffusing over long distances in the structure.

The results presented in this thesis has brought fundamental understanding of the creation of defects in the spinel microstructure and how these defects diffuse in the crystal. Modelling the spinel system was more complex than simple oxides like MgO because of the presence of three distinct sublattices as well as structural vacancies in

the structure. The complexity of the system was increased with inversion. For the inverse spinels, in many cases the damage consisted of chains of vacancies alternating with interstitials, with the interstitials occupying structural vacancies in the lattice. Over the time scales accessible by TAD, no net diffusion occurred in the half-inverse and inverse spinels, the defects being trapped by the anisotropy of the inversion. The results from the MD simulations have been published in [104], [105] and [106], while TAD results on the long-time evolution of point defects have been submitted for publication [89].

The last part of the work was to investigate the interfacial rearrangement brought about by low-energy cascades in a MgO/Al_2O_3 system. The structure was set up by a thermalisation and relaxation process, during which spinel-like tetrahedral sites formed at the interface. During the dynamical cascades, some small displacements occurred at the interfacial region whereby ions could occupy irregular sites. However, no clear indication of further spinel growth at the interface was observed as a result of the low-energy displacement cascades.

8.2 Future Work

As a continuation of the work presented in this thesis, several further investigations can be made. The MD code was initially unequipped with a parallel algorithm for evaluating Coulomb forces. With the implementation of the parallel DPMTA library, it is now possible perform MD simulations on large ionic systems within a reasonable amount of time. The MD simulations have been successfully run on machines with parallel architectures, with tests carried out on a maximum of 32 processors. It would be interesting to fully use the resources of Loughborough University's High Performance Computing and Visualisation Centre in order to perform multi-million atom simulations in these materials so that higher energy PKAs can be analysed. Simulations involving multiple PKAs can also be performed in order to investigate

dose effects.

An important part of the work was to study the long time evolution of point defects using the serial TAD code. However, radiation damage, as seen from the cascades, is characterised by regions containing more than one defect, mutually interacting with each other. Because of the time scale limitation of MD, it would be ideal to use the whole configuration obtained at the end of a collision cascade, and evolve it over longer time-scales using TAD. This approach might require larger simulation cells to be used. The largest reported cell used for a TAD simulation contained 1728 atoms [88]. The simulations performed in the half-inverse and inverse spinels in a cell containing 448 atoms took about one month to run. The amount of computation would therefore require parallelisation of the TAD code. Another approach would be to carve out regions obtained from the collision cascades and investigate their long time evolution using the current version of TAD.

Experimental observations have attributed the amorphisation of magnesium aluminate spinel to be the result of an accumulation of point defects and cation disorder defects within the structure. This transformation can be investigated by constantly incorporating point defects into the spinel structure followed by relaxation using MD simulations. The different mechanisms for defect accumulation/cluster nucleation can be studied as well as their consequences on the stability of the crystal. The hardness of the material, before and after this procedure, can be investigated by nanoindentation techniques [107] and compared to experimental results [25]. However, the polarity of the free surfaces in spinel might be problematic for nanoindentation simulations. *Ab-initio* calculations showed that the Mg-terminated surface is more stable than the Al-terminated surface [108].

The simulations performed in the half-inverse $MgGa_2O_4$ and the fully inverse $MgIn_2O_4$ showed that cation disorder considerably affects the defect evolution due to irradiation, as compared to the normal $MgAl_2O_4$. The $MgAl_2O_4$ spinel used in this work is perfect and has a zero inversion parameter. However, $MgAl_2O_4$ naturally

contains a number of antisite defects in its structure. Another approach to investigate radiation damage in $MgAl_2O_4$, is to run the simulations again in structures that have different amounts of inversion. The results could then be compared with the perfect normal spinel. It would be expected that inversion would result in more complex cascades as well as a reduction in defect mobility.

The effects of radiation on polycrystalline spinel can be investigated by including grain boundaries in the current model. The interaction of cascade defects with the grain boundaries could then be analysed. This approach could also be extended to the MgO/Al_2O_3 system or even a $MgO/MgAl_2O_4/Al_2O_3$ system consisting of a spinel interface between MgO and Al_2O_3. In the latter systems, the grain boundaries could act as sinks for point defects whereby spinel formation and growth could be observed. Other techniques such as TAD or kinetic Monte-Carlo could be used to further analyse the mechanisms for diffusion in those systems.

The ionic interactions were modelled using the standard pairwise Buckingham potential. With recent developments in this field, several modifications to the ionic force field have been proposed. Among the models found in the literature are those that use a variable charge scheme [109] and those that include many-body terms in the potential function [110]. Another technique for modelling atomic interactions is by using a neural-network [111] which has the advantage of not assuming any particular functional form in contrast to empirical potentials. Further work needs to be addressed to investigate whether these force field models can be adapted to the systems considered in this thesis.

The methodology presented in this work can be used to investigate radiation damage in several other promising materials for nuclear applications including bixbyites, fluorites and perovskites.

Bibliography

[1] A. R. Leach, Molecular Modelling, Longman, 1996.

[2] R. Phillips, Crystals, Defects and Microstructures: Modeling Across Scales, Cambridge University Press, 2001.

[3] M. R. Sørensen, A. F. Voter, J. Chem. Phys. **112** (2000) 9599.

[4] G. R. Lumpkin, Progress in Nuclear Energy, Vol. 38 (2001) 447.

[5] S. Wei, S. B. Zhang, Phys. Rev. B **63** (2001) 045112.

[6] N. W. Grimes, Phys. Technol. **6** (1975) 22.

[7] N. F. M. Henry, K. Lonsdale (Eds.), International Tables for X-ray Crystallography, Vol. I. Kynoch Press, Birmingham, England, 1952.

[8] R. W. G. Wyckoff, Crystal Structures, 2nd Ed., Interscience Publishers, 1968.

[9] K. E. Sickafus, J. M. Wills, N. W. Grimes, J. Am. Ceram. Soc. **82** (1999) 3279.

[10] F. A. Kröger, H. A. Vink, Solid State Physics: Advances in Research and Applications, New-York: Academic (1957).

[11] U. Schmocker, F. Waldner, J. Phys. C **9** (1976) L235.

[12] R. I. Sheldon, T. Hartmann, K. E. Sickafus, A. Ibarra, B. L. Scott, D. N. Argyriou, A. C. Larson, R. B. Von Dreele, J. Am. Ceram. Soc. **82** (1999) 3293.

[13] J. B. Goodenough, A. L. Loeb, Phys. Rev. **98** (1955) 391.

[14] J. E. Weidenborner, N. R. Stemple, Y. Okaya, Acta Cryst. **20** (1966) 761.

[15] G. S. Rohrer, Crystalline Materials, Cambridge University Press, Cambridge, U.K., 2001.

[16] G. B. Andreozzi, F. Princivalle, H. Skogby, A. Della Guista, Am. Miner. **85** (2000) 1164.

[17] J. Ball, R. W. Grimes, D. Price, B. P. Uberuaga, M. O. Zacate J. Phys.: Condens. Matter **17** (2005) 7621.

[18] S. A. T. Redfern, R. J. Harrison, H. St. C. O'Neill, D. R. R. Wood, Am. Miner. **84** (1999) 299.

[19] L. Pauling, J. Amer. Chem. Soc. **51** (1929) 1010.

[20] F. W. Clinard, G. F. Hurley, L. W. Hobbs, J. Nucl. Mater. **108-109** (1982) 655.

[21] F. W. Clinard, G. F. Hurley, L. W. Hobbs, D. L. Rohr, R. A. Youngman, J. Nucl. Mater. **122-123** (1984) 1386.

[22] F. A. Garner, G. W. Hollenberg, F. D. Hobbs, J. L. Ryan, Z. Li, C. A. Black, R. C. Bradt, J. Nucl. Mater. **212-215** (1994) 1087.

[23] K. E. Sickafus, A. C. Larson, N. Yu, M. Nastasi, G. W. Hollenberg, F. A. Garner, R. C. Bradt, J. Nucl. Mater. **219** (1995) 128.

[24] N. Yu, K. E. Sickafus, M. Nastasi, Phil. Mag. Lett. **70** (1994) 235.

[25] R. Devanathan, N. Yu, K. E. Sickafus, M. Nastasi, J. Nucl. Mater. **232** (1996) 59.

[26] M. Ishimaru, I. V. Afanasyev-Charkin, K. E. Sickafus, Appl. Phys. Lett. **76** (2000) 2556.

[27] N. Bordes, L. M. Wang, R. C. Ewing, K. E. Sickafus, J. Mater. Res. **10** (1995) 981.

[28] R. P. Gupta, J. Nucl. Mater. **358** (2006) 35.

[29] V. Daggett, M. Levitt, Ann. Rev. Biophys. Biomol. Struct. **22** (1993) 353.

[30] D. Mulliah, S. D. Kenny, R. Smith, C. F. Sanz-Navarro, Nanotechnology **15** (2004) 243.

[31] L. Van Brutzel, J-M. Delaye, D. Ghaleb, M. Rarivomanantsoa, Phil. Mag. **83** (2003) 4083.

[32] C. H. Xu, C. Z. Wang, C. T. Chan, K. M. Ho, J. Phys.: Condens. Matter. **4** (1992) 6047.

[33] Ş. Erkoç, Empirical potential energy functions used in the simulation of materials properties, D. Stauffer (Ed.), Ann. Rev. Comp. Phys. IX, World Scientific, 2001.

[34] M. P. Allen, D. J. Tildesley, Computer Simulations in Liquids, Clarendon Press, Oxford, 1987.

[35] H. Y. Erbil, Surface chemistry of solid and liquid interfaces, Blackwell Publishing Ltd, 2006.

[36] C. R. A. Catlow, C. M. Freeman, M. S. Islam, Phil. Mag. A **58** (1988) 123.

[37] J. Keinonen, Atomic collisions in matter, R. Hellborg (Ed.), Electrostatic Accelerators, Springer, New York, 2005.

[38] J. P. Biersack, J. Ziegler and U. Littmark, The Stopping Range of Ions in Solids, Pergamon Press, Oxford (1985).

[39] R. Smith, M. Jarkas, D. Ashworth, B. Oven, M. Bowyer, I. Chakarov, R. Webb, Atomic and Ion Collisions in Solids and at Surfaces, Cambridge University Press, 1997.

[40] R. W. Grimes, S. P. Chen, J. Phys. Chem. Solids **61** (2000) 1263.

[41] M. R. Levy, R. W. Grimes, K. E. Sickafus, Phil. Mag. **84** (2004) 533.

[42] S. P. Chen, M. Yan, J. D. Gale, R, W. Grimes, R. Devanathan, K. E. Sickafus, N. Yu, M. Nastasi, Phil. Mag. Lett. **73** (1996) 51.

[43] R. J. Hill, J. Craig, G. V. Gibbs, Phys. Chem. Minerals 4 (1979) 317.

[44] M. B. Kruger, J. H. Nguyen, W. Caldwell, R. Jeanloz, Phys. Rev. B **56** (1997) 1.

[45] T. S. Bush, J. D. Gale, C. R. A. Catlow, P. D. Battle, J. Mater. Chem. **4** (1994) 831.

[46] D. Frenkel, B. Smit, Understanding Molecular Simulation, Academic Press, 1996.

[47] L. Verlet, Phys. Rev. **159** (1967) 98.

[48] W. C. Swope, H. C. Andersen, P. H. Berens, K. R. Wilson, J. Chem. Phys. **76** (1982) 637.

[49] J. Lindhard, M. Scharff, H. E. Schiøtt, Mat. Fys. Medd. Dan. Vid. Selsk. **33** (1963) 1.

[50] H. J. C. Berendsen, J. P. M. Postma, W. F. van Gunsteren, A. DiNola, J. R. Haak, J. Chem. Phys. **81** (1984) 3684.

[51] W. G. Hoover, Phys. Rev. A **31** (1995) 1695.

[52] S. Nosé, J. Phys.: Condens. Matter **2** (1990) SA115.

[53] W. T. Rankin, J. A. Board Jr., Proceedings of the 1995 IEEE Symposium on High Performance Distributed Computing, IEEE Computer Society Press, Los Alamitos, California, 1995, p. 17.

[54] S. Ogata, T. J. Campbell, R. K. Kalia, A. Nakano, P. Vashishta, S. Vemparala, Computer Physics Communications **153** (2003) 445.

[55] K. Esselink, Computer Physics Communications **87** (1995) 375.

[56] L. Greengard, V. Rokhlin, J. Comput. Phys. **135** (1997) 280.

[57] S. Plimpton, J. Comput. Phys. **117** (1995) 1.

[58] http://www-unix.mcs.anl.gov/mpi/

[59] W. T. Rankin III, Ph.D Thesis: Efficient Parallel Implementations of Multipole Based N-Body Algorithms, Duke University, 1999.

[60] D. Ramasawmy, Ph.D Thesis: Computer Simulation of Sputtering and Radiation Damage in Ionic Materials, Loughborough University, 2004.

[61] http://public.kitware.com/VTK/index.php

[62] K. E. Sickafus, L. Minervini, R. W. Grimes, J. A. Valdez, M. Ishimaru, F. Li, K. J. McClellan, T. Hartmann, Science **289** (2000) 748.

[63] S. J. Zinkle, C. Kinoshita, J. Nucl. Mater. **251** (1997) 200.

[64] B. Park, W. J. Weber, L. R. Corrales, Phys. Rev. B **64** (2001) 174108.

[65] G. P. Summers, G. S. White, K. H. Lee, J. H. Crawford Jr., Phys. Rev. B **21** (1980) 2578.

[66] Particle interactions with matter, http://www.srim.org/.

[67] I. V. Afanasyev-Charkin, D. W. Cooke, M. Ishimaru, B. L. Bennett , V. T. Gritsyna, J. R. Williams, K. E. Sickafus, Optical Materials **16** (2001) 397.

[68] I. V. Afanasyev-Charkin, R. Dickerson, D. W. Cooke, B. L. Bennett , V. T. Gritsyna, K. E. Sickafus, J. Nucl. Mater. **289** (2001) 110.

[69] R. E. Williford, R. Devanathan, W. J. Weber, Nucl. Instr. and Meth. in Phys. Res. B **141** (1998) 94.

[70] J. D. Gale, GULP (General Lattice Utility Program), Royal Institution of Great Britain, London, 1993.

[71] Christopher Gilbert (private communication), 2006.

[72] S. D. Kenny, A. P. Horsfield, H. Fujitani, Phys. Rev. **62** (2000) 4899.

[73] B. Park, W. J. Weber, L. R. Corrales, Nucl. Instr. and Meth. in Phys. Res. B **166** (2000) 357.

[74] J. A. Purton, N. L. Allan, J. Mater. Chem. **12** (2002) 2923.

[75] B. P. Uberuaga, R. Smith, A. R. Cleave, G. Henkelman, R. W. Grimes, A. F. Voter, K. E. Sickafus, Phys. Rev. Lett. **92** (2004) 115505.

[76] M. O. Zacate, R. W. Grimes, Phil. Mag. A **80** (2000) 797.

[77] K. Trachenko, J. M. Pruneda, E. Artacho, M. T. Dove, Phys. Rev. B **71** (2005) 184104.

[78] K. Trachenko, M. T. Dove, E. Artacho, I. T. Todorov, W. Smith, Phys. Rev. B **73** (2006) 174207.

[79] C. S. Becquart, C. Domain, A. Legris, J. C. Van Duysen, J. Nucl. Mater. **280** (2000) 73.

[80] D. Terentyev, C. Lagerstedt, P. Olsson, K. Nordlund, J. Wallenius, C. S. Becquart, L. Malerba, J. Nucl. Mater. **351** (2006) 65.

[81] A. F. Voter, F. Montalenti, T. C. Germann, Annu. Rev. Mater. Res. **32** (2002) 321.

[82] B. P. Uberuaga, F. Montalenti, T. C. Germann, A. F. Voter, Accelerated Molecular Dynamics Methods, S. Yip (Ed.), Handbook of Materials Modeling, Springer, 2005.

[83] A. F. Voter, Phys. Rev. B **57** (1998) R13985.

[84] A. F. Voter, Phys. Rev. Lett. **78** (1997) 3908.

[85] G. H. Vineyard, J. Phys. Chem. Solids **3** (1957) 121.

[86] H. Jónsson, G. Mills, K. W. Jacobsen, Nudged Elastic Band Method for Finding Minimum Energy Paths of Transitions, B. J. Berne, G. Ciccotti and D. F. Coker (Eds.), Classical and Quantum Dynamics in Condensed Phase Simulations, World Scientific, 1998.

[87] G. Henkelman, B. P. Uberuaga, H. Jónsson, J. Chem. Phys. **113** (2000) 9901.

[88] B. P. Uberuaga, R. Smith, A. R. Cleave, G. Henkelman, R. W. Grimes, A. F. Voter, K. E. Sickafus, Phys. Rev. B **71** (2005) 104102.

[89] B. P. Uberuaga, D. Bacorisen, R. Smith, J. A. Ball, R. W. Grimes, A. F. Voter, K. E. Sickafus, *submitted.*

[90] K. Yasuda, C. Kinoshita, K. Fukuda, F. A. Garner, J. Nucl. Mater. **283** (2000) 937.

[91] K. Ando, Y. Oishi, J. Chem. Phys. **61** (1974) 625.

[92] R. Lindner, A. Akerstrom, Z. Phys. Chem. Neue Folge **18** (1958) 303.

[93] N. Bordes, K. E. Sickafus, E. A. Cooper, R. C. Ewing, J. Nucl. Mater. **225** (1995) 318.

[94] R. Devanathan, N. Yu, K. E. Sickafus, M. Nastasi, Nucl. Instr. and Meth. in Phys. Res. B **127/128** (1997) 608.

[95] C. Kinoshita, H. Abe, S. Maeda, K. Fukumoto, J. Nucl. Mater. **219** (1995) 152.

[96] M. T. Johnson, J. R. Heffelfinger, P. G. Kotula, C. B. Carter, J. Microscopy **185** (1997) 225.

[97] P. G. Kotula, C. B. Carter, J. Am. Ceram. Soc. **81** (1998) 2877.

[98] L. Navias, J. Am. Ceram. Soc. **45** (1962) 544.

[99] E. B. Watson, J. D. Price, Geochim. Cosmochim. Acta. **66** (2002) 2123.

[100] A. Wander, I. J. Bush, N. M. Harrison, Phys. Rev. B **68** (2003) 233405.

[101] G. Paglia, Ph.D Thesis: Determination of the Structure of γ-Alumina using Empirical and First Principles Calculations combined with Supporting Experiments, Curtin University of Technology, 2004.

[102] K. J. W. Atkinson, R. W. Grimes, M. R. Levy, Z. L. Coull, T. English, J. Euro. Ceram. Soc. **23** (2003) 3059.

[103] J. D. Gale, C. R. A. Catlow, W. C. Mackrodt, Modelling Simul. Mater. Sci. Eng. **1** (1992) 73.

[104] R. Smith, D. Bacorisen, B. P. Uberuaga, K. E. Sickafus, J. A. Ball, R. W. Grimes, J. Phys.: Condens. Matter. **17** (2005), 875.

[105] D. Bacorisen, R. Smith, J. A. Ball, R. W. Grimes, B. P. Uberuaga, K. E. Sickafus, W. T. Rankin, Nucl. Instr. and Meth. in Phys. Res. B **250** (2006) 36.

[106] D. Bacorisen, R. Smith, B. P. Uberuaga, K. E. Sickafus, J. A. Ball, R. W. Grimes, Phys. Rev. B **74** (2006) 214105.

[107] R. Smith, D. Christopher, S. D. Kenny, A. Richter, B. Wolf, Phys. Rev. B **67** (2003) 245405.

[108] N. J. Van der Laag, C. M. Fang, G. de With, G. A. de Wijs, H. H. Brongersma, J. Am. Ceram. Soc. **88** (2005) 1544.

[109] X. W. Zhou, H. N. G. Wadley, J. S. Filhol, M. N. Neurock, Phys. Rev. B **69** (2004) 2354XX.

[110] P. Tangney, S. Scandolo, J. Chem. Phys. **119** (2003) 9673.

[111] A. Bholoa, Ph.D Thesis: Potential Energy Surfaces Using Neural Networks, Loughborough University, 2006.